Development and Implementation of Trajectory Optimization Technologies for Cranial Stereotactic Radiation Therapy

by

R. Lee MacDonald

Submitted in partial fulfilment of the requirements
for the degree of Doctor of Philosophy

at

Dalhousie University
Halifax, Nova Scotia
July 2018

TABLE OF CONTENTS

LIST OF TABLES

LIST OF FIGURES

ABSTRACT

Radiotherapy treatment planning optimization employs metrics for the quantification of plan quality indicators based on a set of input desired criteria by the planner. Patient-specificity in current practice is limited to the customization and refinement of input optimization criteria to contextualize relative urgency. The arc geometry and machine trajectory in radiotherapy planning can create additional opportunities for optimization on a patient-specific basis. This work proposes novel technologies capable of leveraging new degrees of freedom in the domain of radiotherapy to improve radiotherapy plan quality.

A series of four manuscripts form the basis for this thesis. The first manuscript, "*Overlap Guided Fixed Patient Support Positioning Optimization for Cranial SRT*", is an investigation into the optimization of couch rotation angle in the standard cranial stereotactic VMAT template to reduce the presence of overlap of sensitive structures with the targeted tissues in the aperture of the radiation beam. The second manuscript, "*Dynamic Collimator Trajectory Algorithm for Multiple Metastases Dynamic Conformal Arc Treatment Planning*", demonstrates a novel method of reducing the presence of uncollimated non-target anatomy from the aperture of the radiation beam and increases the efficacy of collimation by optimizing the rotation angles of the multi-leaf collimator. Additionally, it proposes the use of dynamically updated collimator angle throughout delivery to maximize the capacity of this optimization. The third manuscript, "*Intra-Arc Binary Collimation Algorithm for the Optimization of Stereotactic Radiotherapy Treatment of Multiple Metastases with Multiple Prescriptions*", demonstrates a novel method of aperture design in multiple metastases cranial radiosurgery which maximizes the presence of conformal aperture to increase the efficiency of monitor units, while regularly shielding targets completely to modulate dose to meet target prescription and healthy tissues sparing. Finally, the fourth manuscript, "*CODA: Combined Optimization of Dynamic Axes*", is the first investigation into the synergistic optimization of the rotation angle of the collimator, the rotation angle of the treatment couch, and the rotation angle of the gantry to accomplish the objectives of normal tissue sparing and treatment efficiency using a novel organization of cost function and trajectory design.

These manuscripts form the basis for automated optimization of linear accelerator trajectories in cranial radiosurgery. Their implementation can result in significant increases in plan quality when compared to state of the art conventional treatment planning. The introduction of these additional forms of optimization can be used to mitigate the effects of inter-planner variation in plan quality by automating the steps performed in expert-planning.

LIST OF ABBREVIATIONS USED

1D	One-Dimensional
2D	Two-Dimensional
3D	Three-Dimensional
3D-CRT	Three-Dimensional Conformal Radiation Therapy
AAA	Anisotropic Analytical Algorithm
AG	Aktiengesellschaft
APBI	Accelerated Partial Breast Irradiation
AVM	Arteriovenous Malformation
BEV	Beam's Eye View
BAO	Beam Angle Optimization
CG	Couch-Gantry
CK	Cyber Knife
CN	Conformity Number
CMD	Certified Medical Dosimetrist
CNS	Central Nervous System
CR-IMRT	Collimator Rotation Intensity Modulated Radiation Therapy
CT	Computed Tomography
CODA	Combined Optimization of Dynamic Axes
COM	Centre of Mass
DAO	Direct Aperture Optimization
DCA	Dynamic Conformal Arc
DCT-DCA	Dynamic Collimator Trajectory Dynamic Conformal Arc
DICOM	Digital Imaging and Communications in Medicine
DNA	Deoxyribonucleic Acid
DVH	Dose Volume Histogram
EBRT	External Beam Radiation Therapy
FC-DCA	Fixed Collimator Dynamic Conformal Arc
FFF	Flattening Filter Free
GK	Gamma Knife
GOS	Geometric Overlap Score
HD	High Definition
HI	Homogeneity Index
HU	Hounsfield Unit
iABC	Intra-Arc Binary Collimation
IEC	International Electrotechnical Commission
IMAT	Intensity-Modulated Arc Therapy
IMRT	Intensity-Modulated Radiation Therapy
Inc.	Incorporated
KERMA	Kinetic Energy Released in the Medium
LINAC	Linear Accelerator
LQM	Linear Quadratic Model
MLC	Multi-Leaf Collimator
MME	Multiple Metastases Element

mMLC	Micro-Multi-Leaf-Collimator
MUD	Monitor Unit Distribution
MV	Megavoltage
NoVo	Noncoplanar VMAT Optimization
NSHA	Nova Scotia Health Authority
NTO	Normal Tissue Optimizer
OAR	Organs at Risk
PC	Personal Computer
PCA	Principal Component Analysis
PDD	Percent Depth Dose
PRO	Progressive Resolution Optimization
QA	Quality Assurance
QUANTEC	Quantitative Assessment of Normal Tissue Effects in the Clinic
RAO	Rotating Aperture Optimization
RT	Radiation Therapy
RTOG	Radiation Therapy Oncology Group
SA	Simulated Annealing
SAD	Source-to-Axis-distance
SBRT	Stereotactic Body Radiation Therapy
SLD	Sub-Lethal Damage
SSD	Source-to-Surface Distance
SRS	Stereotactic Radiosurgery
TORUS	Trajectory Optimization in Radiotherapy Using Sectioning
TMAT	Trajectory Modulated Arc Therapy
TPR	Tissue Phantom Ratio
TVMAT	Trajectory-based Volumetric Modulated Arc Therapy
USF	Urgent Sparing Factor
UAB	University of Alabama at Birmingham
VMAT	Volumetric Modulated Arc Therapy
XML	Extensible Markup Language
Z	Atomic Number

CHAPTER 1 INTRODUCTION

1.1 PREAMBLE

This thesis presents the optimization of the positions of mechanical devices which orient, shape, and control the intensity of the photon radiation beam emanating from a clinical electron linear accelerator designed to deliver precision radiation therapy on a patient-specific basis. By developing generalized optimization algorithms which catalogue all allowed scenarios for contextual cost, a customized solution can be produced with the aim of reducing radiation dose received by surrounding normal tissues.

In each of the major bodies of work in this thesis, the novel techniques developed for radiotherapy are compared with clinical standard expert-planned radiation therapy treatment plans to evaluate the dosimetric benefits and any resulting significant differences in clinically relevant metrics between approaches. The aim of this work is to contribute methods capable of automating advanced radiotherapy planning decisions associated with expert experience to mitigate inter-planner variability of plan quality and to replace templated approaches with patient-specific trajectory radiotherapy.

This research has direct utility in the improvement of radiation therapy in the treatment of cancerous and benign lesions in the cranium. With additional research to mitigate site-specific challenges, it is reasonable to expect its applicability to the improvement of radiation therapy treatment as applied in additional extra-cranial cancer sites. As of 2017, one in two Canadians will develop cancer in their lifetime and one in four will die of cancer. Cancer is the leading cause of death in Canada, responsible for 30% of all deaths [3]. The treatment for cancer is dependent on the anatomical site, pathology, and progression of disease, as cancer constitutes a multitude of diseases. The

three most common methods for treatment of cancer are surgery, chemotherapy, and radiation therapy, with over half of all cancer patients receiving radiation therapy as part of their treatment [3].

1.2 RADIATION THERAPY

Radiation therapy uses high-energy ionizing radiation to damage the deoxyribonucleic acid (DNA) in the cells of the tissue of patients to cure, control, or alleviate symptoms of disease. Radiation damages DNA directly, in the case of charged particle radiation, or, as in the case of electromagnetic radiation, interacts to create charged particles within the cell that in turn damage DNA [4]. Radiation is directed towards targeted tissues within the patient to attain a prescribed level of absorbed energy per unit mass, a quantity referred to as absorbed dose. It is the principle goal of radiation therapy to deliver the prescribed dose to the targeted tissues, while sparing the surrounding healthy tissues as much as possible. The difficult balance comes in maximizing this sparing without compromising the coverage of the prescribed dose to the tumour.

Radiation therapy delivery falls into two categories: external-beam radiation therapy (EBRT), in which radiation emanates from a machine outside of the patient; and internal radiation therapy (most frequently referred to as brachytherapy), in which radioactive material is inserted into, or in close proximity to, the tumor with varying duration, which depend on the activity, energy, and half-life of the radioactive material and the prescribed dose. This thesis focuses on radiation therapy technology delivered via photon EBRT on a linear accelerator (LINAC, see Figure 1). A linear accelerator generates a beam of photon electromagnetic radiation using microwave radiofrequency

fields (most frequently in the S-band at 2856 MHz [75]) to accelerate electrons before colliding them with a target composed of a high atomic number (Z) material. Deceleration of electrons in the target produces bremsstrahlung photons of a specified energy spectrum that depends on the initial electron beam energy and the elemental composition of the target. Section 2.2 contains an expanded description of the LINAC.

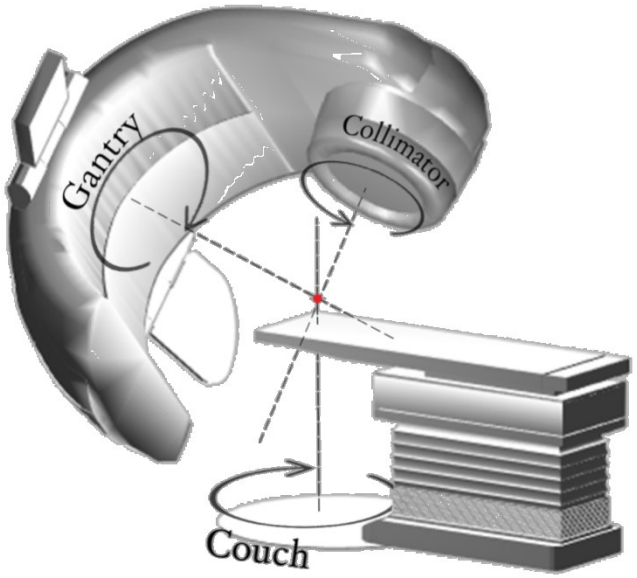

Figure 1: A depiction of the geometry of the linear accelerator highlighting some of the rotation axes, as well as machine isocentre (shown in red) where these rotation axes coincide.

To treat a tumor, megavoltage (MV) X-rays are used in the range of approximately 4 – 25 MeV. Energy deposition in tissue builds up over the first 1 - 4 cm of tissue, allowing the patient's skin surface to receive a fraction of the dose received at the maximum depth. A multitude of these beams can be aimed from different incident angles towards the targeted tissue, allowing dose to accumulate to a higher value where beams overlap at the target [5]. To further assist in localizing dose at the target, the radiation field can be shaped upon exit of the LINAC head by a collimation system. In modern C-arm linear accelerators, such as the Varian TrueBeam system (Varian Medical

Systems, Inc., Palo Alto, CA), this dynamic collimation system is comprised of two sets of orthogonally placed opposing jaws, and a multi-leaf collimator (MLC). The MLC is most typically comprised of two opposed banks of tungsten leaves, each individually motor-controlled to define a radiation aperture.

1.2.1 Radiobiology

Fractionated radiotherapy is the division of a treatment into several smaller recurrently delivered treatments which sum to the prescription dose. Fractionation is done to ensure efficacy of dose delivered to the tumor volume while reducing normal tissue effects in the surrounding tissue. There are four important radiobiological concepts to consider, denoted as *the four R's of radiobiology*:

- Repair: the increased cell survival due to sub-lethal damage (SLD) repair that is observed following irradiation.
- Repopulation: the increased cell survival resulting from cell division following irradiation.
- Reassortment: the increased cell death caused by the progression of cells from a radioresistant phase of the cell cycle during an initial irradiation to a more radiosensitive phase in the time interval between irradiations.
- Reoxygenation: the increased cell death caused by hypoxic cells becoming oxygenated and thus more radiosensitive following irradiation [15].

The efficacy of fractionated radiotherapy treatments depends on these concepts. Repair and repopulation increase tumor cell survival in the interim between irradiations, while reassortment and reoxygenation increase tumor cell kill [16]. Repair and repopulation also serve to mitigate cell damage to surrounding healthy tissues, providing

the ability for cellular recovery and proliferation in early-responding tissues after initial irradiations. A fifth 'R', radiosensitivity, is sometimes additionally included to consider the intrinsic response to radiation of the cells constituting a tumor [78].

In conventional fractionation regimes, the survival of irradiated cells can be modelled using radiobiological approximations of cellular DNA damage. The average yield of radiation damage can be approximated from the sum of lethal damage created by a single event, which is linearly related to the dose delivered, and interactions between multiple elements of sublethal damage events which become lethal, which is related quadratically to the dose delivered. Extended to a Poisson distribution of damaging events intersecting with a given cell, the survival fraction of cells can be approximated by:

$$S = e^{-(\propto D + \beta D^2)} \quad (1)$$

where S is the fraction of surviving clonogenic cells, α describes the linear component of cell survival, β describes the quadratic component of survival, and D is the fraction dose [15]. Cell survival in this sense is defined by the ability for cells to continue reproducing indefinitely. Cell death is the loss of this reproductive ability because of DNA damage by irradiation. This combination of linear and quadratic components of cell survival defines the linear-quadratic model (LQM). The components of cell death from each of these mechanisms can be visualized in Figure 2, where the linear component contributes more to cell death than the quadratic component until the intersection of the two functions at a dose value of $D = \frac{\alpha}{\beta}$, after which the quadratic component far exceeds the contribution from the linear component.

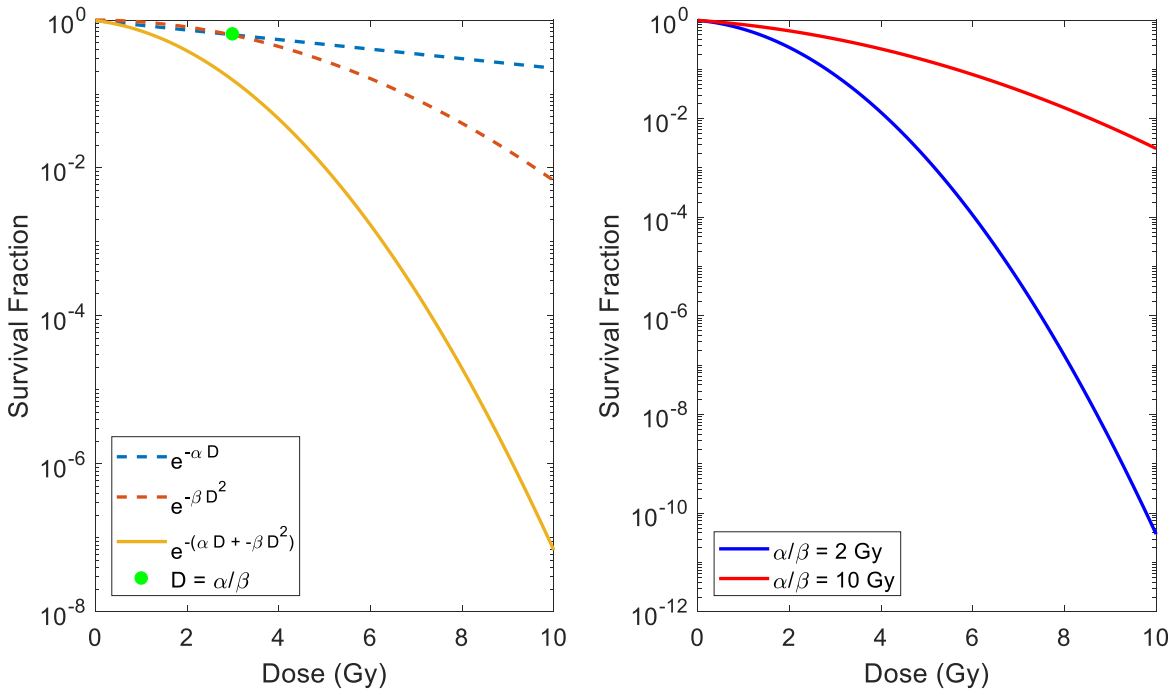

Figure 2: A) Components of the linear quadratic model contributing to cell death over the range of 0 to 10 Gy dose per fraction. The survival curves shown here are for α/β = 3 Gy. B) Comparison of a survival curve for α/β = 10 Gy and α/β = 2 Gy.

This intersection point, $\frac{\alpha}{\beta}$, is characteristic for different tissue types and is an indication of the survival fraction of a given tissue to a range of dose levels. Early-responding tissues possess high $\frac{\alpha}{\beta}$ ratios, meaning the linear component is dominant at the level of conventional doses per fraction. Conversely, low $\frac{\alpha}{\beta}$ ratios correspond to late-responding tissues which possess a higher contribution from quadratic components. Most tumors have a high alpha-beta ratio (approximately 10 Gy (Gray, a unit of dose measurement or J / kg, expanded upon in Section 2.1.2), and are early-responding tissues), however exceptions do exist in some common tumors, such as melanoma and prostate cancers, that possess lower-alpha beta ratios (as low as 1.5 Gy). Normal tissues in the cranium have characteristically low $\frac{\alpha}{\beta}$ ratios.

1.2.2 Delivery Techniques

In conformal radiation therapy techniques, such as three-dimensional (3D) conformal radiation therapy (3D-CRT), the collimation system is fit to the two-dimensional (2D) projection of the target volume. The position of the gantry is rotatable 360^{o} about an axis to allow different anatomical projections when viewed from the position of the radiation source, or beam's-eye-view (BEV). The gantry is repositioned to vary the incident approach angle of radiation, and the relative dose contribution from each beam can be weighted to improve the distribution of dose. This conformal method of delivery can additionally be extended to a dynamic arc-based approach, dynamic conformal arc (DCA), in which dose is delivered simultaneously with gantry rotation. The MLC is dynamically repositioned during DCA to retain its conformality with the projection of the target from each different viewing perspective in the arc.

Further computational advancements allowed for increased sophistication in the delivery of dose from fixed angles. Intensity-modulated radiation therapy (IMRT) uses the MLC to create multiple small beams of varying intensity that generate non-uniform fluence from any given position of the treatment beam to optimize the total dose distribution. The treatment criteria desired by the planner are defined in advance and the fluence profiles, and the MLC movements required to produce them, are determined through inverse-planning algorithms [7]. Although, due to the profile of the linear accelerator, it is not a viable option at all treatment sites, plan quality can be improved with the inclusion of non-coplanar incident beam directions [8]. By specifying a couch rotation angle along with gantry rotation angle, beam axes are no longer required to be confined to one single plane, thus increasing the total degrees of freedom.

IMRT was then extended from fixed fields to an arc, delivered in a continuously rotating field, the principles of which are incorporated in intensity-modulated arc therapy (IMAT) [9]. When developed commercially, this technique took the name of the specific highly efficient IMAT algorithm utilized [10], volumetric modulated arc therapy [11] (VMAT). VMAT has been repeatedly shown to produce similar or superior dose distributions with a decrease in treatment time when compared to IMRT and IMAT [11 12]. This increase in efficiency of delivery and dosimetric equivalence has made VMAT a widely used technique in cranial radiation therapy [12]. These advantages in the domain of normal tissue sparing are of benefit in hypofractionated treatments, such as stereotactic radiosurgery (SRS), where the number of fractions in which treatment is delivered is decreased and the dose per fraction is increased.

1.3 STEREOTACTIC RADIOSURGERY

1.3.1 Rationale and Radiobiology

Stereotactic radiosurgery (SRS) is a single-fraction procedure for treatment of intracranial lesions using stereotactic apparatus and techniques with multiple narrow beams of radiation delivered via noncoplanar arcs or fixed beams [7]. When the treatment is delivered in a few high-dose fractions it takes on the term stereotactic radiotherapy (SRT).

When a radiotherapy treatment is conducted in a single fraction, or a few high-dose fractions, the radiobiological models (as outlined in Section 1.2.1) describing the responses of tissues to irradiation must be modified. Song *et al.* [80] revisits the four R's of radiobiology in the context of hypofractionated radiotherapy with the following observations:

- Repair: a stereotactic procedure whose delivery is prolonged may result in considerable repair of sublethal damage in comparison to a treatment with a very short delivery time.
- Repopulation: it is likely that the shortened nature of the treatment results in repopulation playing little to no role in hypofractionated treatments.
- Reassortment: while fractionated treatments are capable of allowing cells to shift from radioresistant phases to the radiosensitive phases, it is likely that high-dose irradiation halts cell-cycle progression and interphase cell death occurs.
- Reoxygenation: single-fraction treatments are not able to exploit the advantage of reoxygenation of hypoxic cells that is seen in fractionated treatments.

In addition to DNA strand breaks and chromosome aberrations caused in conventionally fractionated radiotherapy, treatments with doses greater than 10 Gy per fraction are shown to cause severe vascular damage that results in a lack of oxygen supply from reduced blood perfusion, which in turn damages the intratumor microenvironment, and leads to indirect tumor cell death [17]. The nature of vascularity in tumors may create additional vulnerability to high-dose radiation damage compared to healthy tissues [79].

In terms of normal tissue sparing, the hallmark of radiosurgery is a rapid dose fall-off outside of the target volume leading to a dose distribution with a high conformity to the target, which in turn limits the exposure of surrounding healthy tissues. An additional requirement is that the size of cranial targets treated using stereotactic

radiosurgery are small. This means that the volume of healthy tissue surrounding the target receiving high dose in a conformal distribution is also small. Chapters 3 - 6 in this thesis focuses on the treatment of acoustic neuromas (vestibular schwannomas) and multiple brain metastasis. Acoustic neuromas are benign tumors that are the most common tumor in the extra-axial posterior fossa compartment in adults [19], with an average volume of 2.0 cm^3 [20]. Brain metastases are the instances of malignancies in the brain as a secondary site, and have an incidence rate of 10 per 100,000 in population-based studies [115]. This occurs when cancerous cells from a primary disease site metastasize to the brain and present as small, typically ellipsoidal, tumors. Single metastases tumors can occur, but frequently multiple tumor volumes also occur. Radiation Therapy Oncology Group (RTOG) 9508 makes prescription recommendations for treatment of brain metastases with SRS up to a maximum diameter of 4 cm. The RTOG 9508 recommended level of prescription dose increases with decreasing maximum tumor diameter (d): 15.0 Gy for 3 cm ≤ d ≤ 4 cm, 18.0 Gy for 2 cm < d < 3 cm, and 24 Gy for $d \leq 2$ cm [18]. This inverse relationship between dose and volume is indicative of the need for normal tissue sparing to the rind volume surrounding the tumor volume.

Brain metastases and malignant brain tumors are estimated to have high $\frac{\alpha}{\beta}$ ratios of approximately 10, while benign tumors have lower $\frac{\alpha}{\beta}$ ratios closer to 3. Normal tissues in the central nervous system are thought to have ratios close to 3 [16]. While there is uncertainty in the exactitude of $\frac{\alpha}{\beta}$ ratios in these tissues, the goal of SRS is high conformity and sparing of the normal tissues. The use of the LQM for dose fraction sizes

used in SRS has been a matter of debate due to validation of the model only in the dose range 1 to 5 Gy and the underestimation of tumor control by not incorporating the additional aforementioned mechanisms involved in tumor cell kill at high dose per fraction [16]. Expanded models have been proposed which add parameters to synthetically straighten the cell survival curve at higher dose per fractions to match cell survival observations [79].

The high dose per fraction delivered in SRS leads to very low cell survival fractions regardless of the $\frac{\alpha}{\beta}$ ratio, and observed data show that cell death exceeds those predicted in the LQM because of indirect tumor cell death from vascular damage, rendering the LQM inapplicable at high dose fractions. This increase efficacy of hypofractionated delivery further motivates the requirement for healthy tissue sparing by highly conformal dose distributions.

1.3.2 History of SRS

The delivery of conformal high dose single fraction radiosurgery for cranial lesions has been performed for two-thirds of a century and has gone through multiple generations of improvements in precision, localization, accuracy, and efficiency. The term radiosurgery was first coined in 1951 by Lars Leksell in his method for non-invasive destruction of intracranial lesions inaccessible for open surgery (see Figure 3) [13].

Figure 3: Neurosurgeon Lars Leksell (right) and physicist Borje Larsson (left) setting up a patient to receive SRS with a particle accelerator treatment in 1958 [105].

This initial work combined a frame for stereotaxy with delivery of orthovoltage (100 – 500 keV) X-rays for the treatment of trigeminal neuralgia. Stereotaxis involves a systemic approach to define a 3D coordinate system to aid with localization of anatomical sites in the cranium. Because the penetration of the orthovoltage X-rays was insufficient for treating targets above a certain depth, Leksell and a team of colleagues developed a radiotherapy unit based on a hemispheric array of cobalt 60 sources ($E_{ave} = 1.25\ MeV, T_{1/2} = 5.26\ years$). The utility of Co-60 as a radiotherapy source had been previously demonstrated by Johns *et al.* in August 1951 with the Saskatchewan Cobalt 60 Unit at the University Hospital in Saskatoon [21]. The first unit from the Leksell team, termed Gamma Knife (GK), was composed of 179 sources and was operational in the Sophiahammet Hospital in Stockholm in 1968 for the treatment of arteriovenous

malformations (AVMs) and acoustic neuromas (see Figure 4 for a cross-sectional diagram) [14]. The GK is currently manufactured by Elekta (Elekta AB, Stockholm, Sweden). The results of the first implementation were promising, and a second unit was installed at Karolinska Hospital in Stockholm in 1974. This second machine was the first to deliver circular fields making it more generally applicable to match a variety of tumor shapes. In addition, a revolution in stereotactic localization was produced with the advent of computed tomography (CT) which improved the ability to localize volumes to be treated with SRS [14]. CT imaging drastically improved the ability to localize tumor volumes compared to previous methods of planar x-ray acquisition as a means of stereotactic guidance. This technological step forward allowed Betti *et al.* in Buenos Aires, and Columbo *et al.* in Vicenza, to independently produce adaptations of the procedures delivered on the GK to a co-planar treatment on LINACs [111]. Additionally, in the 1980s McGill University in Canada is recognized as one of the first universities in North America to offer SRS using standard LINACs. The treatment quality comparison between GK and LINAC based SRS became a continued topic for debate, however dosimetric comparability between the methods has been shown [24].

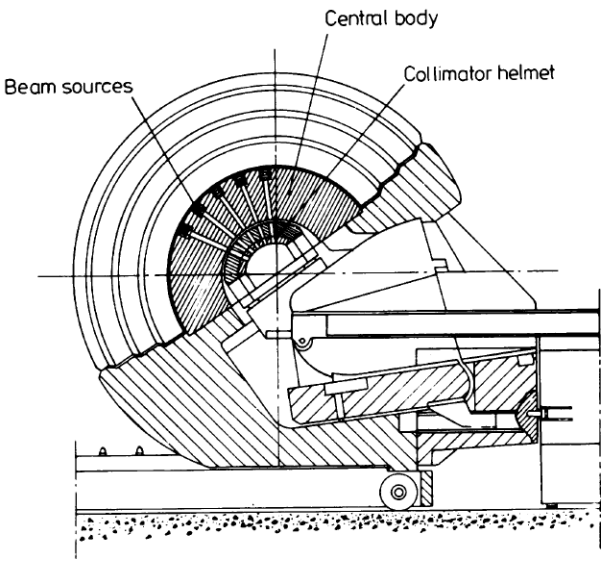

Figure 4: Cross-section of the configuration of a Gamma Knife with a multitude of cross-firing photon sources arranged with a central focal point. Image from Leksell *et al.* Stereotactic radiosurgery [14].

SRS was also propelled forward with the invention of increasingly efficient stereotactic frames. Leksell's initial stereotactic frame was surgically affixed to the patient skull and was advanced in 1985 by the Brown-Roberts-Wells (BRW) stereotactic frame [25]. The BRW frame's utility in combination with a 6 MV LINAC was first used with an adaptation by Winston & Lutz in 1988 [26]. In order to deliver fractionated radiotherapy without the repeated use of a surgically invasive frame, the less invasive Gill-Thomas-Cosman (GTC) frame, which relies on a patient-specific moulded bite-block, was developed [27]. Frameless systems have become the most common in fractionated SRS, with commercially available systems employing the use of thermoplastic mask moulds of the patient to reproducibly position the patient, and confirmation of target location through image guidance. Frameless systems using masks have been shown to have acceptable repositioning accuracy with errors below 3.0 mm [28]. Additionally, immobilization methods which combine thermoplastic moulds of the

back of the skull and vacuum fixation bite-block secured to a metal arch frame have been shown to have superior ability to limit intrafraction motion compared to alternative frameless systems [29].

In 1994, a dedicated stereotactic 6 MV LINAC named the Cyber Knife (CK), manufactured by Accuray (Accuray Inc., Sunnyvale, CA, USA), was devised by the neurosurgeon John Adler and engineers at Stanford University. The smaller scale X-band (8 to 12 GHz) wave-guide allowed the system to be mounted on a versatile industrial robotic arm and was capable of a much more diverse set of non-coplanar fixed incident angles than conventional C-arm LINACs.

Collimation systems on modalities used to treat SRS have made substantial improvements since their initial inceptions. The previously mentioned GK systems used a hemisphere of sources with conical collimation systems and variable field sizes of 4, 8, 14, or 18 mm. The GK Perfexion was released with modifications of this system that feature eight collimation partitions which were independently dynamic and contained 24 sources each (192 sources total). These field sizes are capable of blocking individual partitions to further customize the dosimetric patterns [108].

The first CK systems used a cone-based approach as well, with tungsten cones available between 5 and 60 mm. Later, an iris collimator was released, with two-stacked banks of six tungsten pieces which create a 12-sided aperture [108]. Finally, modern CK systems possess a high-definition multi-leaf collimator with 41 leaf pairs with a leaf width of 2.5 mm and maximum field dimension of 10 x 12 cm^2 at 800 mm source-to-axis-distance (SAD).

C-arm LINAC based approaches to SRS also featured a cone-based collimation system initially, with the offering of tungsten cones that generated field sizes of diameter from 4 to 45 mm in 2.5 mm increments. Brainlab AG (Brainlab AG, Munich, Germany) also developed a modular addition to the LINAC head with a fine resolution MLC for collimation called the m3 micro-MLC. Modern C-arm LINACs with the ability to treat SRS possess high definition MLCs, such as Varian's HDMLC120 with 60 pairs of leaves, the highest resolution of which have a 2.5 mm width at 100 cm SAD.

These three methods, GK, CK, and C-arm LINAC, represent the three most common methods of delivery of cranial SRS and are shown in Figure 5. Studies comparing these methods indicate similar distributions can be delivered on each modality, with planner experience being an asset on each. A 2011[81] study comparing the same multiple metastases treatments planned with all three modalities indicates an improved conformity and peripheral normal tissue dose at multiple dose levels with GK treatment, compared to CK and the C-arm LINAC with Brainlab Novalis stereotactic system. The maximum doses in targets were higher for Gamma Knife for all cases. A 2014[82] study similarly compared the GK, CK, Novalis, and Varian TrueBeam LINAC in flattening-filter-free (FFF) mode for multiple metastases plans. GK hotspots were higher than all other modalities with lower normal brain peripheral dose. The trends for delivery time from comparative studies indicate the ranking of modalities as C-arm FFF, C-arm, CK, and GK in order of increasing delivery time. A nine metastases treatment plan on each modality was delivered in 8.16, 57.68, 85.95, and 124.70 minutes for the C-arm FFF, C-arm, CK, and GK, respectively [82].

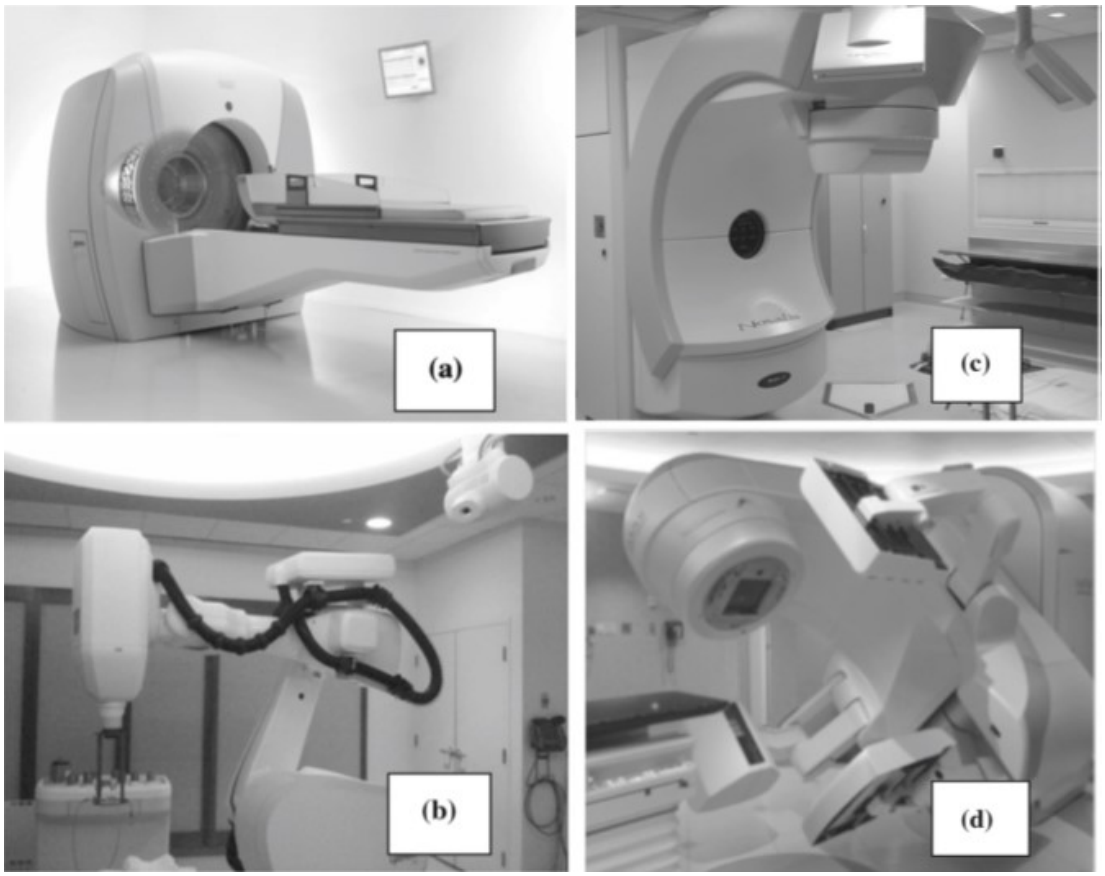

Figure 5: Images of the described delivery methods for SRS (a) Elekta Leksell Gamma Knife Perfexion (b) Cyber Knife LINAC, (c) Brainlab Novalis C-arm LINAC, (d) Varian TrueBeam C-arm LINAC [82].

1.4 TRAJECTORY PLANNING OPTIMIZATION

1.4.1 History of Plan Optimization

Radiotherapy planning optimization departs from the strict mathematical definition of optimization, which seeks the best possible solution to a plan, for the accepted definition in medical physics of the iterative improvement of important radiation treatment plan metrics due to the available degrees of freedom in developing radiotherapy plans. With this definition, a plan that has been optimized does not infer that there exists no possible dosimetrically superior plan, but that the plan has reached a local optimum within the planner's specified priorities. Medical physicists have been

developing novel technology for the optimization of dose distributions through computationally automated and manual means since as early as 1955 [30 31]. Within the realm of LINAC EBRT, computational optimization in radiotherapy became more viable with the invention of complex modulated delivery techniques beginning in the 1980s and the rise of computational power as provided by personal computers. With the optimization of fluence maps with thousands [30] of potential beamlet intensities per treatment plan, the combination of possibilities far-exceeded the capacity for manual iteration of all possible plans. Automated plan optimization methods became an area of focus thereafter with a host of new technologies being implemented clinically. Substantial pioneering work in the optimization of distributing and weighting beams in fixed beams was conducted by Brahme in the late 1980s [43]. Solutions for applying simulated annealing (SA) to radiotherapy [32], computational solutions to generate plans for user-supplied dosimetric qualities (inverse planning, prior to which beam arrangements and MLC configurations would be decided in advance in forward planning techniques) [33], generation of fluence maps from the sequencing of multi-leaf collimators [34, 35, 36], and efficient methods of directly optimizing beam shapes (through direct aperture optimization (DAO)) and weights while controlling aperture complexity [37], enabled IMRT to become a state-of-the-art and widely adopted radiotherapy method in demanding settings in the late 1990s and early 2000s.

Outside of the optimization of fluence patterns to generate dose distributions, the definition of incident beam angle directions, or beam angle optimization (BAO), was another optimization parameter in IMRT. The problem of optimal fixed beam angle becomes intractable to try to solve via brute force. Sampling a 360^{o} coplanar arc by 10-

degrees, producing 36 candidates, and solving from these 36 candidates an optimal 7-field bouquet yields 8,347,680 possibilities. [38] A manual trial-and-error approach leaves the planner likely to miss possibilities approaching optimality in favor of the local optimum in the group of combinations attempted. The search for optimal beam arrangements is thus best suited for computational methods. However, even modelling the dosimetric consequences of more than eight million possible configurations is computationally intensive, providing the motivation for technologies approximating dosimetric consequences of beam selections. Rowbottom *et al.* [39] developed a method to sparsely sample dose voxels by using randomly selected subsets of contained voxels to represent entire structures. Pugachev *et al.* [40, 41] used a heuristic approach of incorporating BEV information to rank the utility of beam directions for use in a solution. Stein *et al.* [42] deployed a SA algorithm to optimize the number and orientation of beams in a solution and found that the benefit of optimization of IMRT beam locations diminishes with increasing number of beams and has greatest benefit with few beams. Bortfeld *et al.* [44] applied SA in a frequency-domain based optimization of beam orientations and concluded that optimality of multiple-beam irradiations with more than three beams is generally the even distribution of these beams over an angular range of 0 to 2π, additionally adding that large numbers of beams (seven to nine) show limited improvement with optimization. It is this concept of even distribution of beam orientations adequacy in modulated settings that validates the use of template arrangements of beams in fixed beam techniques and arcs in rotation-based techniques.

A cranial stereotactic VMAT template employed and developed by the University of Alabama [45] involves distributed sampling of a 2π steradian space with four arcs: one

full axial coplanar rotation, two half arc rotations 45° from the axial plane, and one-half arc at the vertex plane orthogonal to the axial plane. The latter three arcs mentioned are accomplished by means of couch rotations away from the axial plane. The extension of BAO to arc-based deliveries involves a departure from this template approach to find patient-specific solutions, or solutions which incorporate coordinated motion of the LINAC components in a temporal choreography, or trajectory. Frequently, to greater sample the available portion of the total 4π steradian space, these trajectories involve simultaneous motion of the couch and gantry.

1.4.2 Approaches to Trajectory-Based Radiotherapy

Non-coplanar radiotherapy using simultaneous couch and gantry motions dates back as far as 1988 in studies performed by Podgorsak [46] at McGill University in Montreal. Dynamic radiosurgery, as presented by Podgorsak, employed a 330° rotation of the gantry concurrent with a 150° rotation of the couch. Compared to conventional coplanar methods, the dynamic method showed a considerable increase in the slope of dose fall-off outside of the target. While this technique was not widely accepted, 30 years later, the availability of digital control systems within linear accelerators and dosimetric optimization has led to a resurgence of investigation in the area. Numerous planning studies with test patients have emerged illustrating the advantages of non-coplanar beam arrangements that minimize dose to healthy tissues and increase dose conformity to the target.

The motivation for the research in this thesis has come from Yang *et al.*'s publication in 2011 [47] that uses a 2D overlap map, generated via a cost equation, to design non-coplanar couch and gantry trajectories for VMAT. Their method designed

short sub-arc trajectories using hierarchical clustering and was implemented and evaluated on an in-house system against standard non-coplanar VMAT and non-coplanar IMRT. The study found that dynamic trajectories lowered the maximum dose to organs-at-risk (OARs) and increased target conformity with comparable beam-on time to standard VMAT.

Later that year, Shaitelman *et al.* [48] applied dynamic couch rotation to accelerated partial breast irradiation (APBI) with a couch arc and fixed gantry. The dynamic method significantly reduced OAR doses when compared to 3D-CRT. Additionally, the dynamic approach used significantly fewer monitor units than 3D-CRT, IMRT, and VMAT.

Two studies by Dong *et al.* in 2012 and 2013 [49, 50] on non-coplanar treatments for treatment of lung and liver provide some of the most developed implementation of non-coplanar optimization to date. Additionally, this work first refers to non-coplanar beam optimization as 4π radiotherapy, the now colloquially accepted term. Beginning with a very large set of potential fixed beams, their algorithm reduces the number of included beams using a greedy column generation method until the improvement has reached a status of diminishing return. These studies show significant OAR dose reduction, improved dose gradient, and reduced high dose spillage when compared to conventional VMAT. These treatments are delivered with high numbers of non-coplanar fixed beams and do not incorporate dynamic couch motion.

In 2013, Fahimian *et al.* [51] applied dynamic couch motion to APBI with a prone breast setup delivered on the TrueBeam LINAC system in Developer Mode (a linear accelerator delivery mode that enables researchers access to advanced control features

not typically accessible in clinical LINAC modes; see Section 2.2.2). The trajectories delivered were non-isocentric and employed both dynamic couch rotations and translations. This technique showed improvement of dose conformity and associated dose-volume parameters correlated with toxicity. Popescu *et al.* [52] also applied dynamic couch arcs with simultaneous non-coplanar gantry motion to APBI in 2013. This technique resulted in superior target coverage and decreased dose to normal tissues when compared to VMAT.

Rodrigues *et al.* [53] developed dynamic electron arc radiotherapy (DEAR) in 2013, which combines simultaneous couch and gantry motion with dose rate modulation to achieve desirable dose distributions. This technique also makes use of Varian's Developer Mode on the TrueBeam platform. DEAR showed promise as a treatment of conformal radiotherapy of superficial tumors with acceptable dose homogeneity.

Another publication featuring the introduction of dynamic couch rotation in VMAT treatments was published in 2013 by Smyth *et al.* [54] as applied to partial breast, brain, prostate only, and prostate and pelvic nodes. The study used ray tracing to determine the number of OAR voxels intersected for each potential source position and constructed a 2D map. The map was then used to generate dynamic trajectories using Dijkstra's algorithm [109]. The results of this optimization showed substantial reduction of dose to specified OARs compared to otherwise comparable coplanar VMAT techniques.

In 2014, the first paper was published on the quality assurance (QA) requirements for dynamic couch trajectories [55]. Tests were designed to evaluate positional accuracy, velocity constancy, and accuracy for dynamic couch motion under a realistic weight load. These tests were written and deployed using Varian's Developer Mode. The study

showed that the couch rotational accuracy was within 0.3° with 0.04 cm displacement of the rotational axis. Accuracy for complex delivery involving MLC and couch motions was within 0.06 cm. The conclusions reached were that Developer Mode can deliver dynamic treatments with acceptable geometric and dosimetric fidelity.

In 2015, several studies in the area of dynamic couch and gantry methods were published, one of which was the first from our research group [60]. This study focused on the optimization of a heterogeneous population of cranial VMAT cases optimized via geometric overlap maps. Dynamic trajectories across one full gantry rotation were generated using a customized algorithm that includes parameters for limiting total couch motion, inclusion of absolute minimum values of overlap, and clinical practicality. These trajectories were sampled to comply with VMAT restrictions into 10 sub-arcs, which together constitute a complete gantry rotation, with couch angles corresponding to the minimum accrued total objective function score. This optimization resulted in significant OAR maximum dose sparing without significant degradation of target metrics. The methods used in this manuscript will be further expanded in the second chapter of this thesis.

Liang *et al.* [56] applied trajectory modulated arc therapy (TMAT) to APBI in prone setup via Developer Mode. These trajectories included dynamic couch rotations and translations. In 10 breast test-patient cases, the volume of normal breast receiving multiple isodose levels significantly decreased compared to 6-field non-coplanar IMRT. Additionally, delivery time was more efficient for TMAT compared to IMRT.

Papp *et al.* [57] applied simultaneous couch and gantry rotations to non-coplanar VMAT to create a reliable optimization method for isocentric arc therapy plan

optimization. Beam directions were defined using an iterative beam selection heuristic that served as anchor points to the trajectory. A combinatorial optimization was then used to define an efficient means of visiting each anchor point. The application of these trajectories to challenging extracranial stereotactic treatment in the lung (also known as stereotactic body radiation therapy (SBRT)) and brain cases revealed that the large number of angles utilized by isocentric noncoplanar VMAT improves dose conformity, homogeneity, and organ sparing using the same beam trajectory length and delivery time as coplanar VMAT.

In 2015, Wild *et al.* [58] published a comprehensive comparison of nasopharyngeal treatment plans using both coplanar and non-coplanar geometries, and additionally compared them to a benchmark 4π plan with approximately 1400 noncoplanar beams. This study confirmed the dosimetric benefits of noncoplanar irradiation and found that IMRT using optimized non-coplanar beams and VMAT using optimized non-coplanar trajectories resulted in substantial dose reductions to OARs.

Non-coplanar trajectories have additionally been developed for systems other than the C-arm linear accelerator, such as Brainlab's Dynamic Wave Arc (DWA) on the Vero SBRT system (Burghelea *et al.* [59]). Wave arc trajectories were created for 31 patients with various anatomical tumor locations. The technique significantly lowered maximum dose to proximal OARs and reduced delivery time compared to IMRT. The technique also produced a steeper dose gradient outside the target.

In 2016, Smyth *et al.* [61] applied three non-coplanar VMAT trajectory methods to fifteen patients with primary brain tumors. A geometric heuristic technique was compared to a fluence-based local search and a hybrid of the two methods in order to

outline the advantages and disadvantages of each approach. The heuristics method best spared the OARs and reduced normal tissue complication probability, however, the incorporation of fluence into non-coplanar trajectory optimization best maintained planning target volume (PTV) homogeneity.

Wilson, Otto, and Gete presented trajectory-VMAT (TVMAT) in 2017 [62] for SRS that applied a beam trajectory formed by dynamic motion of the treatment couch and the gantry. While the couch swept through 180 degrees, the gantry swept through two to eight partial arcs, changing the degree of sampling of the 4π space. Dose rate and MLC sequence were modulated throughout this trajectory using inverse planning. The result was an efficient dynamic delivery which showed dosimetric accuracy, significant sparing of surrounding normal tissues, and improvements to dose fall-off outside the target, homogeneity, and conformity.

Later that year, Wilson and Gete also published a paper [63] on the quality assurance for treatments with dynamic couch rotations. Comparisons of LINAC log files and DICOM header information of couch angle values showed agreement, consistency of couch centre of rotation was within 0.7 mm, and couch star-shot measurements with film-based measurements gave agreement within 0.2 mm. This study showed that the treatment couch has consistent accuracy with treatments in both fixed and dynamic deliveries.

In 2017, Yu *et al.* [64] applied the method from Dong *et al.* (2012 and 2013) to high-grade glioma patients to evaluate the dosimetric benefit and efficiency of 4π optimization. In nine of the eleven patients analyzed, mean and maximum OAR doses were equal or significantly reduced with 4π when compared with a standard VMAT

template. Substantial reduction was noted in the brainstem maximum dose, which would allow for treatments that would otherwise not satisfy safe dose constraints with VMAT. Average delivery time with this method was still substantially more than VMAT at 34.1 minutes.

Langhans *et al.* [65] published their method, noncoplanar VMAT optimization (NoVo), which used geometric considerations to rank usefulness of the whole beam space, and, starting with many beams, eliminated beams based on examined fluence contributions. A custom path finding algorithm was applied to find an optimized continuous trajectory through the most promising beam angles. Nine-beam IMRT, a full 4π IMRT solution, non-coplanar VMAT, non-coplanar VMAT plan produced using the algorithm of Papp from 2015, and the NoVo technique were compared. The NoVo technique comes the closest dosimetrically to the full 4π plan, as well as improving the solution time.

While the last decade has produced many publications in the space of dynamic couch and gantry trajectories, limited research exists in the space of dynamic collimator rotations designed for VMAT or DCA treatments. Rotating aperture optimization (RAO) research has been conducted by groups in the past fifteen years (Siochi 2004[66], Otto & Milette 2005 & 2010 [67 68]). A manuscript was published in 2010 by Milette & Otto [69] that applied dynamic collimator rotation to DAO, generating RAO. The study showed treatment plans with RAO were as good as or better than DAO, while maintaining a smaller number of apertures and MU than fluence-based IMRT. RAO technologies were designed for fixed-gantry solutions to achieve an increase in MLC resolution beyond which is normally possible due to the finite width of MLCs (typically 2.5 – 5 mm).

In 2005, Lee *et al.* [73] examined the effect on surrounding healthy tissue in the brain from static and dynamic collimator optimization when using a micro-multi-leaf collimator (mMLC) in dynamic arc SRS. By comparing three collimator configurations in thirty patients (static collimation fixed at 90° throughout the treatment, static collimator optimized for each arc, and dynamic collimator optimized every 10 degrees throughout treatment arcs), the study found that dynamic collimator optimization significantly increased dose conformity at three dose levels compared to static solutions. Optimality of the collimator was defined by total aperture area minimization. Additionally, the authors developed a method of linear and polynomial interpolation for collimator trajectories.

An arc-based dynamic collimator solution was developed by Webb *et al.* in 2010 [70], as applied to the Elekta LINAC Beam Modulator MLC (Elekta AB, Stockholm, Sweden). The approach aims to minimize the number of parked gaps between leaves which are needed for certain gantry orientations. This optimization was able to mitigate 40% of the leaf gaps compared to standard delivery.

Zhang *et al.* [71] also implemented dynamic collimator trajectories in VMAT treatments, using the methods developed in Yang *et al.* (2011), [47] concurrently with couch trajectories. This work aimed to ensure effective collimation in paraspinal SBRT using principal component analysis (PCA) to calculate the primary cord orientation. The collimator angle was then aligned so that MLC travel is parallel to the PCA-derived direction. The result was a technique that can improve target coverage and cord sparing but is not generalizable for application in other treatment settings, nor does it catalogue the efficacy of all valid possible collimator angles and compose a trajectory for every control point.

In 2017, Locke and Bush presented a novel approach called trajectory optimization in radiotherapy using sectioning (TORUS) [72] as a solution to issues of aperture connectedness when increasing resolution of samples in Varian's progressive resolution optimization (PRO) for VMAT optimization. TORUS generates trajectories via a score-map that incorporates aperture connectedness throughout the treatment plan and coordinates the dynamic axes to create plans which outperform both 7-field IMRT and 2 arc VMAT plans when comparing delivery time, OAR sparing, conformity, and homogeneity.

1.5 Research Objectives

This thesis presents novel investigations into the degrees of freedom on the C-arm LINAC as opportunities for the improvement of radiotherapy treatment plan quality with specific application to cranial SRS. The metrics of treatment plan quality which are addressed in this thesis are the doses to the surrounding healthy tissues and total amount of monitor units required to potentially reduce treatment delivery time. This research focuses on making these improvements in the treatment of both benign and malignant tumors in the cranium. In the context of benign indications, there is expected long-term survival of the patient after irradiation making sparing of surrounding normal tissue imperative to reduce the probability of normal tissue complications. In malignant cases, retreatments or additional treatments to proximal sites motivates technologies which control normal tissue doses in SRS. A reduction to the total monitor units, and by extension, duration of treatment plan, reduces the potential window to allow patient intra-fraction motion during the course of treatment. Additionally, these improvements must not come with the deterioration of metrics for the targeted tissues. While this work is one

specific embodiment, the fundamentals behind each of these methodologies is extendable to other SRS modalities and extra-cranially.

The work presented here is unique from all works previously stated in Section 1.4.2 as it applies a principle of cataloguing all possibilities into contextualized novel solution space, applies novel trajectory algorithm methods to navigate this space, implements plans in clinically accepted treatment planning systems, and compares to state-of-the-art conventional practice. These optimization techniques are conducted without the need to recalculate fluence or dose with a given iteration, alleviating the computationally intensive task and creating efficient methods. In all works except Chapter 5, there is no dosimetric optimization in axes trajectory definition, only geometric considerations, which is not directly translatable to dose. This strategy is chosen due to its computational efficiency compared to fluence based optimization. This thesis consists primarily of a series of manuscripts, each addressing a key research objective as follows:

- **Manuscript 1 presented in Chapter 3**. This manuscript addresses the investigation of dosimetric improvements with optimization of fixed couch rotation position in sixteen acoustic neuroma patients treated with stereotactic radiotherapy. All plans were compared with expert-planned conventional VMAT plans. The development and refinement of multiple novel algorithm factors for radiotherapy planning are described within.
- **Manuscript 2 presented in Chapter 4**. This manuscript builds on fundamental optimization methods of cost function map generation designed in Chapter 3 (Manuscript 1) and applies them to address the development and implementation

of a dynamic collimator rotation positioning algorithm based on a novel suitability metric, capable of general application in any radiotherapy BEV. The algorithm is applied to seventeen multiple metastases cranial SRS patients to reduce the non-target anatomy present in the BEV and improve overall treatment efficiency of monitor units. All plans were compared with expert-planned conventional VMAT plans.

- **Manuscript 3 presented in Chapter 5**. This manuscript increases the utility of the technology developed in Chapter 4 by developing a new automated radiotherapy aperture and dose modulation technique, intra-arc binary collimation (iABC) aimed at maximizing the presence of conformal apertures in multiple metastases settings, while meeting complex varied prescriptions, and sparing normal tissues. This method is compared to expert-planned conventional VMAT plans in seven multiple metastases patients.
- **Manuscript 4 presented in Chapter 6**. This manuscript addresses the synergistic properties of the optimization of couch rotation (as conducted in Chapter 3) and collimator rotation (as conducted in Chapter 4) together in an automated novel treatment planning procedure: combined optimization of dynamic axes (CODA). The process is applied to seven treatment plans with challenging three-target and four-target artificial patient geometries and compared to expert-planned conventional VMAT plans.

The second chapter of this thesis describes the background theoretical concepts of optimization metrics, objective functions, algorithms, and concepts used to accomplish

the work presented. The seventh chapter concludes the thesis by summarizing the key findings of the manuscripts and hypothesizes on future work.

CHAPTER 2 THEORY

This chapter presents a conceptual primer for the remainder of the thesis, offering an introduction to the theoretical and methodological tools used in the work. Firstly, the fundamental concepts of radiation energy transfer to matter will be outlined in Section 2.1, followed by an outline of the methods and materials used in completion of this research in Section 2.2 and 2.3.

2.1 PHOTON INTERACTION, CALCULATION, AND OPTIMIZATION

Radiation transfers its energy to an attenuating medium through mechanisms dependent on its energy relative to the required threshold for atomic ionization, possession of electromagnetic charge, probability of interaction, and material of the absorber. Radiation with energy capable of exciting orbital electrons to higher-energy states or removing negatively charged orbital electrons leaving a residual positively charged atom (ion pair) is known as ionizing radiation. Ionization radiation can be separated into two categories:

- Directly ionizing: Radiation possessing electric charge (e.g. electrons, protons, α-particles, and heavy ions) which carry sufficient kinetic energy to directly produce ionizations and excitations through the transfer of energy through many small interactions along the particles' path.
- Indirectly ionizing: Uncharged radiation (e.g. photons and neutrons) which transfer their energy to matter in a two-step process. Initial interactions transfer energy to charged particles which in turn directly create ionizations.

This thesis focuses solely on delivery of radiation therapy using photons in the megavoltage (MV) range. As such, this section will focus on the dominant interactions of this nature.

2.1.1 Photon Interactions

For a narrow beam of monoenergetic number of N photons incident on a thickness of attenuator dx, the total reduction by attenuation, dN, is proportional to a constant μ:

$$dN = -\mu N dx \quad (2)$$

Translated in terms of intensity, I:

$$dI = -\mu I dx \quad (3)$$

$$\frac{dI}{I} = -\mu dx \quad (4)$$

Which, when integrated, gives:

$$I(x) = I_0 e^{-\mu x} \quad (5)$$

where I_0 is the initial intensity of the photon beam. This proportionality constant, μ, expressed in units per unit length (cm^{-1}), is the linear attenuation coefficient. The attenuating properties of a medium depend not only on the thickness, x, but on the physical density of the material. To remove the density dependence, we can divide the linear attenuation coefficient by this density, yielding the mass attenuation coefficient μ/ρ, expressed in units of cm^2/g.

If we are measuring a fraction of the incident photon intensity transmitted through a medium, $I(x)$, there must be a complimentary fraction of the beam attenuated. This fraction of initial energy has been transferred in interactions with charged particles, which may have the capacity to create ionization or excitation events. The photon energy

transferred to kinetic energy of charged particles per unit thickness of the absorber is μ_{tr}/ρ, the mass energy transfer coefficient. A fraction of this energy, g, is transferred away from the local volume via bremsstrahlung interactions with the nuclei and thus doesn't contribute to dose locally. The fraction of energy retained in the local volume is thus (1 - g), and the corresponding net transfer coefficient, $\frac{\mu_{en}}{\rho}$, for this energy is $\frac{\mu_{tr}}{\rho}(1-g)$, known as the mass energy absorption coefficient.

The total attenuation of photons in matter is primarily caused by four interactions: the photoelectric effect, Compton scattering, pair production, and Rayleigh (coherent) scattering. The total mass attenuation coefficient is thus the sum of the individual coefficients for these interactions:

$$\frac{\mu}{\rho} = \frac{\tau}{\rho} + \frac{\sigma}{\rho} + \frac{\kappa}{\rho} + \frac{\sigma_R}{\rho} \qquad (6)$$

where $\frac{\tau}{\rho}$ is the contribution from the photoelectric effect, $\frac{\sigma}{\rho}$ is the contribution from the Compton effect, $\frac{\kappa}{\rho}$ is the contribution from pair production, and $\frac{\sigma_R}{\rho}$ is the contribution from Rayleigh scattering. As Rayleigh scattering contributes no energy transfer in the medium, but only the re-irradiation of incident photons at small scattering angles, this interaction is of limited importance in radiotherapy and will not be expanded upon here.

The remaining three principle interactions responsible for the transfer of energy from photons to matter are each dominant over specified photon energy ranges and atomic number of absorbing material. Figure 6 illustrates the range over where each of these interactions is dominant.

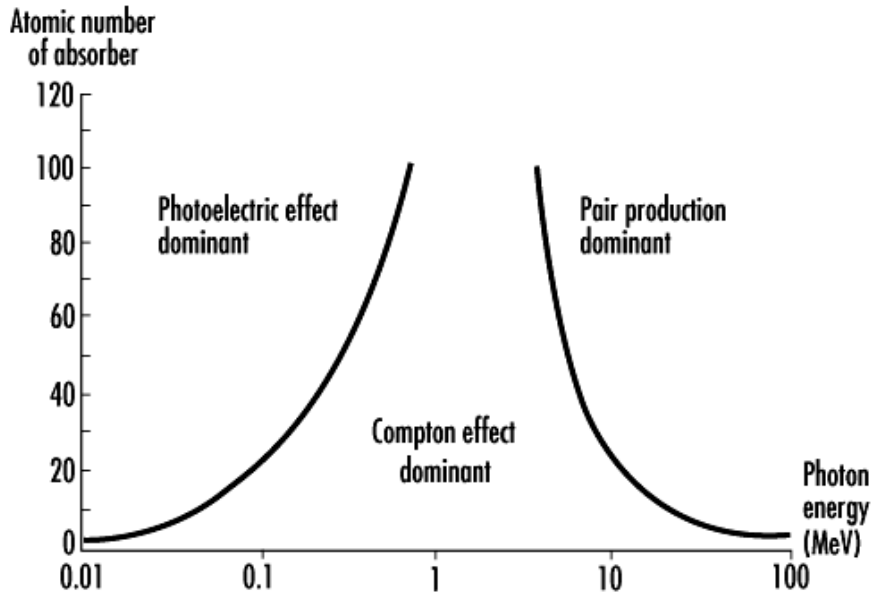

Figure 6: Relative importance of each of the three most important photon interactions for transferring energy to matter. The lines indicate where the interactions are equal in dominance. http://www.ilocis.org/documents/chpt48e.htm

As can be seen from Figure 6, the photoelectric effect is the most dominant interaction at low photon energy photon ranges and materials with high atomic numbers. In the photoelectric effect, an incident photon of energy $h\upsilon_0$, interacts with an orbital electron bound with potential energy E_b. The requirement for this interaction is that $h\upsilon_0 > E_b$ to remove the orbital electron from its bound state. The incident photon is totally absorbed in this interaction, and the net energy, T, is transferred to the electron as it is ejected from the atom as a photoelectron:

$$T = h\upsilon_0 - E_b \quad (7)$$

This photoelectron leaves a vacancy in the orbital shell, which can be filled by an outer shell electron resulting in the emission of a photon with energy equal to the net difference between binding energies, also known as a characteristic photon. This interaction can also produce Auger electrons, which are monoenergetic electrons

produced by the absorption of characteristic photons by the atom and re-emission of the energy in the ejection of orbital electrons. This is depicted in Figure 7.

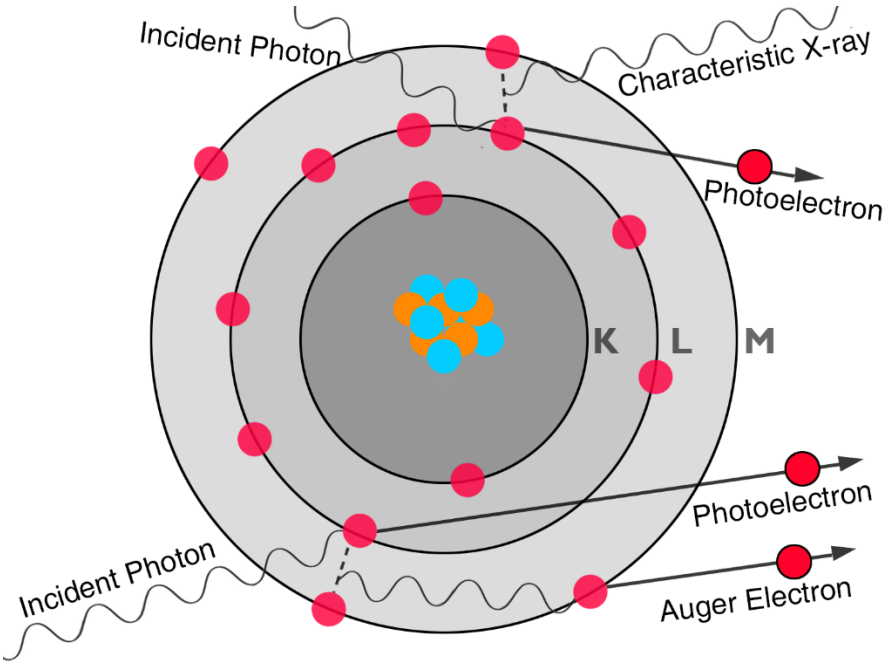

Figure 7: The photoelectric effect. An incident photon is totally absorbed and transfers its energy to an orbital electron, less the energy required for the electron to be unbound. The electron will create a vacancy, which when filled by an outer shell electron yields characteristic x-rays. When absorbed by the atom, these x-rays can result in the ejection of an Auger election.

The contribution of the photoelectric effect to the total mass attenuation coefficient has a strong dependency on energy and atomic number as:

$$\frac{\tau}{\rho} \propto \frac{Z^3}{h\upsilon_0{}^3} \qquad (8)$$

where $h\upsilon_0$ is the incident photon energy [7]. The strong dependence on the atomic number of the attenuator is the reason for differentiation between soft tissues and bone in diagnostic imaging where the energy of the x-rays is in the range in which photoelectric interactions are dominant. As the photoelectric effect has an inherent threshold regarding the binding energy of orbital shells, there exist sharp discontinuities in the photoelectric component of mass attenuation coefficient when the photon energy exceeds the binding

energy of each threshold. These sharp increases in value are denoted absorption edges. This increase in attenuation can be used as an advantage by introducing media (such as iodine or barium) which have a k-edge in the mean energy range of diagnostic x-ray spectra to enhance contrast in images.

The Compton effect is the photon interaction that is dominant at therapeutic photon energies in tissues. In this interaction, the incident photon interacts with an electron assumed to be 'free' or unbound, however the only requirement is that the electron's binding energy be much less than that possessed by the incident photon. The electron is transferred a fraction of the incident photon's energy and is scattered at an angle θ. The photon retains a fraction of the energy and is scattered at an angle φ. The kinematics are depicted in Figure 8.

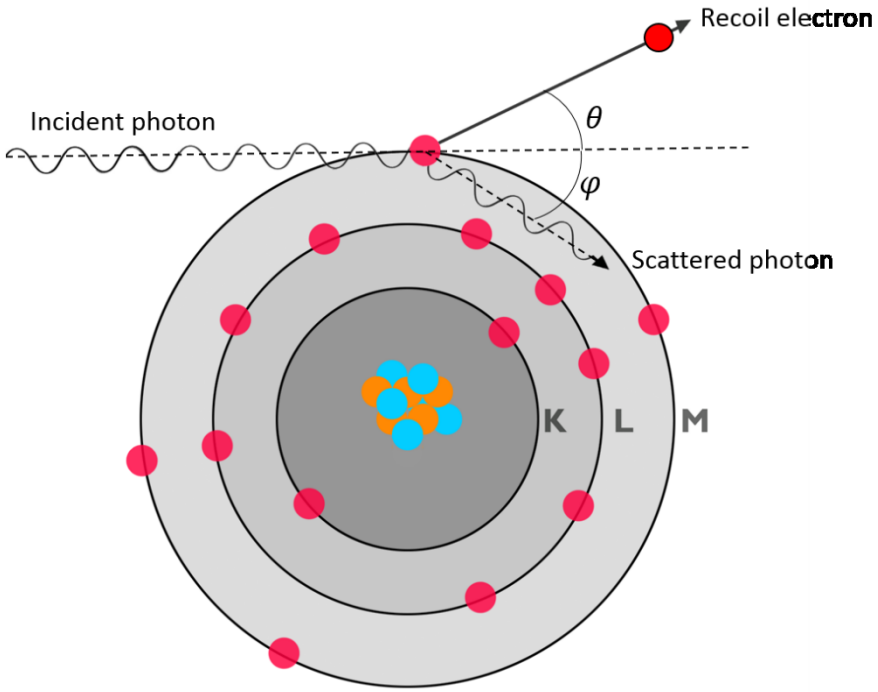

Figure 8: The Compton effect. An incident photon interacts with a free electron, or electron bound with an energy much less than that possessed by the incident photon, scattering it at an

angle θ relative to the direction of the incident photon. The photon is also scattered at an angle φ on the opposite side of the original direction, in the same plane.

If this interaction is examined as a collision of two particles, and the laws of conservation of energy and momentum are applied, the following can be derived for the scattering angles and recoil energies:

$$E = h\upsilon_0 \frac{\alpha(1-\cos\varphi)}{1+\alpha(1-\cos\varphi)} \quad (9)$$

$$h\upsilon' = h\upsilon_0 \frac{1}{1+\alpha(1-\cos\varphi)} \quad (10)$$

$$\cot\theta = (1+\alpha)\tan\frac{\varphi}{2} \quad (11)$$

where E is the energy of the Compton electron, $h\upsilon_0$ is the energy of the incident photon, $h\upsilon'$ is the energy of the scattered photon, and $\alpha = \frac{h\upsilon_0}{m_0c^2}$, where m_0c is the rest mass of the electron (0.511 MeV) [7].

Since Compton interactions involve essentially free electrons ($h\upsilon_0 >> E_b$), it is independent of the atomic number of the attenuating material. The Compton effect is the dominant photon interaction in the therapeutic range contributing to the deposition of dose in tissues.

Pair production is the third photon interaction and is dominant in the high photon energy range. In this interaction, the photon interacts strongly with the electromagnetic field of the atom's nucleus and gives up its total energy in the creation of a particle (electron) and anti-particle (positron) pair. This is a process of energy conversion to mass, and as the rest mass of the electron and the positron are identical at 0.511 MeV, the process cannot occur if the photon energy is below twice this mass, 1.022 MeV (see Figure 9). Any incident energy above this threshold is shared between the two created

particles. The positron then loses this energy gradually through ionizations, excitations, and bremsstrahlung before combining with a free electron in its vicinity, producing two annihilation photons departing from each other at approximately 180°, although residual kinetic energy of the positron can cause non-collinearity, each equal to the rest mass of one of the annihilating particles, 0.511 MeV. Above the threshold for this interaction, the energy dependence sharply rises, eventually reaching a plateau at higher energies.

As pair production is caused by the interaction of a photon with the electromagnetic field of the atom's nucleus, the process increases in likelihood with increasing atomic number at a rate of approximately Z^2 [7].

2.1.2 KERMA and Absorbed Dose

In the previous section, the mechanisms by which the indirectly ionizing photon transfers its energy into the attenuating medium were reviewed. The concepts and units used to describe the transfer of energy from radiation to volumes of matter are presented herein.

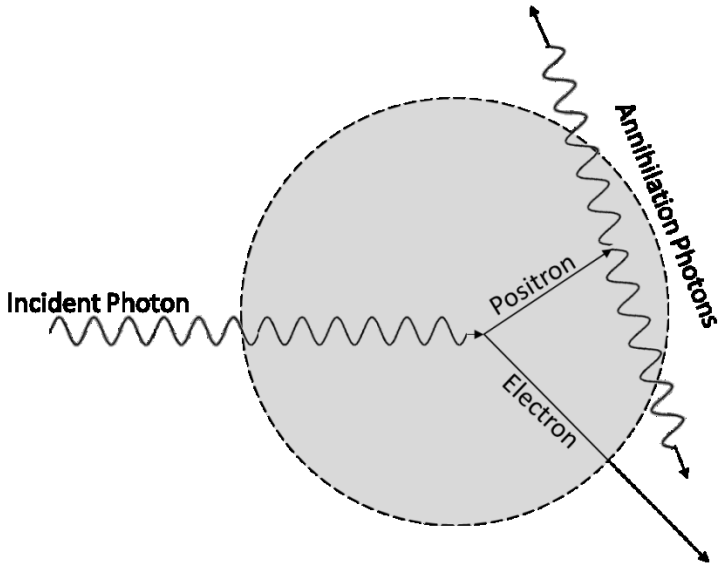

Figure 9: Depiction of a photon incident on a volume, V, shown in grey, resulting in a pair production event with annihilation photons and electron leaving the volume.

The quantity of kinetic energy released in the medium, or KERMA, is a concept which is relevant for indirectly ionizing radiations such as photons. Considering a volume *V* and an incident beam of uncharged particles which carry some radiant energy into that volume, $(R_{in})_u$, and the uncharged particles leaving *V* carrying some radiant energy out of that volume, $(R_{out})_u$, the radiant energy remaining in *V* will be the difference between these values. However, as discussed, liberated charged particles can generate uncharged radiation due to interactions of their own, and this uncharged radiation can then leave *V*, for example, as bremsstrahlung or annihilation photons (see Figure 9). This will not contribute to the energy in V, since the quantity of interest is the kinetic energy received by charged particles in *V*, regardless of how they deposit the energy [74]. To quantify the radiant energy transferred to charged particles in *V*, this fraction of uncharged radiant energy leaving *V* from radiative losses must not count, changing $(R_{out})_u$ to $(R_{out})_u^{nonr}$. Additionally, any transfer of energy to mass, or mass to energy, as seen in the case of pair production, must also be considered for the same reasons. A conversion of mass to

energy should be positively contributed to our quantity, and a conversion of energy into mass should be subtracted from our quantity. The final quantity is then the energy transferred, ϵ_{tr}, to the volume V presented as:

$$\epsilon_{tr} = (R_{in})_u - (R_{out})_u^{nonr} + \sum Q \quad (12)$$

where $\sum Q$ is the net energy derived from rest mass in V. The KERMA, K, in an infinitesimal sub-volume dv, with a mass dm, within V, is:

$$K = \frac{d\epsilon_{tr}}{dm} \quad (13)$$

This is expressed in units of energy per mass, J/kg or Gray (Gy).

The KERMA can be separated into two separate components: the collision KERMA and the radiative KERMA. These components distinguish the mechanisms by which the transferred kinetic energy is spent inside the medium. Firstly, liberated electrons dissipate their energy in ionization of the atom by collisional interaction with the orbital electrons. This fraction is the collisional KERMA, K_{col}. Secondly, charged particles can interact with the electromagnetic field of the nucleus and release radiative photons from the energy loss in slowing down. This fraction is the radiative KERMA, K_{rad}.

To develop a similar quantity that does not only focus on uncharged radiation depositing energy in a volume, but considers all types of ionizing radiation, this principle could be extended to charged radiation as well. It is not then the energy which is transferred to matter being considered, but the energy imparted to matter. The energy imparted by ionizing radiation to matter is then:

$$\epsilon = (R_{in})_u - (R_{out})_u + (R_{in})_c - (R_{out})_c + \sum Q \quad (14)$$

where $(R_{in})_u$ is the radiant energy of uncharged particles entering a volume V,

$(R_{out})_u$ is the radiant energy of all the uncharged radiation leaving V,

$(R_{in})_c$ is the radiant energy of the charged particles entering V,

$(R_{out})_c$ is the radiant energy of the charged particles leaving V,

$\sum Q$ is the net energy derived from rest mass in V.

Absorbed dose is related to energy imparted or absorbed within a volume, the same way KERMA is related to energy transferred as:

$$D = \frac{d\epsilon}{dm} \quad (15)$$

where $d\epsilon$ is the expectation value of the energy imparted in an infinitesimal volume dv with mass dm. Absorbed dose is then also measured in units of Gy.

As a broad beam of photons is incident on a medium, the KERMA, and specifically the collisional KERMA, K_{col}, is at a maximum at the surface, decreasing thereafter. Absorbed dose, which considers the energy absorbed from both charged and uncharged particles, builds up to a maximum at a depth z_{max}, after which it decreases steadily with $K_{col.}$ The superficial region before z_{max} is caused by the building up of charged particle dose contribution, which is not complete until the depth is equal to the average forward range of the electron. After this point, the absorbed dose curve enters a region of transient charged particle equilibrium (TCPE), where absorbed dose is proportional to K_{col} ($D = \beta K_{col}$, where β is the quotient of absorbed dose and collision kerma at a given point) due to photon attenuation and charged particle scatter. A depiction of the relationship of collision KERMA and absorbed dose as a function of depth in the medium is in Figure 10.

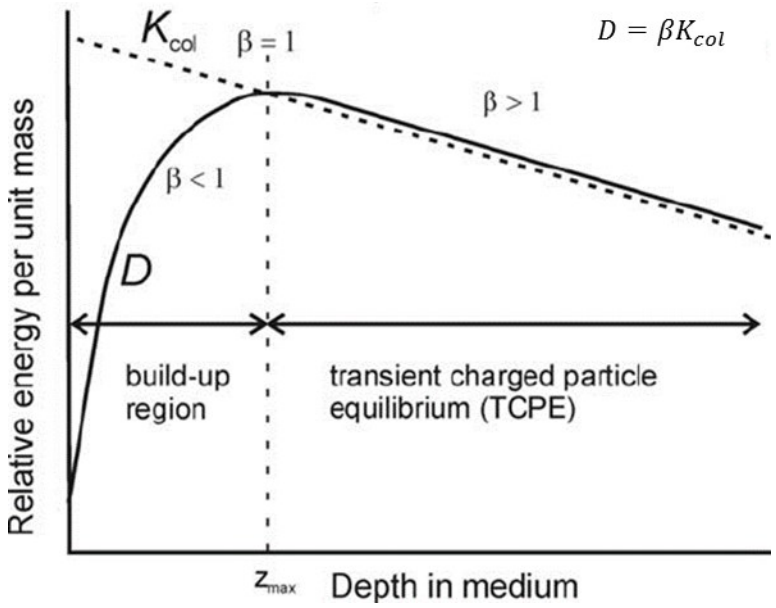

Figure 10: Collision KERMA and absorbed dose as a function of depth in a medium irradiated by a high-energy photon beam [75].

2.1.3 Computational Dose Calculation

The dose administered to a patient during treatment planning is modelled computationally by commercially available treatment planning software. Modern treatment planning systems use imaging data, advanced processing methods, dose calculation, and dose optimization methods. Electron density estimates are generated from the patient CT image data and calculation of dose deposition can be generated.

Planning systems are additionally capable of modelling the beam generation parameters of the linear accelerator to replicate fluence spectra and profiles with a high degree of accuracy. The version of Eclipse (Varian Medical Systems, Inc., Palo Alto, USA) treatment planning system used in the completion of Chapters 3 - 6 was v.11.0.31. As part of beam modelling in Eclipse, the photon beam source model was developed using Monte Carlo simulations of the components of the LINAC head. A planar phase space was used to construct specific beam parameters to match the clinical beam. The

simulated clinical beam is represented by four components: the primary photon source, which is a simulated spectrum generated by modelling the bremsstrahlung photons generated in a finite width source; the secondary photon source model, which models the photons emitted from the flattening filter and collimation; electron contamination source; and photons scattered from the hard wedge. The clinical broad beam is divided into finite-sized beamlets, β, corresponding to a divergent column of the beam with a size dependent on the grid size of the calculation volume [76].

The dose calculation algorithm used to complete the dose calculations in Chapters 3 - 6 was the Anisotropic Analytical Algorithm (AAA) for photons in Eclipse v.11.0.31. The algorithm, conceived by Ulmer and Kaissl, accounts for any tissue heterogeneity anisotropically by using photon scatter kernels in multiple lateral directions. The scatter kernels are computed in EGSnrc Monte Carlo [116] to simulate the phantom scatter effects. These polyenergetic kernels matched to the beam spectra are created by superimposing multiple monoenergetic kernels [76]. The final dose is the superposition of the dose calculated with photon and electron convolutions [76]. The volume of the patient body is divided into a 3D grid of volumetric pixels, or voxels, with a size corresponding to the calculation grid size. To align the coordinate system of the patient relative to that of the beam line, the calculation voxel grid is divergent from the source position. The calculation voxel is attributed a mean electron density from the registered locations in the patient CT images according to a calibration curve for Hounsfield unit (HU) to electron density.

In a region that is consistently homogenous, the energy distribution resulting from a beamlet β due to photons is:

$$E_{ph,\beta}(\tilde{X},\tilde{Y},\tilde{Z}) = \Phi_\beta \times I_\beta(z) \times K_\beta(x,y,z) \quad (16)$$

where $(\tilde{X},\tilde{Y},\tilde{Z})$ is the position of the calculation point relative to the origin of beamlet coordinate system, $K_\beta(x,y,z)$ is the scatter kernel defining the lateral scatter at the point (x, y, z) in the beamlet coordinate system, Φ_β is the photon fluence and is assumed to be uniform over the beamlet, $I_\beta(z)$ is the energy deposition function given as:

$$I_\beta(z) = \iint h_\beta(t,v,z)dt\,dv \quad (17)$$

where h_β is the poly-energetic pencil beam kernel derived from Monte Carlo simulation, where t and v are the spatial dimensions of the beamlet, z is the depth coordinate measured from the central beam-line. Energy is then converted to a dose with the assumption that heterogeneities can be modeled as a scaled value of water, converted via electron densities [76].

Known limitations of these dose calculation algorithms include the differences in dose in the presence of heterogeneous media caused by electron disequilibrium compared to Monte Carlo simulation [112]. In cranial plans these calculation algorithms are effective as surrounding tissues are largely homogeneous [113].

2.1.4 VMAT Optimization

VMAT optimization is a modern radiotherapy treatment planning technique and is utilized as the benchmark clinical standard in Chapters 3 - 6. As mentioned in Section 1.1, VMAT was developed in 2007 as a solution to efficiency issues in IMAT techniques for MLC leaf position change restrictions between consecutive gantry positions. The repetition of arcs over the same span were used to produce multiple unique apertures for the same arc geometry, which created an increase in treatment time. VMAT solved this

by creating a progressive resolution sampling of continuous motion delivery by evenly distributed static source positions to generate and deliver plans in a single gantry rotation. This algorithm is called PRO (progressive resolution optimizer) in Eclipse, and the version used in Chapters 3 – 6 is v.11.0.31. The MLC is initialized at discretized control points (temporal LINAC axes position instructions) as the BEV comprised of a Boolean subtraction operation of normal structures from target structures, and the dose rate is equal for all control points. Beginning with coarse sampling, iterative modifications are made to the MLC positions and MU weights of the sampled points. In the initial stages of optimization, large scale adjustments are made in leaf sequencing and dose rate. The scale of these adjustments reduces as the optimization progresses. Samples are added progressively throughout the optimization at the midpoint between existing samples until the sampling has reached its final resolution.

The amount of MUs and MLC transition motion is varied between sampled control points. These constraints control the efficiency of the delivery to ensure that the gantry rotation rate is not required to slow to accommodate large transitions in dose rate or MLC motion. These can be expressed as:

$$\Delta x \leq \Delta\theta\left(\frac{dx}{d\theta}\right)_{max} \text{ and } \Delta MU \leq \Delta\theta\left(\frac{dMU}{d\theta}\right)_{max} \quad (18)$$

where Δx is the change in MLC position between control points, ΔMU is the change in MU between control points, $\Delta\theta$ is the change in gantry angular position between control points, $\left(\frac{dx}{d\theta}\right)_{max}$ is the maximum allowable change in MLC position between degrees of gantry travel, $\left(\frac{dMU}{d\theta}\right)_{max}$ is the maximum allowable change in MU between degrees of gantry travel. A change to these axes is requested at each iteration of the optimization to one of the available fields. If a change doesn't violate the restrictions above, the dose

distribution and resultant cost function are evaluated. If the total cost is reduced, the change is accepted, otherwise it is always rejected. The optimization cost-function is based on user-defined objective dose-volume constraints for the structures in the plan. Doses are specified as function of structure volume and a relative priority for each constraint is input into the system. Cost is defined by quadratic differences weighted by the priority value assigned, and finally summed to construct the total cost function. The total objective function used in PRO in Eclipse is the sum of the dose-volume and other user-defined objectives.

2.2 MEDICAL LINEAR ACCELERATORS

2.2.1 Photon Beam Generation

A medical linear accelerator is a high precision device used to accelerate charged particles (electrons in the case of the production of photon beams) by means of microwave radiofrequencies (RF) before colliding with a high-Z material target to generate a spectrum of photons via bremsstrahlung. The major components of a LINAC consist of a gantry and stand: the gantry houses all components which act to accelerate and shape the beam, and the stand supports the gantry and houses all components to produce the RF for accelerating electrons. Other important components of the LINAC consist of a source of electrons, a source of microwave RF, an evacuated accelerating waveguide in which to accelerate electrons, a bending magnet used to direct the electron beam line, and the head of the LINAC containing the components to control the shape of the photon beam exiting the LINAC. A cross-section of the LINAC structure can be seen in Figure 11. A depiction of the collimation system and the nature with which it generates the BEV within the gantry head is shown in Figure 12. While variations on LINAC beam

generation specifics vary, the work within this thesis is conducted solely with a Varian TrueBeam STx LINAC with stereotactic radiosurgery capabilities as equipped at the Nova Scotia Health Authority (NSHA). As such, the specifics of the LINAC will be outlined as they are contained in the TrueBeam STx system.

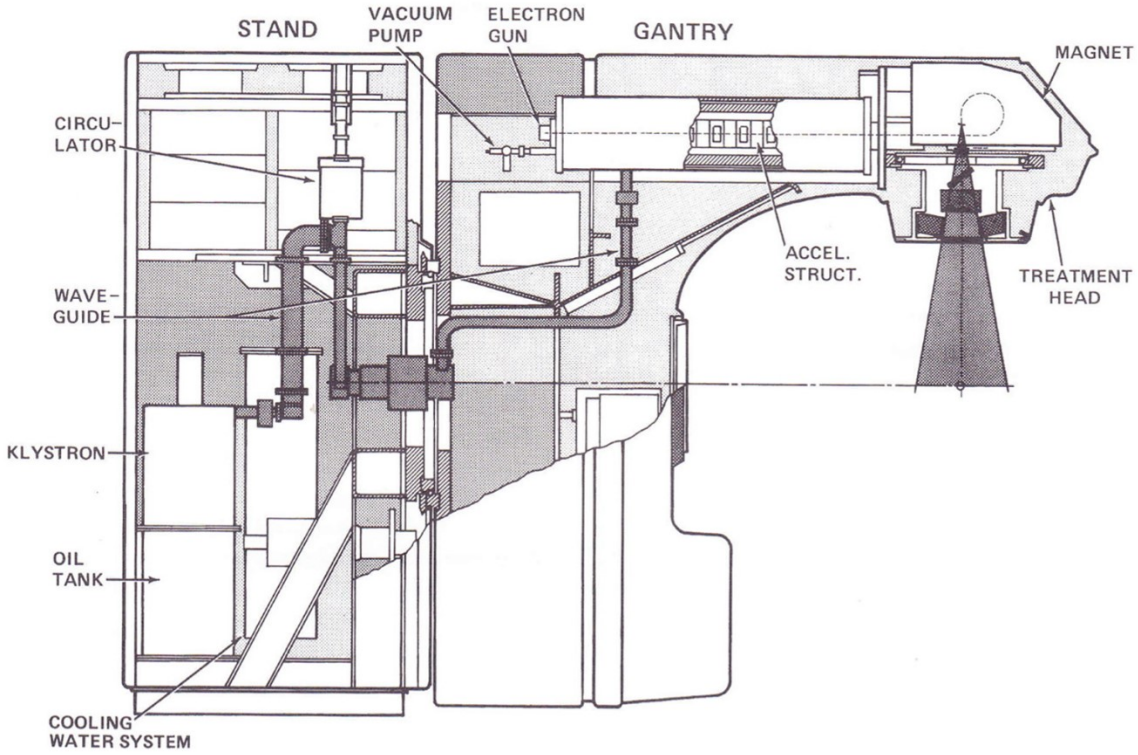

Figure 11: Cross-section schematic of a medical linear accelerator [5].

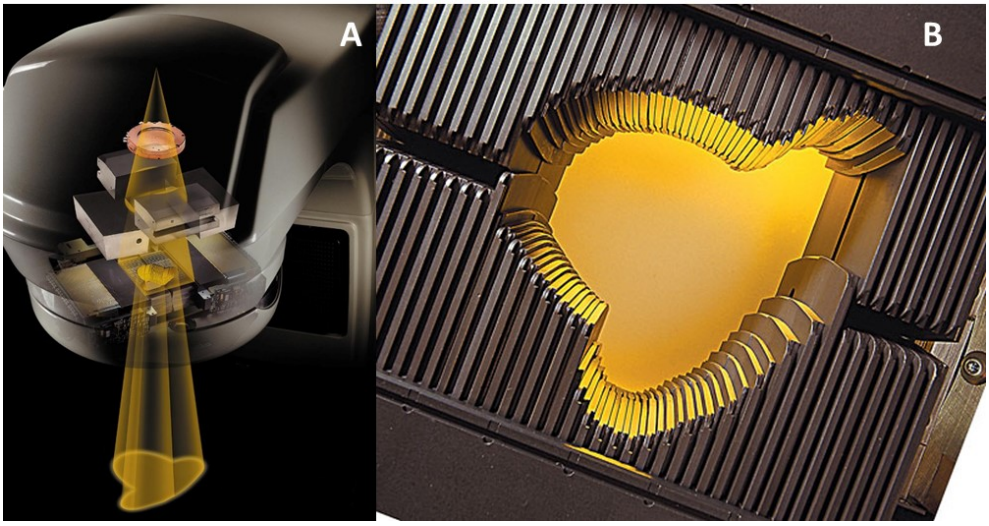

Figure 12: A) depiction of the collimation system used in a Varian TrueBeam system and the effect on the beam line. B) The MLC forming a collimation pattern as seen collimating the beam in A). Images from Varian Medical Systems, Inc [110].

The electron gun consists of a gridded electron gun (or triode) which produces electrons through thermionic emission and allows the LINAC to be capable of a continuously variable dose rate [106]. These emitted electrons are accelerated towards the waveguide, an evacuated cavity which is fed microwave RF.

The RF used to accelerate electrons is generated via klystron in modern LINACs, with other versions of medical LINACs using a magnetron. The klystron produces microwave RF at 2856 MHz and is fed into the accelerator waveguide which is divided into cylindrical cavities by disks that have circular holes through which the beam can travel. These cavities are specifically designed for the microwave frequencies to generate an accelerating electric field for bunched electrons. The beam of electrons is additionally focused throughout acceleration to narrow the total width of the beam of electrons. The beam exiting the accelerating waveguide then enters an achromatic bending magnet which steers the beam a full 270^{o} after which it enters the LINAC head.

Standard photon beams are generated through electron collisions with a high-Z target that generates a bremsstrahlung X-ray spectrum. This spectrum is initially strongly forward-peaked, motivating the addition of a flattening filter to preferentially attenuate closer to the beam axis to create a flattened beam profile. The flattening filter may be removed (FFF treatments) to produce a higher dose rate if required.

TrueBeam treatment units are capable of a number of photon energies and, with removal of the target, electron beams. The nominal photon energy used in this thesis is a 6 MV beam in both standard and FFF modes. This photon spectrum has characteristic dosimetry with a maximum dose found at a depth in water of 1.60 ± 0.15 cm for a 10 x 10 cm^2 field sized measured at a 100 cm SSD. The PDD value for the same beam conditions at 10 cm depth in water is approximately 67.2 ± 1.0 %. Standard photon dose rates range between 5 and 600 MU/min, while FFF is capable of 400 - 1400 MU/min [107].

2.2.2 Developer Mode Delivery

While conventional treatment planning systems and control systems for LINACs do not support simultaneous motion of multiple axes, Varian (Varian Medical Systems, Inc., Palo Alto, USA), the manufacturer of the LINACs and treatment planning software used in the completion of this research, does provide a non-clinical research interface which allows for the delivery of customized plans with simultaneous motions. The developer mode platform allows researchers access to advanced control features not typically accessible in clinical LINAC modes. Developer mode code can be written in Extensible Markup Language (XML), which can be locally stored on the control console system. The instructions for the LINAC are written in a control point-based system in which instructions for the axes are provided in discretized points and linearly interpolated

between. An axis which is not provided instructions at a control point is not modified from its pre-set position or trajectory between other control points. Control points are executed temporally to accommodate the slowest axis, such that all axes arrive at their instructed position in coincidence. The maximum velocity of the axes of the linear accelerator are given in Table 1.

Table 1: Maximum velocity for each of the dynamic axes available on the TrueBeam LINAC [76].

Axis	Maximum Velocity
MLC Carriage	1.20 cm/s
MLC Leaf	2.50 cm/s
Gantry Rotation	6.00 °/s
Collimator Rotation	15.00 °/s
Couch Vertical	2.00 cm/s
Couch Lateral	4.00 cm/s
Couch Longitudinal	8.00 cm/s
Couch Rotation	3.00 °/s
Collimator Jaws	2.40 cm/s

The XML files used in this thesis were programmatically generated and formatted using customized Python and MATLAB scripts.

2.3 RESEARCH METHODS

The methodology carried out in Chapters 3 - 6 was conducted using novel methods of data analysis and optimization. The outline of the most pertinent of these methods is given in this section.

2.3.1 Volumetric Projection

The perspective in the BEV of the anatomical structures is modified with the position of the source in the LINAC. As such, the ray lines diverging from the source position onto targeted structures make up the potential incident beam angles for treatment. These divergent beam angles can be visualized from the perspective of an arbitrary source position by projecting the volumetric data onto a two-dimensional plane perpendicular to that of the central ray-line of the source. To optimize treatment plans on a patient specific basis using purpose-built code, it is crucial to import the anatomical information into a computational environment to design tailored treatment plans with a high degree of accuracy. MATLAB (The MathWorks, Inc., Natick, Massachusetts, U.S.A.) is the computational environment in which the optimized treatment parameters in this thesis were designed. This anatomical information is contained in the Digital Imaging and Communications in Medicine (DICOM) format. A typical radiotherapy plan will consist of four separate types of files: RT Plan DICOM, which holds all parameters for a specific plan generated for the patient; RT Structure DICOM, which contains the patient structure set; RT Dose DICOM, which contains the dose voxel data as calculated by the treatment planning system and the metadata that applies; and DICOM files for every CT image acquired for the patient. Additional imaging modalities and metadata are

also available in DICOM format, but the four aforementioned are the ones used in this thesis.

To optimize the treatment plan, it is vital to simulate the 2D BEV of 3D anatomy from an arbitrary source position with accuracy to apply algorithmic methods to the suitability of radiation source positions relative to the patient. To acquire this anatomical information, the RT Structure DICOM is used, which contains the 3D contour information generated in the treatment planning software through manual contouring on axial CT slices by trained experts to delineate the bounds of anatomical structures. This information is imported into MATLAB using built-in DICOM import packages and filtered to only contain pertinent 3D locations of points within structures. These structures are imported with an inherent coordinate system in millimetres defined by the organization in the RT Structure DICOM. In the installation of Eclipse v.11 at NSHA, this coordinate system has the x-dimension to specify patient left-right, y-dimension to specify anterior-posterior, and z-dimension to specify superior-inferior. This coordinate system is illustrated in Figure 13 (this system differs from the axes in the IEC 61217 patient coordinate system as the y and z axes are exchanged and superior inferior direction would be reversed). Additionally, the coordinate system for these 3D points needs to be adjusted to faithfully contextualize them in terms of the geometry of the linear accelerator. As shown in Figure 13, the axes of the LINAC coincide at a fixed 3D location in the treatment room, referred to as the isocentre. To appropriately apply rotations or translations to the view of these 3D structures, the axes must rotate about this point.

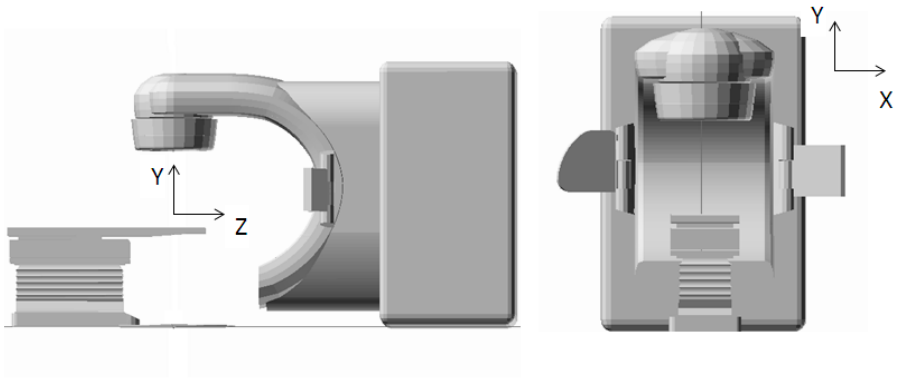

Figure 13: LINAC coordinate system used for treatment planning optimization with the software in Chapters 3 – 6.

The following rotation matrix is used to rotate by θ_c around the *y*-axis and apply couch rotations to the imported anatomical structures:

$$r_c = \begin{pmatrix} \cos\theta_c & 0 & \sin\theta_c \\ 0 & 1 & 0 \\ -\sin\theta_c & 0 & \cos\theta_c \end{pmatrix} \quad (19)$$

An anatomical point $P = [x_P, y_P, z_P]$ within a patient can be multiplied by r_c to rotate this point according to the appropriate applied couch position in the LINAC coordinate system. Rotation about the z-axis is defined later in the section as Equation 26 for gantry rotation. Rotation about the x-axis is not considered relevant.

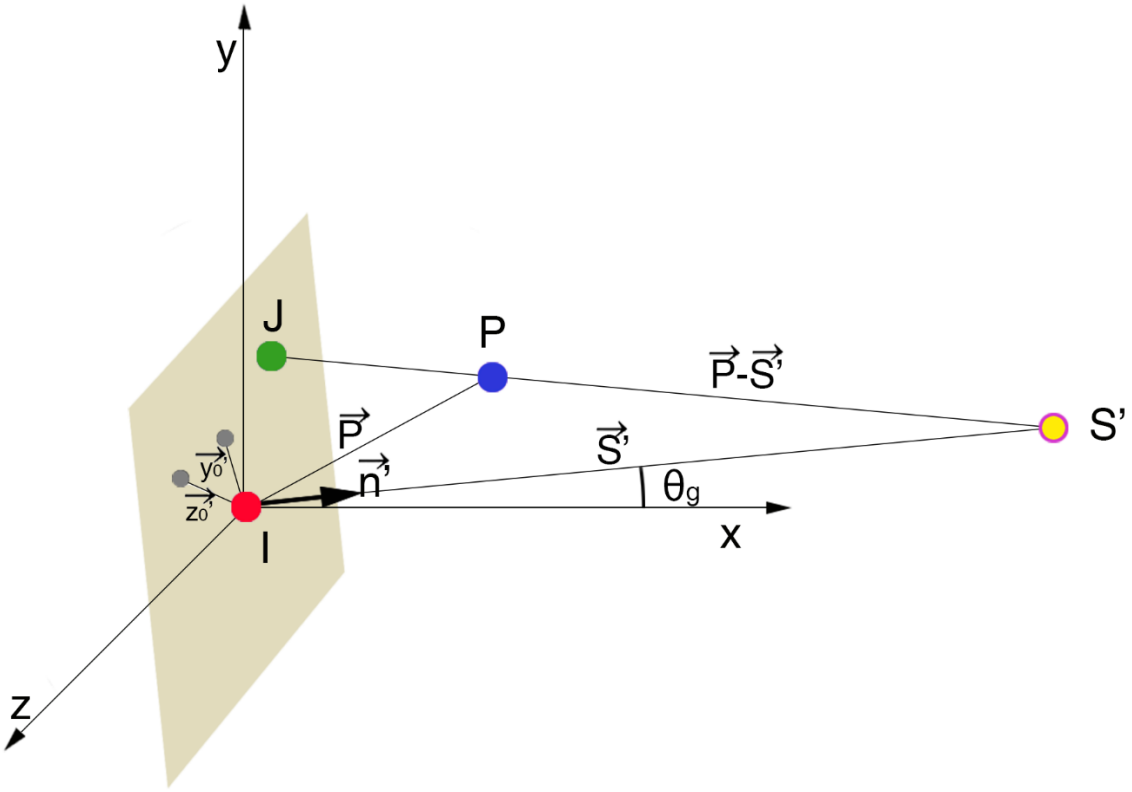

Figure 14: Depiction of the geometry for the divergent projection of a 3D point onto a 2D plane at isocentre to generate BEV.

To visualize contour points in the projected BEV (see Figure 14), they must be projected along the divergent ray line which joins the source position, *S*, and a given point, *P*, to where it intersects a plane perpendicular to the vector joining isocentre, *I*, and *S*, and containing *I*. The linear accelerator source position is located 100.0 cm from the isocentre and is initialized at a position of $S = [x_S, y_S, z_S] = [1000\ ,0\ ,0]$ in the coordinate system of the isocenter plane (additionally, for ease of calculation the coordinate system origin is at isocentre, $I = [x_I, y_I, z_I] = [0\ ,0\ ,0]$). To uniquely identify the plane at isocentre, the normal vector to the plane, $\vec{n} = [a, b, c]$, can be calculated with the general equations for a plane in Cartesian coordinates as:

$$ax + by + cz + d = 0 \qquad (20)$$

$$d = -ax_d - by_d - cz_d \quad (21)$$

where the plane intersects the point $[x_d, y_d, z_d]$. Since our plane is always intersecting *I*, or origin, the equation simply reduces to:

$$ax + by + cz = 0 \quad (22)$$

To find the normal vector $\vec{n} = [a, b, c]$ two points in the plane can be used. For the arbitrarily initialized source position in the x-direction, two points in the y-z plane can be used as:

$$y_0 = [0\ 1\ 0] \quad (23)$$

$$z_0 = [0\ 1\ 1] \quad (24)$$

The vectors leading from isocentre (origin) to these points are $\overrightarrow{y_0}$ and $\overrightarrow{z_0}$, respectively. The normal vector to the plane can be then determined by:

$$\vec{n} = \overrightarrow{y_0} \times \overrightarrow{z_0} = [a, b, c] \quad (25)$$

When the gantry position is rotated, the source position is rotated around the z-axis by:

$$r_g = \begin{pmatrix} \cos\theta_g & -\sin\theta_g & 0 \\ \sin\theta_g & \cos\theta_g & 0 \\ 0 & 0 & 1 \end{pmatrix} \quad (26)$$

A rotated source position can be determined from $S' = Sr_g$. This can be used to find the vector joining the rotated source to isocentre by $\overrightarrow{S'} = [Sr_g - I]$. Similarly, the vectors which yielded the normal vector can be rotated by r_g to give $\overrightarrow{y_0'}$ and $\overrightarrow{z_0'}$ to yield the normal vector for the rotated source position, $\overrightarrow{n'}$, as above. Any point *P* can also be represented in its vector format, $\vec{P} = [P - I]$.

For any contour point *P*, the location of the projection of the point, *J*, on the isocenter plane, defined by $\overrightarrow{n'}$, can be defined by:

$$J = [x_J, y_J, z_J] = \overrightarrow{S'} + t(\vec{P} - \overrightarrow{S'}) \quad (27)$$

Where t is given by:

$$t = \frac{\overrightarrow{n'} \cdot \overrightarrow{S'}}{\overrightarrow{n'} \cdot (\vec{P} - \overrightarrow{S'})} \quad (28)$$

Applied to all points in a 3D structure, the 2D projection as viewed from source position onto a plane at isocentre can be calculated as above. Plotting all relevant structures can produce the 2D projection information for BEV optimization.

2.3.2 Metrics for Optimization

2.3.2.1 BEV Overlap

To quantify the presence and level of overlap between structures in a BEV, the 3D contour information for every structure pertinent to the radiotherapy plan was imported and projected onto the appropriate isocentric plane as described in Section 2.3.1. The result is the 2D projection of this structure as it is viewed by the source. If the boundary of the projection of the targeted structures physically intersects with the area of the OARs in the BEV, this presents the undesirable scenario of shared irradiation of these structures. This can be identified by the conversion of the 2D points for each structure into a contiguous binary mask by way of the MATLAB function *poly2mask.* The boundary of the binary mask is set to the boundary of all projection information from all structures in that particular BEV. A binary mask is generated which is given a value of 1 inside the structure area and 0 outside of the structure area. The overlap between two structures can then be determined by taking the Boolean AND of the binary masks (see Figure 15).

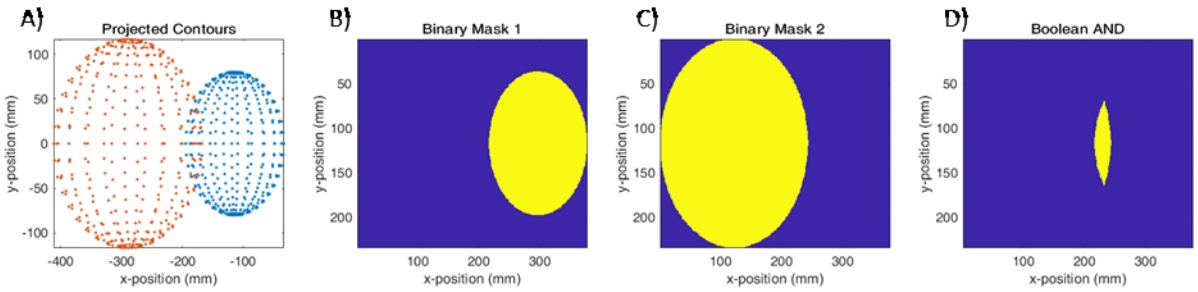

Figure 15: The calculation of overlap given the 2D projection information for contours from RT structures DICOM. (A) Examples of contour projections for two structures from an arbitrary source position. (B) The contour information from the first structure converted to a binary mask with resolution of 1 mm^2. (C) The contour information from the second structure converted to a binary mask with resolution of 1 mm^2 (D) The Boolean AND of B & C, i.e. the overlap region of the binary mask 1 and 2.

The overlap at any incident beam angle is quantified based on a metric described by Yang *et al.* in 2011 that normalizes the calculated overlap of a structure (target or OAR) relative to its total projected area. While the pixels measured in our projected areas are 1 mm^2, Yang's overlap metric creates a unitless value for overlap that is relative to initial sizes of projected structures. This metric at a couch coordinate c and gantry coordinate g is defined as:

$$E(c,g) = \frac{L_i(c,g)}{A_t(c,g)} \times \frac{L_i(c,g)}{A_i(c,g)} \qquad (29)$$

where $L_i(c,g)$ is the area of overlap measured for the i^{th} OAR, $A_t(c,g)$ is the area of the target volume, and $A_i(c,g)$ is the area of the i^{th} OAR. This yields a normalized product of the fraction of overlapping area. All area calculations are measured from the projection of the target volume and the i^{th} OAR onto a plane at isocentre, as viewed form the source position. An example of Equation 29 catalogued at every position of couch and gantry for an OAR and target is shown in Figure 16.

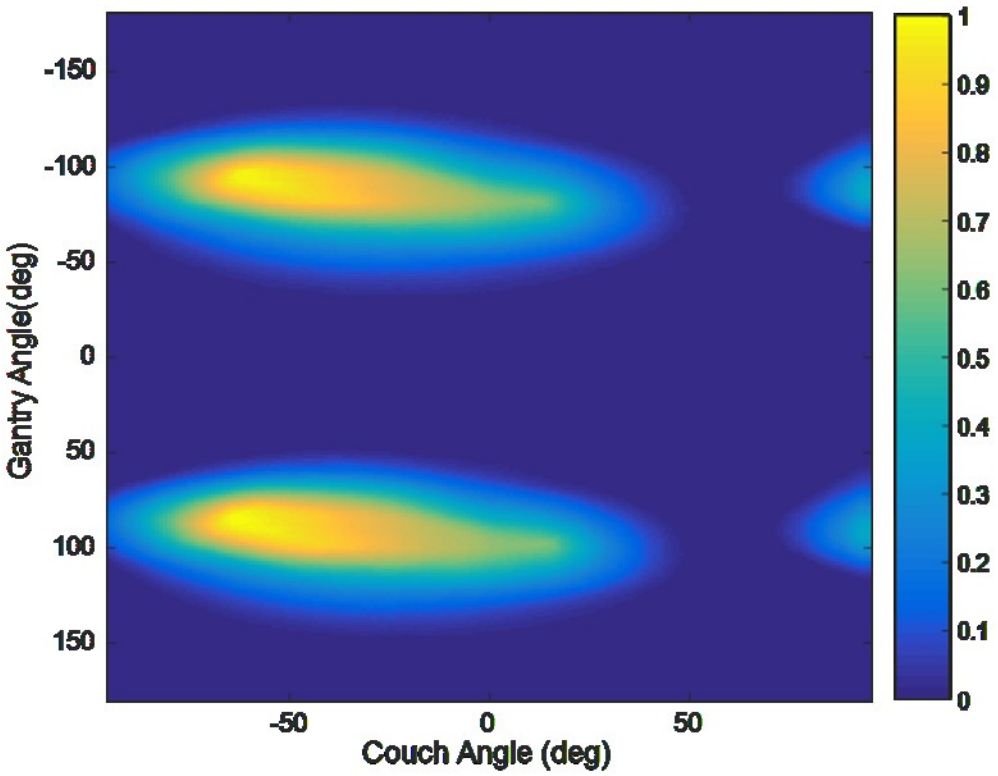

Figure 16: A BEV overlap map computed for every coordinate of couch and gantry, shown here in IEC 1217 [87] coordinates, as calculated by Equation 29 for a brainstem and an acoustic neuroma tumor. The color scale here indicates high values of overlap in the bright regions, and low overlap in the dark.

2.3.2.2 Whitespace Calculation

To investigate collimator optimization, research was conducted to develop an algorithmic approach to quantify collimator angle suitability through minimization of irradiation of normal tissue based on conformal aperture design. To fulfil this requirement, a metric has been developed, referred to herein as whitespace, to unambiguously propose a solution based on any input anatomical geometry. Whitespace is introduced as the principle feature of the methodology in Chapter 4 and analyzes the projection data of structures as outlined in Section 2.3.1. By modelling the collimation system geometry and subtracting all areas occupied by desired assignments, the

remainder is identified as uncollimated non-target anatomy (or Whitespace) that is undesirable for inclusion in the treatment field. This equation can be expressed as:

$$W(\theta_{GA}, \theta_{CH}, \theta_{CL}) = w_1 A_{jaw} - w_2 A_{PTV} + w_3 (A_{PTV} \cap A_{OAR}) + w_4 A_{MLC} \quad (30)$$

where W is the whitespace, θ_{GA} is the gantry rotation angle, θ_{CH} is the couch rotation angle, θ_{CL} is the collimator rotation angle, A_{jaw} is the total rectangular area encompassed by the jaw system, A_{PTV} is the area of the target, $A_{PTV} \cap A_{OAR}$ is the area of the OARs overlapping with the targets in the BEV, A_{MLC} is the area collimated by the MLC when conformally fit to the target, and w_{1-4} are weighting factors which can adjust the priority or inclusion of any of the terms in the equation. Specific applications of these factors include w_1 being used in some instances to highlight the area of the BEV not collimated by the jaw, and thus contributing to interleaf transmission to normal tissues, or $w_3 = 0$, to remove the inclusion of OAR overlap from the equation. The weighting of these values is not investigated in this work, but may be beneficial in some instances. All areas are calculated in the isocentric plane.

This calculation is implemented programmatically by rotating the projected BEV according to the collimator angle and sampling the BEV at a given leaf pair. The contour information found within the sampled leaf pair is then condensed to a 1D binary profile (presence of contour or not). This profile is then measured for whitespace present if the leaf pair were set to a conformal setting. The summation over all leaf pairs is the total whitespace, *W*, found for this BEV at this collimator angle, θ_{CL}. This sampling is conducted at a 0.1 mm resolution in the direction of leaf travel, matching the resolution of leaf fitting in Eclipse v.11. This technique is utilized in the methodologies of Chapters 4 - 6.

2.3.3 Trajectory Navigation Techniques

The methods described in Section 2.3.1 and 2.3.2 are used in of the methodologies of Chapters 3 - 6 to create 2D cost function maps. These maps present the cataloguing of suitability measures, and, when appropriately organized, can be navigated to create LINAC axes trajectories for radiotherapy plans. Multiple algorithms for the creation of trajectories have been produced from this research group for both dynamic and fixed trajectory navigation, and these are summarized in the following sub-sections.

2.3.3.1 Best Single Fixed Sub-Arc Trajectory

The best single fixed sub-arc trajectory identifies the optimal trajectory for a given map when the output trajectory involves no dynamic motion within an arc. In a map with the aforementioned convention, this corresponds to trajectories with one allowed column (couch angle) for a span of rows (gantry angles). This amounts to identifying for a span of rows in the map, beginning with i and ending with j, the column with a minimum accrued cost between i and j. The graph theory restrictions to the trajectory can be represented as:

$$S = min\ c_{ij} \tag{31}$$

$$(i,j) \in Z;\ \ i < j \tag{32}$$

Where S is the total trajectory score, c_{ij} is a column spanning rows i to j. This is implemented programmatically by summing the cost from all valid columns from rows i to j and returning the index of the column with the minimum cost. Chapter 3 employs this technique for optimizing the standard cranial radiosurgery VMAT template, the details of

which are expanded upon in that chapter. A trajectory designed by this method is shown in Figure 17A.

2.3.3.2 Optimal Fixed Sub-Arc Trajectory

Optimal fixed sub-arc trajectory extends the best single fixed arc trajectory to identifying the optimal length of continuous best fixed arcs to traverse a map. Given a defined number of total arcs allowed in the trajectory, n, and a minimum allowable total span of rows in an arc, m, the algorithm finds the best way to distribute the start and stop value of each arc, i and j, respectively, such that the span of all arcs create a continuous piece-wise function from the first row of the map, to the last. The graph theory restrictions to the trajectory can be represented as:

$$S = min \sum_{(i,j)\in E} c_{ij} x_{ij} \quad (33)$$

$$(j - i) \geq m \quad (34)$$

$$\sum_{(i,j)\in E} x_{ij} \leq n \quad (35)$$

$$i < j \quad (36)$$

where x is a binary variable where 1 means the arc is included in the final solution and 0 if it is not. Integrating over any range of rows i to j, the first column to return the minimum total integrated value is superior (or equivalent in the case of multiple minima) to all other columns. If one collects the minimum column for every valid span i to j, the optimal navigation of the map becomes simply examining all combinatorics of complimentary sets of arcs generating perfect piece-wise functions through minimum columns. This set of arcs for all valid spans is referred to in Chapter 6 as the convex set. A constrained Bellman-Ford algorithm, a dynamic programming method, is used to

examine the optimal combinatorics of the convex set and return the optimal arcs to generate a solution to the traversal of a map.

Chapter 6 employs this method to planes of 3D cost space to generate candidate arcs from which a final trajectory is chosen. This method is expanded upon greatly in the methodology therein. A trajectory designed by this method is shown in Figure 17B.

2.3.3.3 Dynamic Trajectory

The algorithm designed for the dynamic (motion permitted simultaneously on couch and gantry) traversal of a map functions through a four-step process to generate a trajectory.

1. Trajectory built from absolute minimum angles.

   For each row of the map, the trajectory takes the corresponding column in which the value is at a minimum. Written in graph theory notation is:

$$S = min \sum_{(i,j)\in E} c_{ij} x_{ij} \quad (37)$$

$$(j - i) = 1 \quad (38)$$

2. Filter trajectory for spans of couch stability.

   Filter the values found in step 1 to remove those which require motion more than the user-defined mechanical restriction. If the difference in value between the current minimum column being analyzed, $min\ c_i$, and the neighbouring row's minimum column, $min\ c_{i+j}$, is greater than the restriction applied, the couch coordinate $min\ c_i$ is removed from the trajectory.

3. Repair trajectory using linear interpolation.

Over all rows where the absolute minimum column has been removed from the trajectory, link the nearest preceding coordinate in the trajectory with the nearest proceeding coordinate using linear interpolation.

4. Refine interpolated trajectory.

   At this step, the linear interpolation from the previous step is used as a starting point for further refinement. At all rows where the column in the trajectory was determined via linear interpolation in step 3, investigate neighbouring columns within an allowed maximum distance from the preceding point in the trajectory for lower cost. If the score at any allowable neighbouring column is lower than the current column in the trajectory, replace it. Repeat until all interpolated trajectory points have no allowable neighbours with lower scores.

While this dynamic algorithm is not employed in the work within this thesis, it was the trajectory method used to generate trajectories in the first paper by our research group [60] and offers specific advantages (primarily the customizable parameters for trajectory smoothness) over traditionally optimal trajectory methods. Modification of the parameters of the trajectory algorithm allow the user customization over the level of optimal path versus the rate and extent of couch motion. A trajectory designed by this method is shown in Figure 17C.

2.3.3.4 Bi-Direction Gradient Trajectory

Chapter 4 describes the optimization of the rotation angle of the MLC system of the LINAC using the BEV metric methodology described in Section 2.3.2.2. The values of this metric were catalogued to build 2D cost function maps in which trajectories

traversing the map generate solutions for the rotation of the collimator (columns) with every control point (rows) of the treatment plan. This can be conducted in four steps:

1. Beginning at the first row and the first column, define a trajectory by moving to the next row, and choosing the column which corresponds to the lowest value of cost, within an allowable range of columns from the current column position. When the final control point has been reached, sum the values of cost from all coordinates in the trajectory.
2. Repeat step 1, for each column in the first row.
3. Repeat steps 1 and 2 with the map flipped vertically. This creates gradient trajectories built starting from the last row and working towards the first.
4. Find the trajectory defined from steps 1 - 3 with the minimum accrued total whitespace score.

A trajectory designed by this method is shown in Figure 17D.

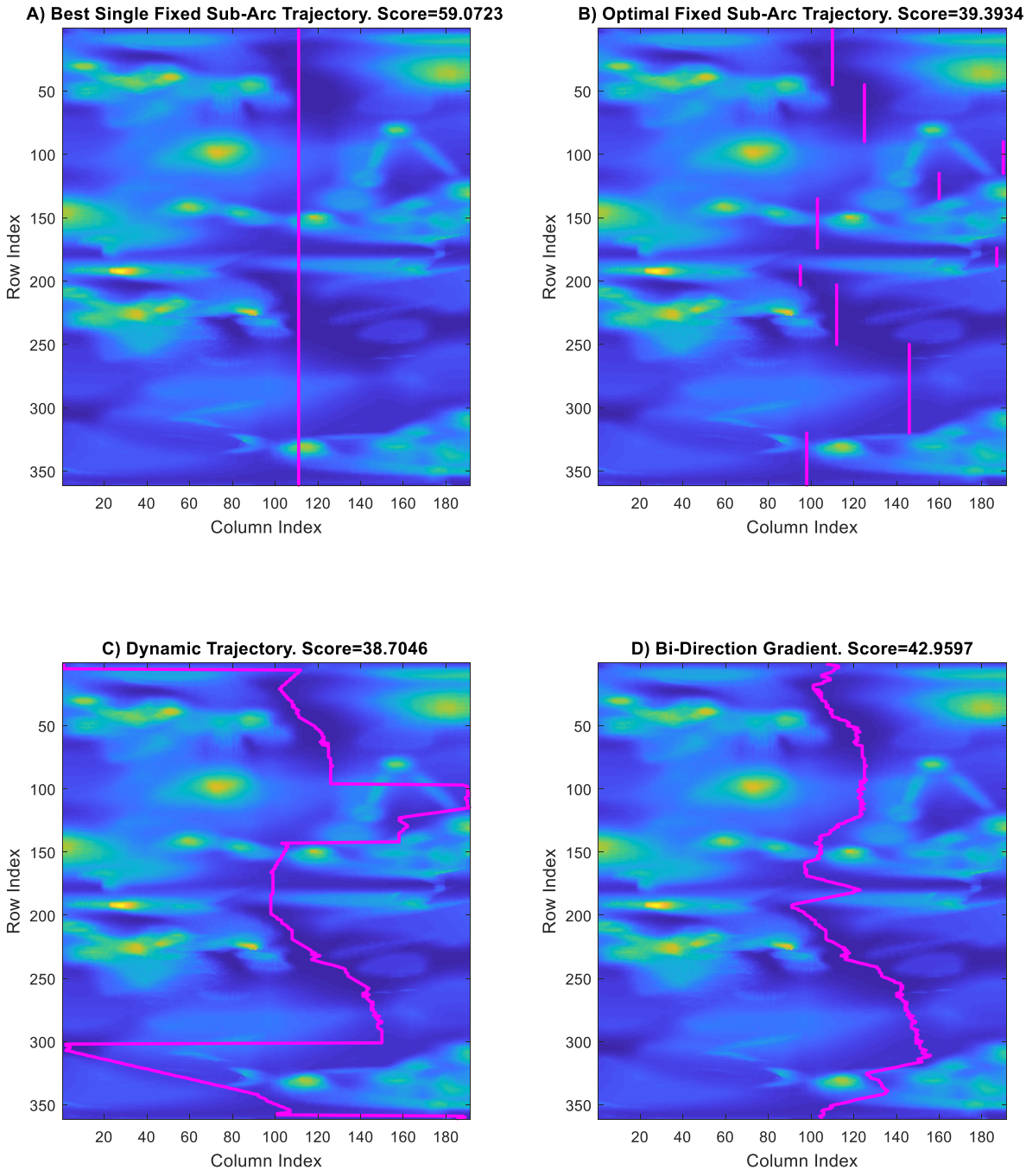

Figure 17: A depiction of the four methods of trajectory optimization described in Section 2.3.3 on the same cost map. The total cost of each trajectory through the map is shown in the title as score. A) The best single fixed sub-arc for the traversal of the map shown in magenta. B) The optimal fixed sub-arc trajectory shown in magenta. Here the restrictions are set such that the arcs can be no shorter than 10 rows of travel, and the solution must contain 10 total arcs. C) Dynamic trajectory designed in magenta. The restrictions are set such that the filter examines the trajectory with a row width of 2, a column with of 2, and a neighbour search of 5. D) Bi-direction gradient trajectory shown in magenta. Here the maximum restriction on column distance between rows is set at 3.

2.3.4 Dose Matrix Analysis

In Chapter 5, the dose contribution for every control point is optimized via an objective function that uses as input the dose distribution for a given plan. To quantify important metrics of a dose distribution, dosimetric information was extracted from RT Dose DICOM files that were calculated in Eclipse for every control point independently. These matrices contain the information about how dose is distributed from each control point. The pertinent data in this matrix are voxels located within the 3D boundary defined by structure contours. Using the dose matrix for every control point and the contour information for every structure, the matrices are filtered for the voxels within the structure boundary and the associated dose for those voxels. Each dose value in a voxel is divided by the number of monitor units used to deliver the dose within each matrix to normalize the dose information. These voxel values are catalogued according to the structure and control point information. This creates a data structure in which all dose information for a given control point within a given structure can be easily accessed and modified without the need to open the cumbersome dose matrix. Additionally, this provides a simple means of rescaling and combining potential monitor unit distributions, without the need of adding all dose matrices.

Programmatically, this is conducted by examining each slice of the RT Dose matrix independently and overlaying the corresponding contour information from the RT Structure DICOM. By creating a binary mask using the *poly2mask* MATLAB function that matches the size and resolution of the dose matrix slice, with values of 1 within the boundary of the contour and values of 0 outside, the element-wise multiplication of the

dose slice with the binary mask yields only dose voxels inside of a given structure (see Figure 18 for an example slice).

This method is employed in the dose optimizer in Chapter 5 to make it computationally feasible to iteratively examine and modify monitor unit distributions (MUD) over all control points in a treatment plan.

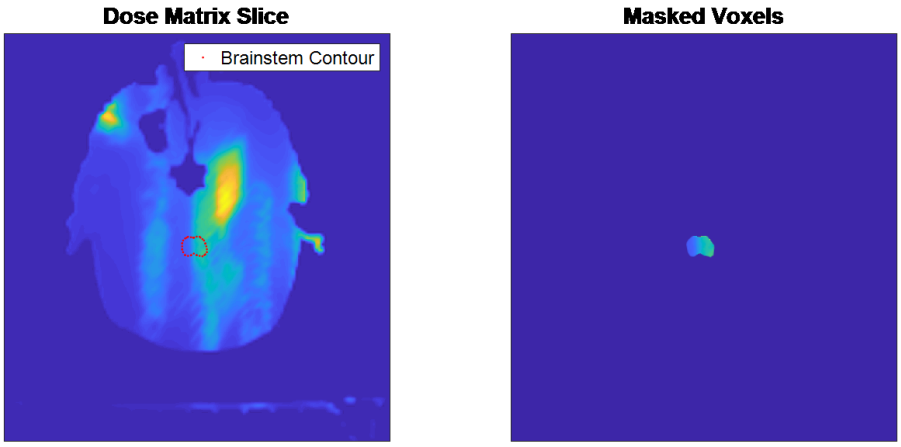

Figure 18: A visualization of the process of masking dose voxels from a single slice of the dose matrix from the corresponding contour of the brainstem.

2.3.5 Simulated Annealing

To solve the problem of an optimal distribution of parameters across all treatment control points, a simulated annealing [114] (SA) method has been employed that examines possible solutions and converges onto a minimization of a total objective function. As input, the SA algorithm takes an initial randomly generated solution and the resultant objective function value. It then selects a random control point whose parameter in the distribution is then modified by a random perturbation, within an allowable window. The perturbation to the distribution has two possible outcomes: the perturbation improves the objective function score, in which case it is accepted as the new distribution, or the

perturbation makes the objective function score worse, in which case there is an assigned probability of accepting this worsened distribution in the search for a global minimum. The probability of accepting a worsened distribution is dependent on a user-defined exponential function designed to mirror temperature's role in the strengthening of steel during the process of annealing. The probability function is:

$$P = e^{\frac{OF_{old} - OF_{new}}{T}} \quad (39)$$

where P is the probability between 0 and 1 of accepting the perturbation to the distribution, OF_{new} is the objective function value after the perturbation, OF_{old} is the objective function value before the perturbation, and T is the temperature at the current iteration. At each iteration, the temperature is decreased by a multiplicative constant denoted as the cooling rate. As such, the probability of accepting a worsened distribution is decreased as the simulation progresses. The process allows for the optimizer a higher probability of locating a global solution to the process. In Chapter 5, this method was applied to finding a MUD and the scheduling and quota of total blinks within an iABC plan. With each simulation, the cooling rate for the system which modifies T with each perturbation was 3%, and the simulations were run for 3000 iterations to ensure convergence of the objective function based on initial validations to converge on plans superior to gradient and random perturbation methods.

CHAPTER 3 MANUSCRIPT 1: OVERLAP GUIDED FIXED PATIENT SUPPORT POSITIONING OPTIMIZATION FOR CRANIAL SRT

3.1 PROLOGUE

The following manuscript is the second manuscript based on couch rotation angle optimization in cranial stereotactic planning by this research group. It is a direct application of methodologies described in Sections 2.3.1, 2.3.2.1, and 2.3.3.1. Unlike the first manuscript, it is a focused study on one specific indication of a challenging nature with an OAR proximal to the PTV. Further, it expands on the cost equation and incorporates both novel and refined methods of measuring the suitability of incident beam directions. The USF and depth comparison terms in the cost equation are highlighted in the methodology section.

Additionally, this manuscript aims for clinical practicality. Unlike the first manuscript by this group, high-resolution trajectories with a large degree of couch motion are not designed. Instead, the methods aim to optimize the clinically delivered VMAT template with couch angles repositioned on a patient-specific basis. The optimized treatments are compared with state-of-the-art expert-planned VMAT. Important discussions to optimized arc proximity are investigated, along with the trade-off nature of organ specific focus in optimization.

Publication: *MacDonald R. Lee, Robar James L., and Thomas Christopher G. "Overlap guided Fixed patient Support Positioning Optimization for Cranial SRT." Medical Physics 44, no. 1 (November 21, 2016): 17–27. https://doi.org/10.1002/mp.12008.*
The included chapter differs only from the publication in the addition of revisions for additional clarity.

3.2 ABSTRACT

Purpose: To investigate potential dosimetric improvements through the optimization of fixed-couch rotational position in cranial cancer stereotactic treatments.

Methods: Using previously delivered cranial stereotactic radiotherapy plans treated at the Nova Scotia Health Authority (NSHA), we have redesigned the treatment arrangement to find the optimal couch rotation positions based on the reduction of overlap between organs-at-risk of exposure (OARs) and target volume (PTV). Maintaining the gantry arrangements from the delivered treatment, the couch positions were determined based on a cost function analysis of accumulation of overlap score from an equation developed by Yang *et al.* [47] and refined by MacDonald *et al.* [60]. The algorithm incorporates factors for radiation dose sensitivities of each OAR, depth of both OARs and target (PTV) volumes, and orthogonality of the 3D vector between OAR and PTV in the case of proximal OAR position.

Results: The plan evaluation was conducted on sixteen acoustic neuroma patients treated with stereotactic radiotherapy plans at the NSHA. Maximum and mean doses to the OARs were reduced by approximately 14.30% ± 2.86% and 19.25% ± 2.10%, respectively, with application of this optimization technique as compared to the delivered treatment plans. In addition, PTV conformity and homogeneity were improved with application of this optimization technique.

Conclusion: This variation of the existing delivery techniques with guidance from a PTV-OAR overlap cost-function analysis technique can yield significant dosimetric improvements with no increase to delivery or planning time.

3.3 INTRODUCTION

Cranial cancer treatment plans can be complex and intricate cases to treat with radiation. The location and the size of the target volume can vary significantly within the cranial cavity, creating significant variations between cases [86]. In addition, there are many critical organs surrounding the target, which are very sensitive to exposure to radiation. Technology designed to diminish the risk of exposure to sensitive healthy volumes surrounding the target is a high priority in all radiotherapy modalities. This work aims to further refine cranial stereotactic radiation therapy techniques by modifying the current conventional template for points of entry of radiation to the cranium in order to reduce dose to sensitive structures.

The current convention for planning of a cranial stereotactic radiotherapy/radiosurgery (SRT/SRS) treatment is a fixed-couch approach, which means that for each individual gantry arc, the patient treatment couch is in a unique position. This differs from previous publications from this group [60] which featured dynamic repositioning of couch rotation concurrent with the rotation of the gantry. The extension of this technology to a fixed-couch technique is intended to display the strength of overlap metrics as a reference in the definition of radiotherapy trajectories in current practice in radiosurgery. A radiotherapy trajectory is defined as the coordinated motion of all moving components of the radiation delivery system throughout an arc. In our study, we are focused on gantry rotation and a fixed-couch rotational position. At the Nova Scotia Health Authority (NSHA), cranial SRT/SRS trajectories are based on a template, with small modifications, developed by the University of Alabama at Birmingham (UAB) [45]. Four arcs are used in a plan, and for each of these arcs, the couch is positioned 45°

apart, with one arc at the 0º position (IEC 1217 coordinate system [87]) (see Table 3). These arc lengths and couch positions are applied to all patients, regardless of PTV size and location, although some plans with highly lateral PTVs are reduced to three arcs (removing a lateral arc from the template). The trajectories defined in the template receive no modification as a result of any organ-at-risk (OAR) proximity or possibility of increased dose to the OARs. OAR sparing is achieved through volumetric arc therapy (VMAT) optimization and the definition of the objectives for each OAR.

This research aims to guide the definition of the fixed-couch rotation angles for each arc based on the quantity of overlap present in the BEV of the arc from the OAR-PTV geometric overlap score (GOS) map. This approach modifies the quantity of overlap between the OARs and PTV present in the trajectory and thus diminishes the probability of normal tissue toxicities in the treatment plan. This can be seen as complementary to the VMAT optimization.

3.4 METHODS

3.4.1 Measurement of Overlap

The position of the gantry and the patient couch alters the constituents of the radiation beam's-eye-view (BEV) and the arrangement of the anatomy with respect to it; consequently, each unique BEV will correspond to different values of area of overlap for each OAR and PTV. The calculation method for each of these areas is identical to that covered in a previous publication [60] by this group. These areas are based on the projections of the PTV and OARs onto a plane as defined at the isocentre.

The ranking of every gantry and patient support combination was conducted via a method proposed by Yang *et al.* [47], which evaluates the amount of geometric overlap

between the PTV and every OAR and classifies a large amount of overlap as a high ranking. Using the nomenclature established by Yang *et al.* [47], this overlap, *E(c,g),* was evaluated for each gantry (g) and patient support rotational angle (c), where w_i is a relative weighting factor for the i^{th} OAR, $L_i(c, g)$ is the overlap area between the PTV and the i^{th} OAR, $A_i(c,g)$ is the area of the i^{th} OAR , and $A_t(c,g)$ is the area of the PTV:

$$E(c,g) = \sum_i \left(w_i \times F(d_i, d_t)_{c,g} \times \left[\frac{L_i(c,g)}{A_t(c,g)} \times \frac{L_i(c,g)}{A_i(c,g)} \right] + USF(\propto) \right) \quad (40)$$

The normalization to the projection area of the PTV and OAR compensates for variations in sizes of these volumes. The factors w_i, $F(d_i,d_t)$, and $USF(\propto)$ are discussed and defined in the following sections.

Once an overlap measurement is calculated, this information is filed in a couch-gantry (CG) space, where gantry angle (θ_G) is along the ordinate and couch angle (θ_C) is along the abscissa. This is defined as the geometric overlap space (GOS) [47]. The amplitudes of the values are indicated via colour map, as in the example shown in Figure 21.

3.4.2 Relative OAR Dose Weighting

As previously mentioned [60], we have defined the weighting factor w_i as relating the importance of these OARs relative to one another based on dose constraints given by Quantitative Analysis of Normal Tissue Effects in the Clinic (QUANTEC) [83] and Hall *et al.* [15]. If the constraining value found in Hall *et al.* was more conservative than that found in QUANTEC, the value from Hall *et al.* was used. The radiation dose limitations, D_{tol}, to these organs given by QUANTEC and Hall *et al.* are listed in Table 2. We define

w_i as $\frac{1}{D_{tol_i}}$, where D_{tol_i} is the tolerance limit in Gy for the i^{th} OAR. This would result in units of Gy^{-1} for *E(c,g)*, which we chose to ignore in the final construction of GOS.

Table 2: Dose limitations for the most common OARs in cranial cancer cases as previously published by this group [60].

OAR	Constraint (Gy)	Limit Definition	Risk if Exceeded	Reference
Brainstem	54	Max dose (< 5% Rate)	Cranial Neuropathy or Necrosis	QUANTEC [4]
Chiasm	55	Max dose (< 3 % Rate)	Optic Neuropathy	QUANTEC [4]
Lens	10	Max dose (TD 5/5)	Cataract	Hall *et al.* [5]
Eye	45	Max dose (TD 5/5)	Blindness	Hall *et al.* [5]
Optic Nerve	55	Max dose (< 3 % Rate)	Optic Neuropathy	QUANTEC [4]
Optic Tract	55	Max dose (< 3 % Rate)	Optic Neuropathy	QUANTEC [4]
Normal Brain	45	Max dose (TD 5/5)	Infarction, necrosis	Hall *et al.* [5]
Cochlea	45	Mean dose (< 30 % Rate)	Hearing Loss	QUANTEC [4]
Pituitary	45	Max dose (TD 5/5)	Hypopituitarism	Hall *et al.* [5]

3.4.3 Factor for Percent Depth Dose Ratio

When the target volume and the sensitive organ overlap, there are two distinct possible scenarios: the first that the OAR is between the source of radiation and the PTV, and the second that the PTV is between the source of radiation and the OAR. These scenarios pose different risks to the OAR and thus need to be weighted differently. In the first case, the radiation has to first traverse the OAR in order to reach the PTV, meaning more exposure to this OAR. This is a "foreground" overlap because the OAR is in the foreground. A "background" overlap still poses a risk for the OAR, however since it is found at a greater depth than the PTV, the radiation does not expose it to the same degree. We defined *F* as an additional factor to the Yang calculation equation, which provides further insight to the special conditions of the patient anatomical arrangement and is based on the relative depth in the patient of each OAR and PTV. By taking the PDD (6 MV, field size of 10 x 10 cm^2 and 100 cm SSD) value of each object (PTV depth, d_t, and OAR depth, d_i), and calculating the ratio of these, we have a relative

measure of the decrease/increase in risk for background/foreground overlap scenarios (See Figures 19 and 20, and Equation 41 for sample calculations). The variation of the ratio of the PDDs as a function of field size is small and only becomes appreciable at larger depth differences between the PTV and OAR, thus field size dependency of PDD is ignored for this simple calculation.

PDDs were chosen as opposed to tissue phantom ratios (TPRs), because for any BEV, the PTV and OAR in question are along the same ray line and have the same SSD. In the case of TPRs, the SSD varies with depth of the object in question. Since we are interested in a relative difference in depths between PTV and OAR, a first approximation using PDDs was deemed appropriate.

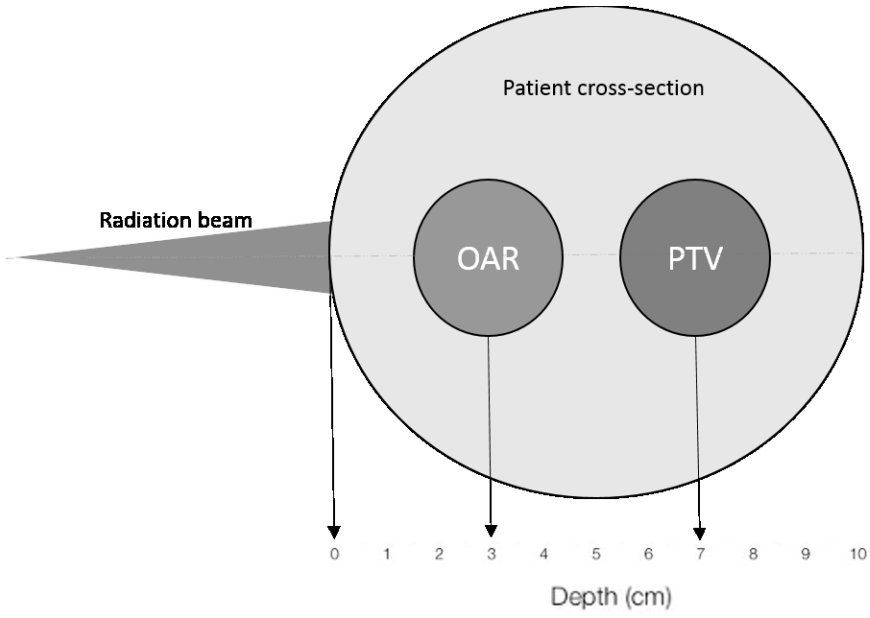

Figure 19: Schematic of the scenario of the locations of the PTV and OAR with reference to the depth within the patient, and a depiction of the divergent radiation beam. The situation depicted in this figure is a "foreground" overlap.

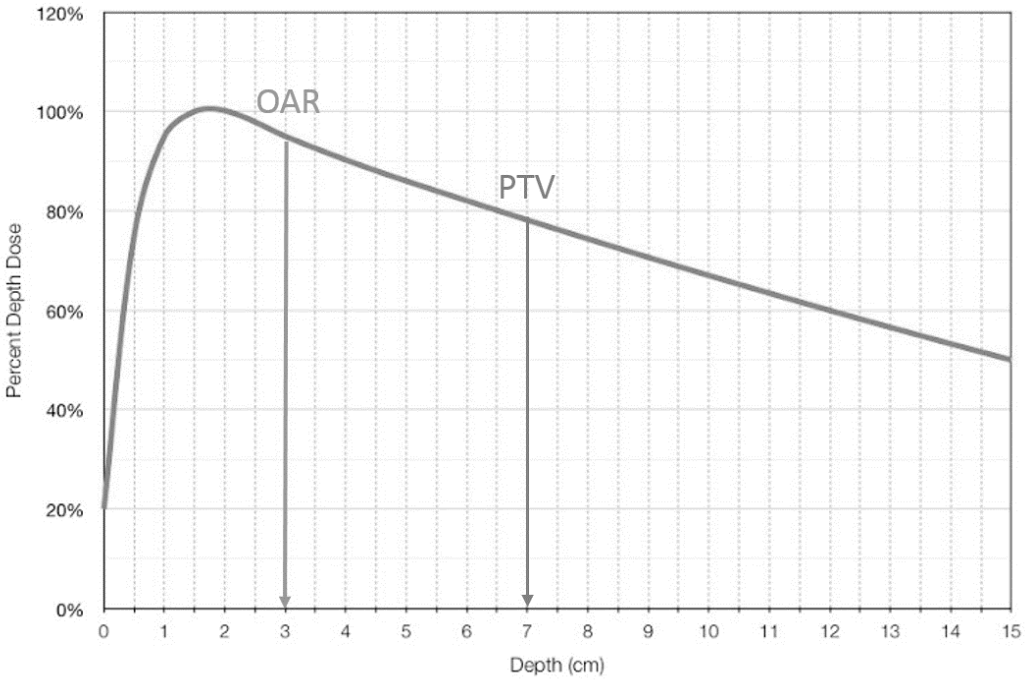

Figure 20: Plot of the PDD in the scenario from Figure 19 and the locations on the PDD curves of the depths of the OAR and PTV. This is a PDD curve for a 6MV beam, field size 10x10 cm^2, and SSD = 100 cm.

$$F(d_i, d_t) = \frac{PDD_i}{PDD_t} = \frac{PDD(3\ cm)}{PDD(7\ cm)} = \frac{95\%}{79\%} = 1.19 \quad (41)$$

By incorporating this new factor, the overlap maps for each individual OAR can be significantly modified to appropriately weight each scenario according to the risk associated with an OAR being in the foreground or background. This factor was previously [60] set as 0.10 for a background overlap, which was arbitrarily chosen and exaggerated the cost of these opposing scenarios. Although this weighting based on 6 MV PDDs may restrict the degree of freedom of the possible valid trajectories, the inclusion of this information results in more appropriate weighting and creates a much clearer context for the relative contributions to cost. The difference in GOS maps due to the different definitions of *F* is shown in Figure 21. Figure 22 displays the improvement in dosimetric results for a patient with implementation of the new definition for F-factor.

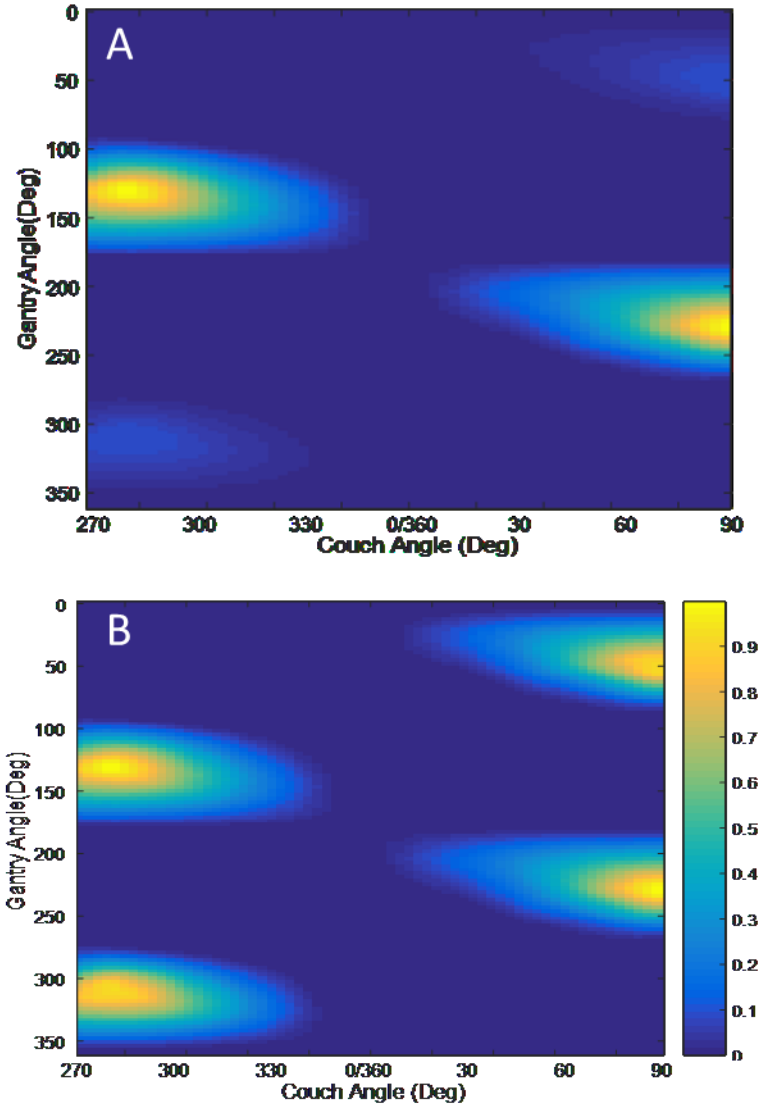

Figure 21: a) - The overlap map between the brainstem and the PTV with the arbitrarily established 10% of foreground overlap that had previously been used [60]. b) - The overlap map between the brainstem and PTV with the PDD-defined F-factor included.

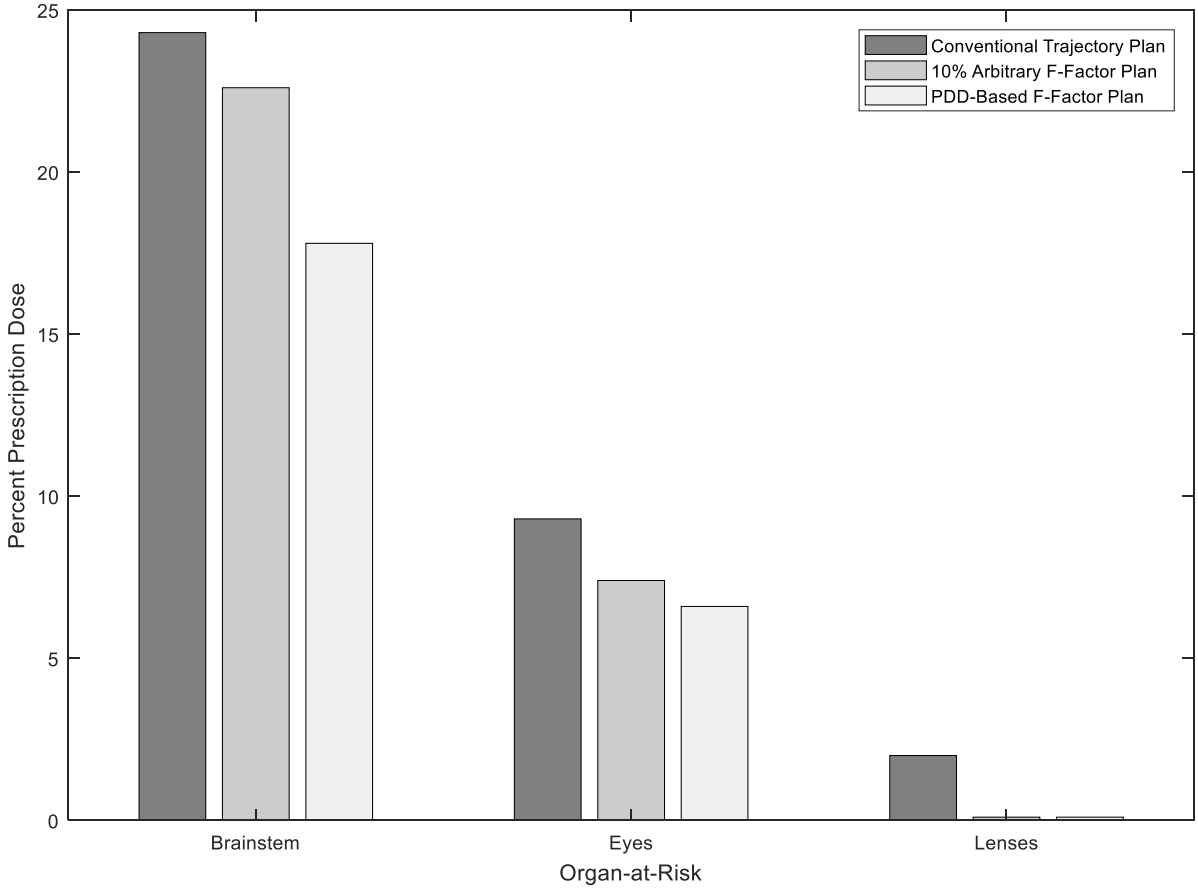

Figure 22: Conventional plans previously delivered compared with the results of optimization of these plans according to the first publication [60], and results of the inclusion of the improved foreground overlap factor (F-factor).

3.4.4 Urgent Sparing Factor

Another factor has been introduced as an addition to the existing cost equation in order to identify radiation therapy couch and gantry positions that further limit any involvement of a specified OAR in the beam's aperture.

This new urgent sparing factor (USF) aims to address the need for limiting excessive exposure to an OAR in close proximity to the PTV. In some patient geometries, an OAR (e.g., the brainstem) is at risk of receiving high dose on the edge closest to the PTV. This factor is included to increase the priority of sparing the proximal edge of the OAR when designing a trajectory. By taking advantage of the anatomical arrangement of

the PTV and the OAR in need of further sparing, the factor promotes the use of trajectories which are orthogonal to the vector joining the two structures, thus maximizing dose fall-off in the direction of the OAR.

To calculate this factor for any OAR, a 3D vector is drawn that joins the two nearest points of the OAR and the PTV ($\vec{b}$ in Figure 23). Another 3D vector is then established for each couch rotation and gantry rotation position which joins the source of radiation to the isocentre at which the PTV is centered ($\vec{a}$ in Figure 23). The angle (α) between these two 3D vectors is then computed by adding 90 degrees (π/2 radians) to the arctangent between the plane to which the vector joining source and isocentre is normal, and the vector joining the OAR and PTV at their nearest points. This establishes the angle (α) between the two 3D vectors measured by the shortest circle path between them and ensures that the angle found lies between 0 and 180 degrees (0 and π radians). Figure 23 displays a geometrical representation of the variables in the calculation of this value. In order to compute this for all angles, it can be understood that with each repositioning of the couch and gantry, these vectors change their 3D position. The angle α is calculated by:

$$\propto = \tan^{-1}\left(\frac{\|\vec{a}\times\vec{b}\|}{\vec{a}\cdot\vec{b}}\right) \quad (42)$$

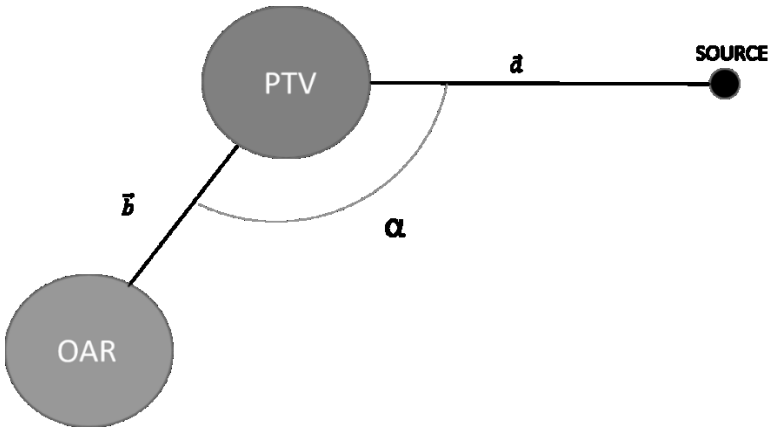

Figure 23: Example of a relative anatomical arrangement and the definition of the 3D vectors used in the calculation of the USF.

Now that this angle α has been established, we want to promote the use of couch and gantry coordinates which force those two vectors to be orthogonal, or α to approach 90 degrees (π/2 radians). As such, we compute the absolute value of the cosine of the angle drawn by the two vectors and add that value to the output of the cost equation. This aligns with the computation of score, as a geometric overlap corresponds to α = 0 or 180 degrees (0 and π radians) or cos α = 1, which gives a maximum value to *E(c,g)*. The full implementation of the overlap metric as implemented in a cost equation for an individual coordinate is thus defined as:

$$E(c,g) = \sum_i \left(\frac{1}{D_{tol_i}} \times \left(\frac{PDD(d_i)}{PDD(d_t)} \right)_{c,g} \times \left[\frac{L_i(c,g)}{A_t(c,g)} \times \frac{L_i(c,g)}{A_i(c,g)} \right] + \left| \cos\left(\tan^{-1}\left(\frac{\|\vec{a}\times\vec{b}\|}{\vec{a}\cdot\vec{b}} \right) \right) \right| \right) \quad (43)$$

3.4.5 Collision Zones

Due to the physical configuration of the gantry and couch, there exists CG-coordinates that are not valid for entry in the geometric overlap map due to possible collision between the gantry and couch or patient. These collision zones were measured on a Varian TrueBeam STx (Varian Medical Systems, Inc., Palo Alto, USA) linear accelerator at the NSHA [60]. An anthropomorphic phantom was placed on the couch and

the couch was placed at typical coordinates for a cranial treatment: longitudinal position of 90.85 cm, a vertical position of 15.00 cm, and a lateral position of 0.00 cm. The gantry and couch were rotated over their full range of motions. A point in a collision zone was recorded for which the couch position and gantry position were such that: (i) the collision avoidance system of the TrueBeam was triggered, or (ii) the gantry was within a 5 cm buffer to either the treatment bed or the anthropomorphic phantom. The CG-coordinates within these zones were forbidden zones for the trajectory path. These collision zones were much less conservative than those found in Yang *et al.* [47], which occupy two full quadrants of the overlap map. These zones provide only a conservative estimate of the LINAC collision space and are highly dependent on isocenter location and patient dimensions. Further refinements of these collision zones will aim to generate them on a patient specific basis.

3.4.6 Treatment Planning

Using sixteen previously delivered cranial SRT plans treated at the NSHA, we've redesigned the treatment arrangement (see Table 3) to find the optimal couch rotation position based on the reduction of overlap between OARs and PTV.

Table 3: The conventional SRT arc template used at the NSHA [3]. These coordinates are in the IEC 1217 system [87].

Couch Angle (°)	**Gantry Start** (°)	**Gantry Stop** (°)	**Gantry Direction**
45	180	0	CCW
0	180.1	179.9	CW
90	150	355	CCW
315	0	180	CW

Maintaining the number of arcs and arc length from the delivered treatment, the couch position was determined based on a cost function analysis of accumulation of

overlap along an arc length, finding the least amount of score from Equation 43 over all couch angles. This principle was first developed to guide non-coplanar, continuous gantry-couch trajectories [60] in which the gantry and couch angle may be modified from point to point in the GOS map based on the lowest amount of overlap available. An example of the optimized couch positions is shown in Figure 24 as overlaid on the GOS map. These arcs result in the lowest value of overlap. Unique fixed-couch, 4-arc treatment plans were generated based on the above cost function analysis of overlap for each patient and then dosimetrically compared to the conventionally delivered VMAT treatment plans. Both couch-optimized and clinical plans were optimized using identical VMAT optimization parameters and three iterations on the optimizer. Although the clinical cases were reoptimized for this study, they were clinically acceptable. The Eclipse treatment planning system v.11 (Varian Medical Systems, Inc, Palo Alto, USA) was used for VMAT optimization (PRO v.10) and dose calculation (AAA v.10). Two plans with optimized couch positions were created: one with only the F-factor and w_i in the cost equation, and one with the F-factor, w_i, and the USF in the cost equation.

Calculation of a GOS map with one-degree resolution took approximately 45 minutes in MATLAB on a PC (Intel® Core™ i5-3570 CPU @ 3.4 GHz, 4 GB RAM), while optimization of couch angles took only a few seconds. GOS map generation would be drastically improved if compiled code was used and the resolution of the maps was decreased.

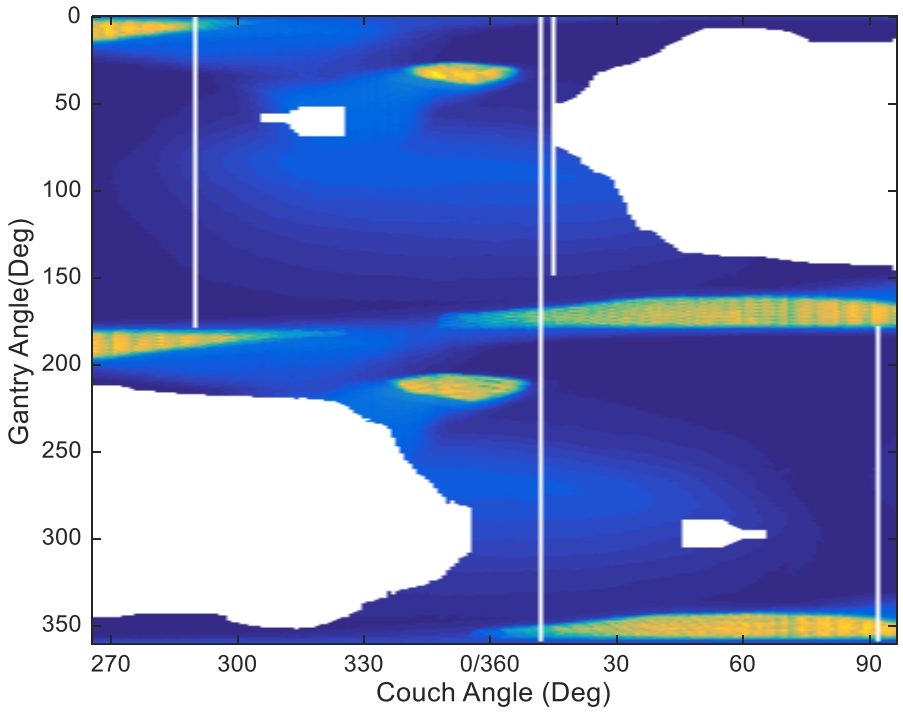

Figure 24: A geometric anatomical overlap map for a cranial cancer patient with an optimized fixed-couch trajectory overlaid. The large white areas and small white islands indicate collision zones. The vertical white lines are the trajectories output from cost function analysis of overlap.

PTV coverage for all plans was set such that the 90% isodose curves covered 99.5% of the PTV volume. The dose homogeneity (*HI*) [84] (see Equation 44) and dose conformation number (*CN*) [85] (see Equation 45) of the PTV were then compared between the conventional and optimized trajectory plans:

$$HI = 100\% \times \frac{D_5 - D_{95}}{D_P} \quad (44)$$

$$CN = \frac{V_{PTV,RI}}{V_{PTV}} \times \frac{V_{PTV,RI}}{V_{RI}} \quad (45)$$

where D_5 is the dose given to 5% of the target volume, D_{95} is the dose given to 95% of the target volume, D_P is the prescription dose, $V_{PTV,RI}$ is the volume of the PTV covered by the 90% isodose line (reference isodose), V_{PTV} is the volume of the PTV, and V_{RI} is the volume of the 90% isodose line (reference isodose). Lower values of *HI* indicate a more homogenous dose distribution within the PTV. Values of *CN* can range from 0 to 1,

where 1 indicates that the reference isodose covers the PTV exactly and 0 indicates a geographical miss or that the reference isodose covers a volume much larger than the PTV.

To evaluate the performance of our treatment planning optimization in clinically demanding scenarios, we have chosen to focus on patients within the NSHA database diagnosed with an acoustic neuroma. As the lesion in these cases can be directly abutting the brainstem, it is a challenging task to spare dose to the brainstem while maintaining uniform tumor coverage. Thus, the brainstem was the only OAR weighted with the USF.

3.5 RESULTS

3.5.1 Optimization of Trajectories with F-Factor

The optimization was performed on sixteen cranial cancer patient plans with acoustic neuromas and resulted in a maximum dose reduction to the OARs of 19.83% ± 3.83% and a mean dose reduction to the OARs of 27.35% ± 2.90% when compared to conventional trajectory plans. For all patients, the mean dose homogeneity was 6.55% ± 0.16% for conventional trajectory plans and 5.69% ± 0.09% for optimized trajectory plans. The mean dose conformation number was 0.79 ± 0.01 for conventional trajectory plans and 0.81 ± 0.01 for the optimized trajectory plans.

Figures 25 and 26 are plots of the dose volume histograms (DVHs) of the PTV, brainstem, and eyes of a typical patient.

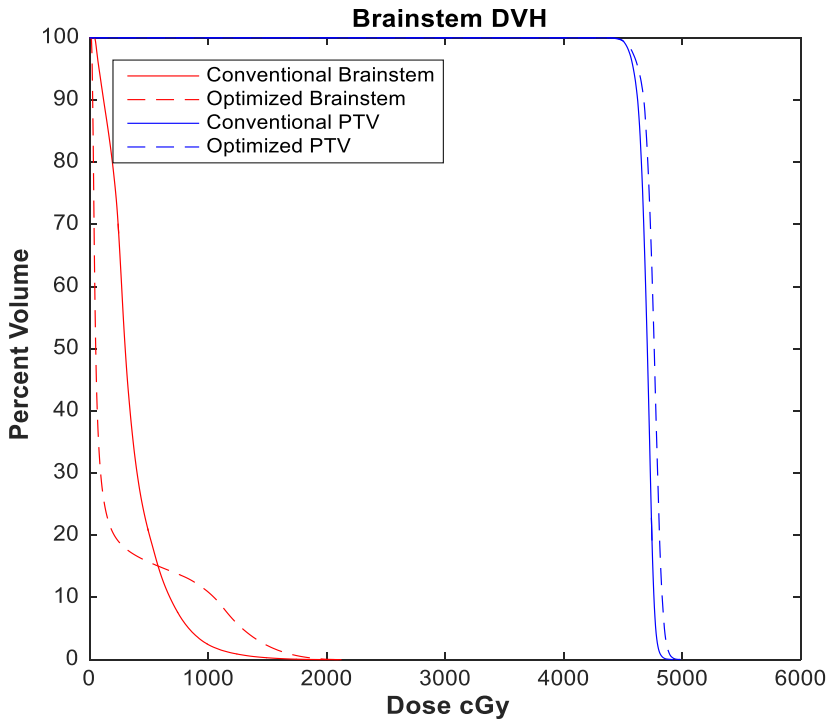

Figure 25: Dose volume histograms (DVHs) of the PTV and the brainstem for an acoustic neuroma patient optimized with F-factor only.

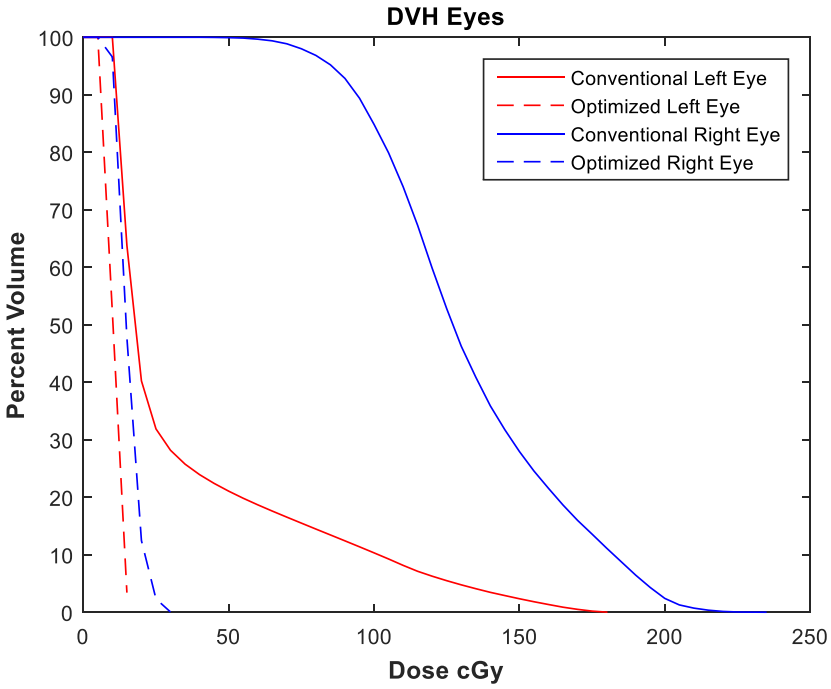

Figure 26: Dose volume histograms (DVHs) of the left and right eyes for an acoustic neuroma patient optimized with F-factor only.

3.5.2 Optimization of Trajectories with F-Factor and USF

A second optimization was performed on the sixteen cranial cancer patient plans in an effort to further reduce dose to the brainstem and resulted in a maximum dose reduction to the OARs of 14.30% ± 2.86% and a mean dose reduction to the OARs of 19.25% ± 2.10% when compared to conventional trajectory plans. For all patients, the mean dose homogeneity was 6.55% ± 0.16% for conventional trajectory plans and 5.71% ± 0.09% for optimized trajectory plans. The mean dose conformation number was 0.79 ± 0.01 for conventional trajectory plans and 0.81 ± 0.01 for the optimized trajectory plans. Additionally, the brainstem maximum dose reduction was 6.88% ± 5.65% in the first optimization and with the implementation of the USF, the maximum brainstem dose reduction was 8.68% ± 4.32%, an increase in sparing of approximately 2% of initial dose.

Figures 27 and 28 show the mean and maximum dose reduction for a single patient optimized with F-factor and USF applied to the brainstem, respectively. Figures 29 and 30 show the mean percent dose reduction for all patients examined and each OAR, in terms of initial plan doses.

To emphasize this general quality of the method, optimization (F-factor and USF) was applied to five additional cranial cases that were not acoustic neuromas, and with target volumes more distant from the brainstem (right parietal adenocarcinoma, parietal metastasis, central occipital metastasis, post fossa meningioma, and left frontal meningioma). Without the brainstem immediately proximal to the PTV, it was less frequently in occlusion with the target, and was more easily spared in general (see Figure 31). The average maximum dose reduction to OARs was 34.2%, indicating that this optimization is applicable to other locations within the cranium.

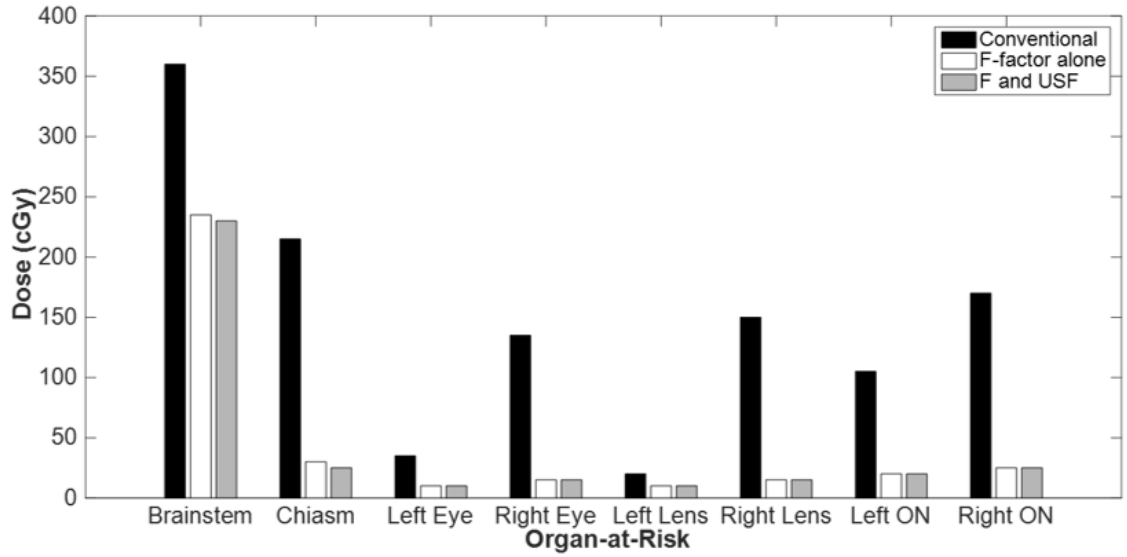

Figure 27: Mean dose for OARs from a single patient optimized with F-factor and the USF applied to the brainstem.

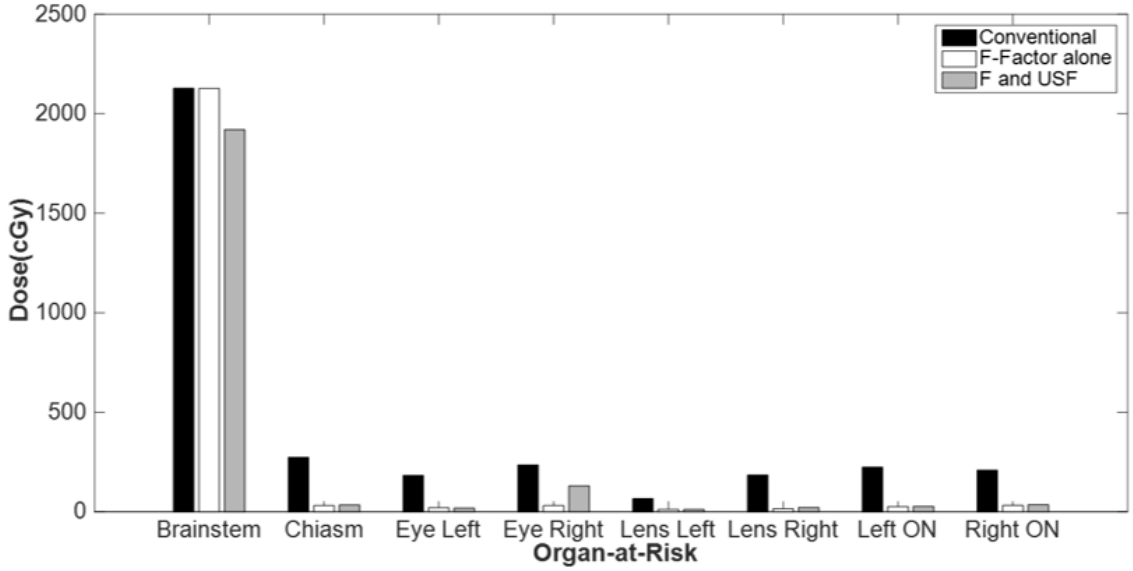

Figure 28: Maximum dose for OARs from single patient optimized with F-factor and the USF applied to the brainstem.

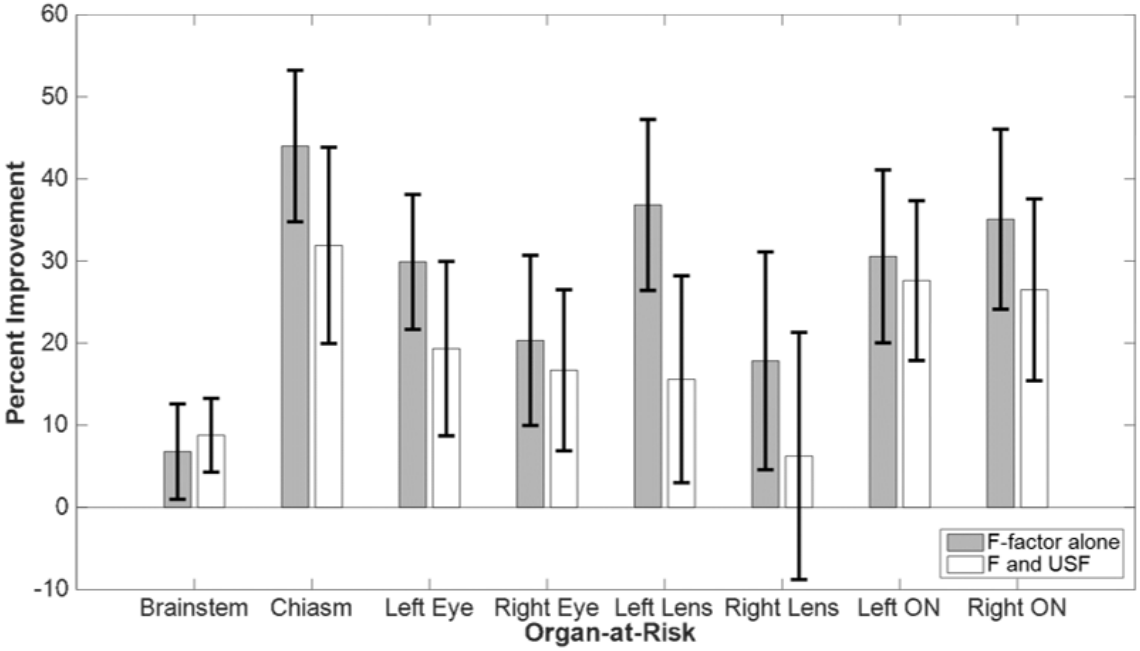

Figure 29: Averaged percent reduction of mean dose for each OAR. This optimization was performed with F-factor and USF applied to the brainstem (N = 16).

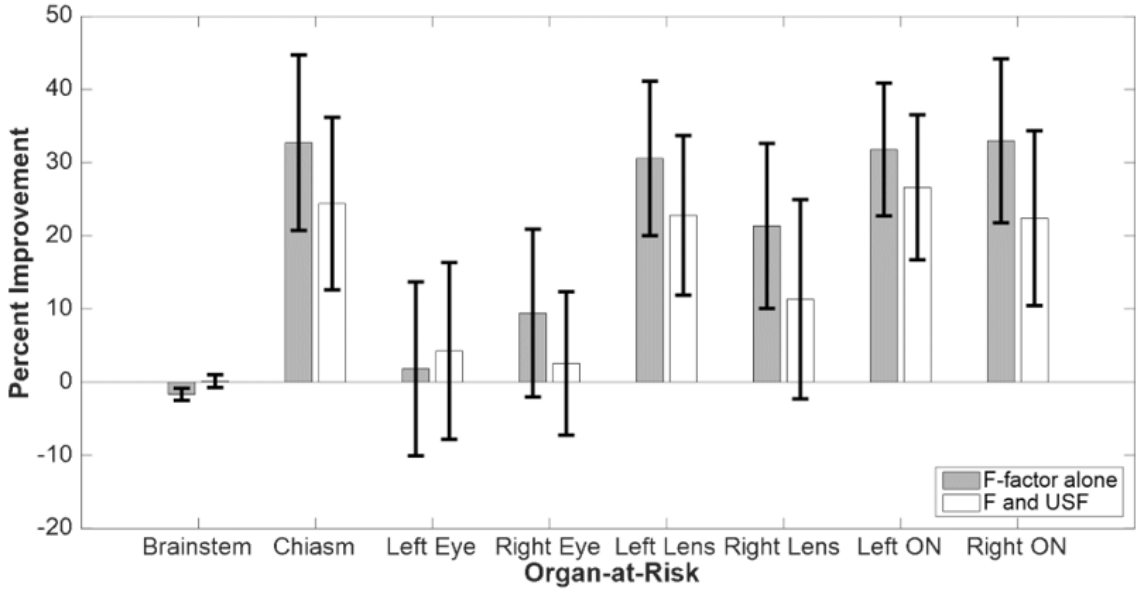

Figure 30: Averaged percent reduction of maximum dose for each OAR. This optimization was performed with F-factor and USF applied to the brainstem (N = 16).

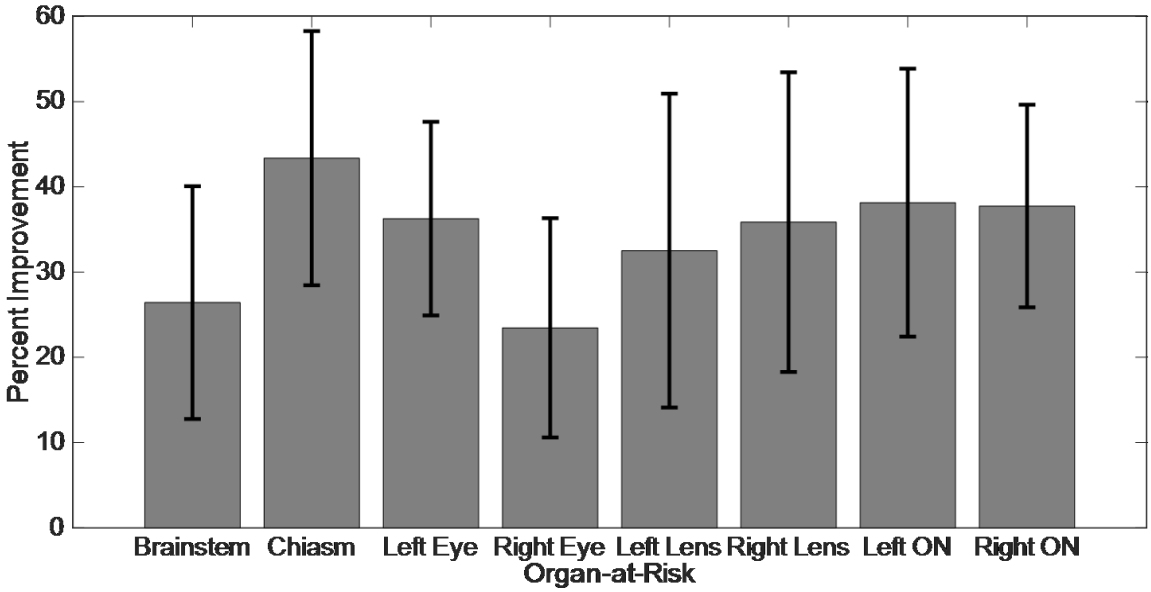

Figure 31: Average percent improvement to OARs in five non-acoustic neuroma cranial cases of differing size and location by using F-factor and USF in the trajectory design.

3.5.3 Arc Elimination

The optimization and treatment can be abridged by removal of arcs that, after optimization, are found at similar couch rotational angles. Frequently, in the methodology described above, ideal locations on the GOS map will be recommended for multiple arcs. When arcs become too close to one another, their individual contributions could be merged into one arc without loss in OAR sparing and PTV coverage. In order to test this hypothesis, five patients in which arcs in the plans measured using F-factor alone were found to be within 10 degrees of couch position (and occupying the same gantry space) were merged, and a 3-arc plan was compared to initial optimization. If one arc was longer, that arc was retained and the shorter was eliminated. This modification altered maximum doses to these patients by 0.422 % ± 2.93 on average (N = 5) when compared to non-combined optimization, suggesting that, in some cases, the simplification of these plans does not affect their dosimetric qualities. Although, in the case of arcs with couch

positions less than 10 degrees apart, a splaying of the intermediate dose may be seen. This further indicates that possible elimination of redundant arcs is possible, and indeed may be desirable, with the result being decreased treatment time and possibly an improvement in the intermediate dose region surrounding the PTV.

Table 4: P-values as a result of a Wilcoxon-rank sum analysis of the mean doses for each of the acoustic neuroma patients (N = 16). * indicates statistical significance ($p < 0.05$).

Organ	Conventional vs F-Factor	Conventional vs F & USF	F-Factor vs F & USF
Brainstem	0.0562	0.436	0.3195
Chiasm	0.0065*	0.0266*	0.1224
Left Eye	0.1729	0.1988	0.7236
Right Eye	0.0974	0.1218	0.4193
Left Lens	0.0923	0.1654	0.4603
Right Lens	0.1282	0.335	0.0777
Left Optic Nerve	0.0018*	0.0064*	0.536
Right Optic Nerve	0.0243*	0.1322	0.2444

Table 5: P-values as a results of a Wilcoxon-rank sum analysis of the maximum doses for each of the acoustic neuroma patients (N = 16). * indicates statistical significance ($p < 0.05$).

Organ	Conventional vs F-Factor	Conventional vs F & USF	F-Factor vs F & USF
Brainstem	0.1635	0.893	0.0358*
Chiasm	0.0148*	0.0215*	0.2653
Left Eye	0.8838	0.7047	0.58
Right Eye	0.1869	0.3851	0.1356
Left Lens	0.0259*	0.0596	0.3784
Right Lens	0.0593	0.1651	0.0832
Left Optic Nerve	0.0062*	0.0104*	0.8918
Right Optic Nerve	0.0212*	0.1763	0.2553

Table 6: Mean conformity and homogeneity indices for each of the treatment plans (N = 16).

Treatment Plan	Conformity Number	Homogeneity Index (%)
Conventional	0.79 ± 0.01	6.55 ± 0.16
F-Factor	0.82 ± 0.01	5.69 ± 0.09
F & USF	0.81 ± 0.01	5.71 ± 0.09

Table 7: P-values for Wilcoxon-rank sum analysis of the indices between each of the treatment plans (N = 16).

Comparison	Conformity Number	Homogeneity Index
Conventional vs F-Factor	p = 0.1225	p = 0.0995
Conventional vs F & USF	p = 0.1812	p = 0.1311
F-Factor vs F & USF	p = 0.3115	p = 0.8463

3.6 DISCUSSION

Initial implementation of our optimization based on cost function analysis of overlap using F-factor only resulted in an average sparing to the sixteen-patient population of approximately 20% in maximum doses, and approximately 27% in mean doses. It should be noted that the metric used to examine reduction to these OARs was the percent improvement (Figures 29 - 31), which examines the relative change in dose to these structures with optimization compared to conventional VMAT. This metric can show small gains when large doses are marginally decreased, as is the case with the brainstem, and large gains when gains are made to initially small doses, as with distant OARs. Most successfully, dose was spared to the optic chiasm and the optic nerves, as the reduction in these structures reached a statistical significance when examined with a Wilcoxon ranked-sum analysis (Tables 4 and 5). Additionally, conformity and homogeneity of dose to the target were improved with our optimization, but the improvement was not statistically significant when compared to equivalent conventional trajectory planning (Tables 6 and 7). When we examine Figures 29 & 30, we can see that plan optimization was successful on average for these sixteen cases, with the exception of reducing maximum dose to the brainstem, the most proximal OAR to the target volume. While all other metrics of plan quality improved with initial optimization, brainstem maximum doses worsened with application of initial optimization. It is for this reason that we have created the USF, and in this study, applied its focus to the brainstem.

As can be seen from Figures 27 - 30, the USF was able to preferentially reduce mean doses to the brainstem by an additional 2% (approximately 9% total) of conventional dose, and reduce maximum dose to brainstem by 1.5%, and in one case,

reduce maximum dose to brainstem by 10%. This reduction in brainstem dose was achieved with average reduction to maximum dose of 14% and mean dose of 19% across all OARs. When the application of optimization using F-Factor alone is compared to optimization with inclusion of the USF on the brainstem, the only statistically significant difference between them, is dose to the brainstem. This implies that inclusion of the USF for brainstem has no significant effect on the other OARs. The implementation of both F-Factor alone and F-Factor with USF did not yield statistically significant differences in brainstem maximum dose from the conventional VMAT plans. However, there was statistical significance between the optimized plans without USF and with USF. This indicates that while initial optimization without the USF in these plans on average worsened the maximum dose to the most proximal OAR, the inclusion of this factor was able to retain the majority of sparing to more distant OARs, and recover the sparing of the most proximal OAR.

The USF was additionally implemented in the arc optimization of acoustic neuroma cases treated in an experimental version of Brainlab's Cranial SRS Elements planning system and examined relative to plans optimized without this factor. The most notable effect was the consistent reduction of dose to the brainstem D10% with inclusion of the USF as is shown in Figure 32.

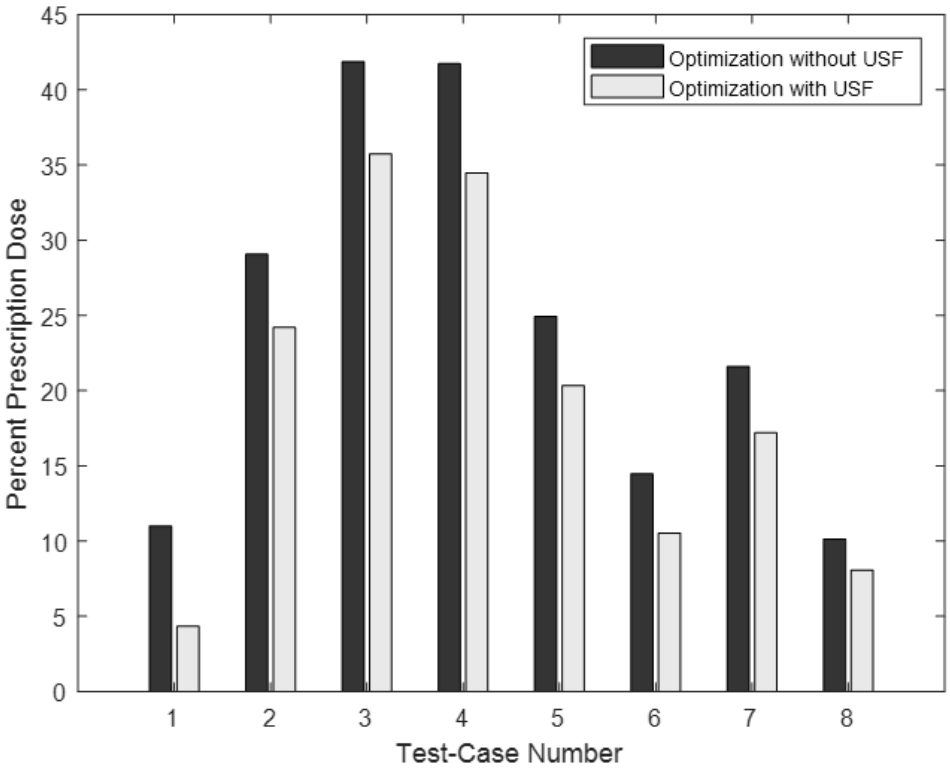

Figure 32: The value of the brainstem D10% with and without implementing the USF in the treatment of eight acoustic neuroma cases.

Though not present in the patient population of this study, in cases where a proximal OAR occupies the same physical volume within the cranium as the target volume (physical overlap as opposed to BEV overlap), the vector b, as illustrated in Figure 23, can be applied to the portion of the OAR outside of the PTV. This would, in effect, apply the sparing afforded by the USF to that external portion of the OAR, potentially decreasing the mean dose of the OAR.

By repositioning the standard SRT trajectory template to minimize the amount of cumulative score based on Equation 43, we have reduced the inclusion of OARs within the BEV in the overall delivery. The optimization's efficacy can be noted from the reduction in dose to these structures when compared to a conventional treatment without

optimization for dose reduction to OARs (apart from the VMAT optimization present in all SRT VMAT treatments). The reduction of both mean and maximum dose values is, on average, common to all OARs specified for inclusion in the optimization.

In a select few patients, there are marginal increases of dose to some of the patient's OARs, usually in a pattern which suggests a preferential reduction to one lateral side of the patient. In patients found to have increased doses to OARs after optimization, this can likely be attributed to the fixed nature of the gantry trajectories. As the start and stop angles for the gantry have not been optimized, this is a limitation on the lack of complexity of the trajectory and could in some instances cause non-optimal BEV angles to be selected. This study does not examine the optimization of gantry start and stop angles, as it aims to isolate the benefit of optimizing couch angle alone. Shortening or lengthening of arcs in combination with couch angle optimization is another degree of freedom to investigate, although shortening of arcs may result in a skewing of the dose distribution along the axis of the arc [28], which in turn will affect the conformity of the prescription isodose and intermediate dose levels. When trajectories with a higher degree of complexity, and without these limitations, have been applied to treatment plans [60], statistical analysis indicated higher degrees of consistent sparing across a patient population.

Table 2 includes dose constraints for the OARs used in this study in an attempt to quantify the relative differences in sensitivity between these structures. While the treatments optimized in this study do not use the protocols with which the dose constraints in Table 2 apply, these values were chosen in order to highlight a context in which the constraints to these structures are distributed more widely than in SRS/SRT

dose protocols. The validity of these relative weighting factors can be validated in future studies to examine trade-off scenarios between OARs.

This study reflects the benefits of applying the USF to the brainstem in acoustic neuroma patients, however, the USF can be applied in other clinical scenarios that involve the need to additionally spare OARs at very close proximity to the target, so long as there is sufficient distance between the two such that a vector, b, (as shown in Figure 23) can be drawn.

Table 8 gives a comparison of fixed-couch trajectory optimization results to the previously published results of Yang *et al.* [47]. Column 3 is simply a subtraction of the results in column 1 and 2 (our data), whereas column 4 is taken from Yang *et al.* [47]. While percent improvement between the two techniques is the same (compare average values from columns 3 and 4), normalized improvement (the reduction normalized by the dose present in the clinical plan) is superior in our study (compare average values from columns 5 and 6). However, these two methods of delivery are very different, as our trajectory optimization is implementable immediately as it requires only a modification of the couch angle based on consultation of a GOS map, while the trajectories proposed in Yang *et al.* [47] and in MacDonald *et al.* [60] require the development of a clinical linear accelerator capable of simultaneous couch and gantry motion in a dynamic non-coplanar VMAT delivery. The advantage of this fixed-couch based trajectory optimization is that it does not rely on simultaneous motion of gantry and couch and can be implemented on any linear accelerator capable of VMAT delivery.

Table 8: Average dose values for OARs compared to those available in Yang *et al*. [47]. All dose values are in percent prescription dose.

	Conventional Trajectory (%)	Optimized Trajectory (F & USF) (%)	Improvement (%)	Improvement (Yang *et al* [1] data) (%)	Normalized Improvement (%)	Normalized Improvement (Yang *et al* [1] data) (%)
Brainstem D_{max}	93.8 ± 5.8	93.6 ± 4.5	0.2	1.1	0.2	1.1
Brainstem D_{mean}	12.0 ± 5.9	11.0 ± 6.0	1.0	2.3	8.3	4.0
Chiasm D_{max}	22.2 ± 43	18.3 ± 40.6	3.9	1.6	18	2.0
Chiasm D_{mean}	5.3 ± 2.7	3.30 ± 3.3	2.0	2.6	38	4.0
Eye D_{max}	8.7 ± 5.5	8.5 ± 7.7	0.2	-0.3	2.3	-1.3
Lens D_{max}	5.4 ± 4.7	4.7 ± 5.6	0.7	0.5	13	9.4
Optic Nerve D_{max}	20.9 ± 43.6	17.2 ± 40.8	3.7	2.3	18	3.9
Optic Nerve D_{mean}	4.0 ± 2.4	3.3 ± 2.8	0.7	2.9	18	8.6
Average			**1.6**	**1.6**	**14**	**3.9**

3.7 CONCLUSION

The variation of the existing delivery techniques with guidance from a PTV-OAR overlap cost-function analysis technique yields dosimetric improvements, with no increase to delivery or planning time, except for calculation time of the GOS.

The creation of radiotherapy trajectories based on the minimization of overlap between OARs and PTV is an effective means to increase dose sparing to OARs in the majority of cranial cancer treatments. In a test-patient population study of sixteen acoustic neuroma cranial SRT patients, the average mean dose reduction to OARs was 27% and the average maximum dose reduction to OARs was 20% of the initial dose given in the treatment of these patients with the use the F-factor alone, and by 19% and 14% with incorporation of the USF as well. A reduction of dose to each OAR upon utilization of this fixed-couch trajectory optimization technique was seen on average in the patient population. To measure the effectiveness of cost function analysis optimization of plans plan on treating the target, we've used two indices: the

homogeneity index [84] and the conformation number [85]. Dose homogeneity within the PTV and conformity of prescription isodose to the PTV was improved in the optimized plans when compared to the conventional delivered treatment plans, although not statistically significant.

Apart from couch rotation angles, the optimized treatment plan is equivalent to a conventional trajectory treatment plan in terms of time of delivery, prescriptions, normalization, and VMAT dose objectives. These results illustrate the potential advancements to stereotactic treatment of challenging cases with the implementation of patient-specific overlap analysis.

The novelty of our method is that it uses the geometric position of the PTV and OARs to guide arc placement in an intuitive manner. This method is easily implementable in any oncology facility and is independent of the ability of the LINAC to simultaneously move the gantry and the patient couch. In addition, our method can also be used in the context of conventional fixed port conformal treatment planning to aid in beam placement.

CHAPTER 4 MANUSCRIPT 2: DYNAMIC COLLIMATOR TRAJECTORY ALGORITHM FOR MULTIPLE METASTASES DYNAMIC CONFORMAL ARC TREATMENT PLANNING

4.1 PROLOGUE

This manuscript is the first foray into dynamic collimator optimization, and as a result, is a thorough description of the challenges and solutions therein. It is an application of the methodologies described in Sections 2.3.1, 2.3.2.2, and 2.3.3.4 as it uses a novel cost function as input to generate a 2D catalogue, from which a traversal trajectory generates collimator rotation instructions for the MLC on the LINAC.

While this method is capable of general application in any radiotherapy BEV, here it is applied in the clinical setting with which it is likely to be most beneficial: the minimization of normal tissue exposure in multiple metastases settings. By collimating the conformal MLC as efficiently as possible, the aim is to reduce dose to normal tissues between targets, and hence minimizing the volume of healthy brain receiving intermediate to high dose values. Another by-product of this optimization is increasing the area of the aperture delivering dose to the target volumes throughout the treatment. This returns a greater efficiency of MU throughout treatment compared to the conventional VMAT plans that require frequent collimation of target sub-sections in order to accomplish global dosimetric benefit.

This chapter includes the validation of this technique and comparison of dynamic collimator DCA plans to expert-planned VMAT plans.

Publication: *MacDonald, R. Lee, Christopher G. Thomas, and Alasdair Syme. "Dynamic Collimator Trajectory Algorithm for Multiple Metastases Dynamic Conformal Arc*

Treatment Planning." Medical Physics 45, no. 1 (January 1, 2018): 5–17. https://doi.org/10.1002/mp.12648.
The included chapter differs only from the publication in the addition of revisions for additional clarity.

4.2 ABSTRACT

Purpose: To develop an algorithm for dynamic collimator positioning to optimize beam's-eye-view (BEV) fitting of targets in dynamic conformal arc (DCA) based radiotherapy procedures, of particular use in multiple metastases stereotactic radiosurgery procedures.

Methods: A trajectory algorithm was developed to dynamically modify the angle of the collimator as a function of arc-based control point to provide optimized collimation of target volume(s). Central to this algorithm is a concept denoted herein as "whitespace" defined as any non-target area in the BEV that is not covered by any collimation system and is open to exposure from the radiation beam. Calculating whitespace at all collimator angles and every control point, a two-dimensional topographical map depicting the tightness-of-fit of the MLC was generated. A bi-directional gradient trajectory algorithm identified a number of candidate trajectories of continuous collimator motion. Minimization of integrated whitespace was used to identify an optimal solution for the navigation of the parameter space. Plans with dynamic collimator trajectories were designed for multiple metastases targets and were compared with fixed collimator angle dynamic conformal arc (DCA) plans and standard VMAT plans.

Results: Algorithm validation was performed on simple test cases with known solutions. The whitespace metric showed a strong correlation ($R^2 = 0.90$) with mean dose to proximal normal tissue. Seventeen cases were studied by using our algorithm to generate

dynamic conformal arc (DCA) plans with optimized collimator trajectories for three and four target SRS patients and comparing them to DCA plans generated with optimized fixed collimator angles per arc and standard VMAT plans generated via template. Optimized collimator trajectories were found to produce a reduction in monitor units of up to 49.7 ± 5.1% when compared to VMAT across seventeen patients, and all organ-at-risk and normal brain metrics were found to be superior or comparable.

Conclusion: Dynamic collimator trajectories have the potential to improve DCA deliveries through increased efficiency, especially in treatment of multiple cranial metastases. Implementation of this technology should not be hindered by mechanical safety considerations as collimator motions do not modify or introduce any new risks of collisions with patients.

4.3 INTRODUCTION

In conventional arc-based radiation therapy, including VMAT and dynamic conformal arc (DCA), the gantry of the linear accelerator rotates around the patient and the leaves of the MLC are driven through a pre-determined motion pattern to facilitate aperture modulation (VMAT) or target conformity (DCA). In previous research, the inclusion of couch rotational motion has been explored [1, 2]. To date, there has been limited investigation of dynamic collimator motions.

When treating multiple targets or targets with irregular shapes that include concavities, the projection of the target(s) as seen from the beam's eye view (BEV) will change as a function of control point (i.e. as the couch and/or gantry rotate). Consequently, the ability of the MLC to conform to the target(s) while shielding healthy tissue at each control point can be a strong function of collimator angle. As such,

dynamic collimator motions during treatment arcs could serve to continuously re-orient the MLC to facilitate optimal target coverage and normal tissue shielding throughout the delivery.

Dynamic collimator motions in the age of modulated treatment deliveries were first introduced in the context of collimator rotation intensity modulated radiotherapy (CR-IMRT), sometimes referred to as rotating aperture optimization (RAO) [3 - 6]. In this application, the collimator would rotate while the couch and gantry remained static and the leaves of the MLC would be driven through a pre-calculated motion pattern. The purpose of this technique was to increase the achievable resolution of fluence modulation that was otherwise limited by the fixed width of the MLC leaves in the direction perpendicular to the direction of leaf travel. With the increasing use of volumetric modulated arc therapy (VMAT) treatment deliveries, the relevance of techniques such as CR-IMRT in a modern clinic has been significantly diminished. In VMAT treatment deliveries, the concept of "modulation" has changed. In static gantry IMRT, MLC motions introduced a two-dimensional, spatially varying fluence intensity pattern across the treatment field. In VMAT deliveries, fluence intensity modulation is non-existent (outside of the naturally occurring spatial variation that is found in the unmodified beam profile). Instead, the shape of the field aperture is modulated as the gantry rotates to realize the objectives of the treatment plan.

The concept of dynamic collimator motions during arc therapy is relatively new and little literature exists on the subject. Webb [70] first studied the potential benefits of dynamic collimator rotations from the point of view of minimizing patient dose that results from "parked" MLC leaves in the Elekta Beam Modulator system. The dosimetric

challenge associated with this beam modulation system (a problem that is not common to all MLC models) lies in the fact that opposing MLC leaves must maintain a minimum separation of 5 mm. As such, when there is insufficient time for opposing leaves to park underneath the jaws when that leaf pair is not needed at a control point, substantial unwanted dose can be deposited in the patient. Webb noted that dynamic collimator rotations could significantly reduce the frequency of occurrence of this phenomenon (up to 40% for simple target shapes).

Other works that incorporate dynamic collimator rotations into VMAT treatment deliveries have been published by Zhang *et al* [71] and Yang *et al* [47]. Zhang's approach to identifying an optimal collimator angle was illustrated in the context of paraspinal SBRT. Since the overriding concern in these cases is the dose to the spinal cord, Zhang sought to align the collimator to the principal axis of the cord by using principal component analysis (PCA) to ensure that the spinal cord could be effectively shielded at every control point. As such, the "optimal" collimator angle at a control point is uniquely determined by the PCA and only considers cord orientation. That work does not consider how effectively other collimator angles at a particular control point might be able to provide optimal spine collimation, nor does it consider the optimization of collimation of a target volume.

In order to optimize collimator angle selection, this study aims to define a general solution metric for potential quality of collimation based upon the rotational angle selected. The spatial placement of each of the bi-lateral leaves is not suggested by this metric; instead, it identifies the direction of travel of the leaves in which the fraction of unshielded normal tissue is minimized when individual leaf encroachment into the jaw-

defined field is terminated at first contact with the target volume(s) (see Figure 33). In VMAT treatment planning, minimizing non-target anatomy in the BEV may increase treatment delivery efficiency because fewer control points will force the fluence / aperture optimization process to shield target volumes to prevent healthy tissue irradiation. Normal tissue doses may also decrease because, under certain circumstances, commercial treatment planning systems will choose to include the full target volumes in the shaped aperture at the expense of healthy tissue (see Figure 34).

In this work, the effects of collimator trajectory-derived whitespace minimization in DCA treatments of multiple metastases are studied. To quantify the performance of the algorithm, the results are compared to a fixed collimator DCA and volumetric modulated arc therapy (VMAT). Due to limitations of current commercially available treatment planning systems, dynamic collimator VMAT plans were not created for comparison.

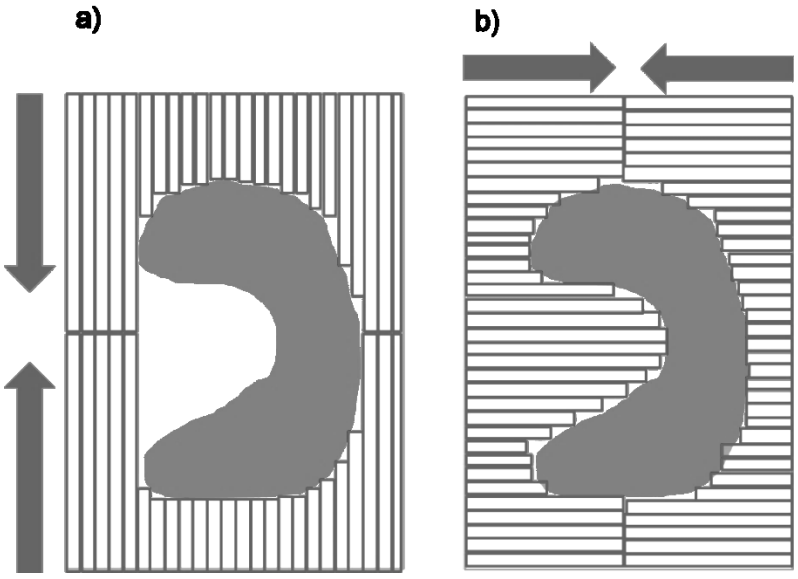

Figure 33: An example of the worst (a) and best (b) collimation directions for a PTV with a convexity. The convex area is the PTV and the boxes indicate the aligned MLC leaves collimating the defined PTV. The arrows indicate the direction of leaf travel.

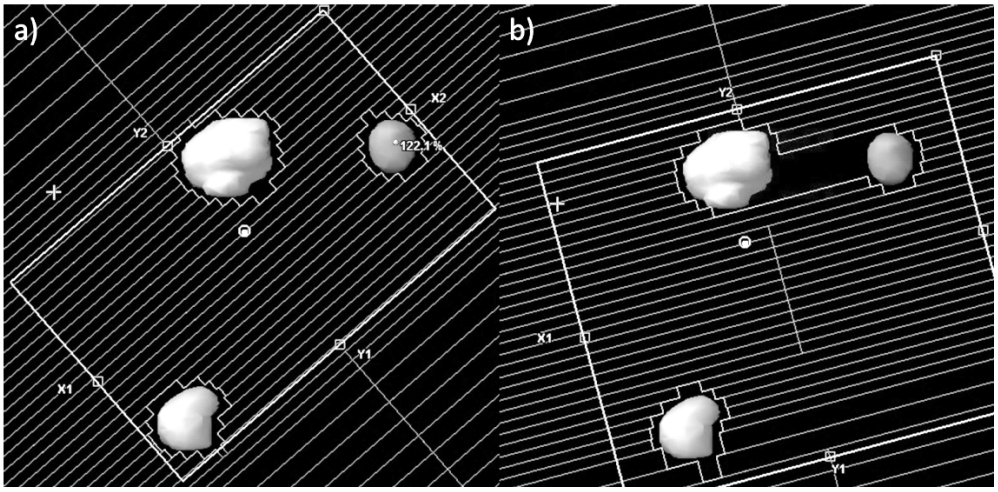

Figure 34: Optimal (a) and non-optimal (b) DCA apertures. Shown in b) is an example of normal tissue being irradiated to accommodate the treatment of multiple targets.

4.4 METHODS

4.4.1 Calculation of Whitespace

In order to assess the suitability of any collimator angle for use in a radiotherapy trajectory, a metric must be defined which can unambiguously rank the quality of collimation direction for any given BEV. The quality of collimation is based on the objectives of the radiotherapy treatment plan, principally to treat the target volume to the prescription dose and to limit dose as much as possible to surrounding healthy tissue.

The area within any BEV can fall into one of the following five categories: 1) area bounded by the jaw, which is the portion of the BEV in which the upper and lower jaws collimate the area in a rectangular shape; 2) area of the PTV; 3) area of overlapping organ-at-risk (OAR) with the PTV; 4) area collimated by the multi-leaf collimation system (MLC) (i.e. BEV area inside the jaws covered by the leaves); and 5) whitespace, which is any non-target area in the BEV that is not covered by any collimation system and is open to exposure from the radiation beam. All areas are calculated from the

projected areas of the volumes, MLC, and jaws onto a plane at isocentre. By categorizing and measuring these areas in any BEV defined by the couch rotation angle, θ_{CH}, gantry rotation angle, θ_{GA}, and any chosen collimator angle, θ_{CL}, the parameter denoted by whitespace (W) can be defined by Equation 46:

$$W(\theta_{CL}, \theta_{CH}, \theta_{GA}) = w_1 A_{Jaw} - w_2 A_{PTV} + w_3 (A_{PTV} \cap A_{OAR}) - w_4 A_{MLC} \quad (46)$$

where A_{Jaw} is the fitted rectangular jaw, A_{PTV} is the area of the PTV, $A_{PTV} \cap A_{OAR}$ is the area of the OAR(s) overlapping with the PTV, A_{MLC} is the area collimated by the MLC in a conformal position, when the entire PTV or PTV – OAR(s) is targeted, and, w_1- w_4 are weighting factors to control the significance of each term. For example, in this work, the overlap between PTVs and OARs is not considered, meaning that $\boldsymbol{w_3}$ has a value of zero. An investigation of the effects of each of the weighting factors on the optimization process is beyond the scope of the current work, and the factors $\boldsymbol{w_1}$, $\boldsymbol{w_2}$ and $\boldsymbol{w_4}$ were as such assigned a value of 1. At each control point, every possible collimator angle has an associated whitespace value that can be quantitatively assessed by Equation 46.

In order to measure all of the values in Equation 46, for any given BEV, a procedure was developed in MATLAB (The MathWorks, Inc., Natick, Massachusetts, USA) to model the constituents in the BEV and measure the areas of each. For this work, a Varian HD 120 MLC (Varian Medical Systems, Palo Alto, California, USA) was used since the clinical plans generated involve stereotactic radiosurgery, although the algorithm is equally applicable to any other MLC design. This MLC was modeled according to the vender specifications for leaf number and width. The HD MLC 120 is composed of two bi-lateral banks, each composed of sixty uniquely motor-positioned tungsten leaves [76]. The central 32 pairs of leaves have a 2.5 mm width and the peripheral

28 leaf pairs have a 5 mm width when projected to isocentre.

Using in-house anatomical projection software previously used to measure the suitability for any given physically feasible couch/gantry angle [60], the patient structure set and plan files are imported into the MATLAB (R.2015b) environment, and the BEV for any treatment arrangement can be projected and used in the assessment of Equation 46.

Measuring and cataloguing the whitespace value at every control point within a radiotherapy arc at unit collimator angles (over the range of 90^{o} to 270^{o}), the information was used to create a two-dimensional whitespace map. This map is used in this study as a treatment planning resource for condensing and visualizing complex patterns of high and low whitespace values inside of a radiotherapy arc.

4.4.2 Validation of Test Case

To verify the correct performance of the calculation, an artificial test case with a known solution was supplied to the software. Two identical 2 cm spherical PTVs were contoured using Eclipse (v.11 Varian Medical Systems, Inc., Palo Alto, USA) and set 3 cm apart, both situated on the cranial-caudal axis of the patient. The beam isocentre was centrally located between the two volumes. All BEVs from a complete, axial, coplanar arc were examined for the test patient, and the normalized (for display only) whitespace was catalogued for each of these points.

4.4.3 Correlation of Whitespace and Dose

To isolate the effects of minimization of whitespace, an investigation was conducted with a controlled patient geometry. A whitespace map was generated for a

two-target patient with single, axial arc geometry. For every valid collimator angle in unit angle increments (90° - 270°, for a total of 181 angles), the integrated whitespace for a fixed-collimator plan was calculated. From these 181 possibilities, 18 DCA plans that fully sampled the range of integrated whitespace values were generated in Eclipse. The normal brain contained in the volume between the two PTVs was contoured and the mean dose to this volume was calculated.

4.4.4 Navigation of Whitespace Map

For a treatment arc with *n* control points, the objective of the whitespace optimization algorithm is to identify a collimator trajectory that minimizes the integrated whitespace in moving from control point 1 to control point *n* while respecting motion constraints that govern the size of the allowable collimator angle change between control points. The current angular velocity limits (for a TrueBeam accelerator) on the gantry and collimator are 6°/s and 15°/s, respectively. This suggests that for a treatment delivery in which the gantry is moving at maximum angular velocity, the maximum allowable change in collimator angle between unit angle increments of gantry motion is 2.5°. However, in large dose per fraction treatments, the number of monitor units in an arc is often larger than that which can be delivered with the gantry moving at maximum velocity, thereby requiring a slowing of the gantry and resulting in a larger allowable collimator angle rotation per degree of gantry motion. Furthermore, if larger collimator angle rotations between control points is desirable, slowing down the gantry is always an option. In this work, we limited the allowable collimator motion to ± 3° between control points when control points are separated by unit angle gantry rotation motions. Currently, this restraint is applied for the purpose of minimizing potential discrepancies between

calculated and delivered fields and based on the above reasoning. The validity of the dosimetric assumption should be independently investigated.

While there are many techniques available to solve this minimization problem, we used a gradient search algorithm in which a path of least resistance is followed between control points. Each allowable collimator angle (181 between 90° and 270° in unit angle intervals) serves as a potential starting point at control point 1. The gradient search then considers all available collimator angles at control point 2 that lie within ± 3° from the position at control point 1 (seven collimator angles in total: -3°, -2°, -1°, 0°, +1°, +2°, +3°). Of these, the collimator angle at control point 2 is chosen as the angle with the lowest whitespace value. If more than one collimator angle at the next control point share the same minimum whitespace value, the gradient search will select the coordinate that requires the least amount of motion from the current position. This operation is repeated for all subsequent control points. Additionally, the search is conducted in reverse, starting from the last control point and working toward the first. The inversely directed gradient produces unique trajectories not identified in the initial search. This bi-directional gradient search produces 362 total candidate trajectories (181 in each direction). The final collimator trajectory selected is the trajectory with the lowest accrued whitespace of all 362 candidate trajectories. The result of a bi-directional search of a whitespace map is shown in Figure 35 for an example case with three targets and a single 360° coplanar arc. To eliminate small changes in whitespace due to the discrete nature of the MLC leaf, a Gaussian smoothing function was applied to the map with a 10-pixel radius to preserve major trends in the whitespace map.

4.4.5 Clinical Cases

Two patients previously treated at the Nova Scotia Health Authority (NSHA) for multiple brain metastases were chosen for this study. Both patients had three PTVs and all volumes were treated with a prescription of 24 Gy prescribed to the 90% isodose. In addition, using one of the clinical CT data sets, fifteen simulated cases were generated using combinations of eight artificial target volumes manually contoured using Eclipse v11. We chose to create artificial targets due to the low number of three and four target clinical cases all with the same prescription dose in our clinical database. The artificial targets span the volume sizes appropriate for a prescription of 24 Gy as per RTOG 9508 [18]. All dose calculations were performed in Eclipse using AAA v.11 with a calculation grid size of 1.5 mm. All artificial targets were within 5 cm of an organ at risk, with four targets closer than 1 cm (0.44 cm from the optic chiasm, 0.74 cm from the brainstem, 0.66 cm from the brainstem, and 0.28 cm from the brainstem) in order to challenge our algorithm. All artificial targets were treated using prescription doses of 24 Gy prescribed to the 90% isodose.

For each case, three plans were generated: a dynamic collimator trajectory plan, with collimator angle changing at each control point based on whitespace score at each control point; a fixed collimator angle plan, with the collimator angle fixed at an optimal angle based on whitespace score over each entire arc; and a VMAT plan with non-optimized, fixed collimator angle for each arc.

Table 9: Gantry and couch parameters for the clinical stereotactic plan used at the NSHA [87]. CW = clockwise, CCW = counter-clockwise.

Couch Angle (°)	**Gantry Start** (°)	**Gantry Stop** (°)	**Gantry Direction**
45	180	0	CCW
0	180.1	179.9	CW
90	150	355	CCW
315	0	180	CW

4.4.6 Dynamic Collimator Trajectory Plans (DCT-DCA)

A standardized DCA treatment template involving four non-coplanar arcs was used, the details of which are provided in Table 9. For each arc, a whitespace map was generated, and the bi-directional gradient search was used to create the collimator trajectory. At each control point, in-house MATLAB code was used to specify the treatment field parameters, namely the collimator angle and leaf positions conforming to the total PTV area (i.e. a Boolean "OR" operation performed on the three target volumes) with a 1 mm margin added. By down-sampling the treatment resolution to 5^{o}, a total of 175 control points were produced in one plan by creating 175 unique static fields. Dose calculations were performed by importing individual treatment fields for each of the control points into Eclipse (Varian Medical Systems, Inc., Palo Alto, USA) and calculated using A.A.A. v.11. To generate optimal MU weights for each arc in the treatment, the dose matrices for each control point in an arc were exported and combined using in-house MATLAB software. This solution was then reimported into Eclipse where the final dosimetric comparison was conducted. This method is expanded in Section 4.4.10.

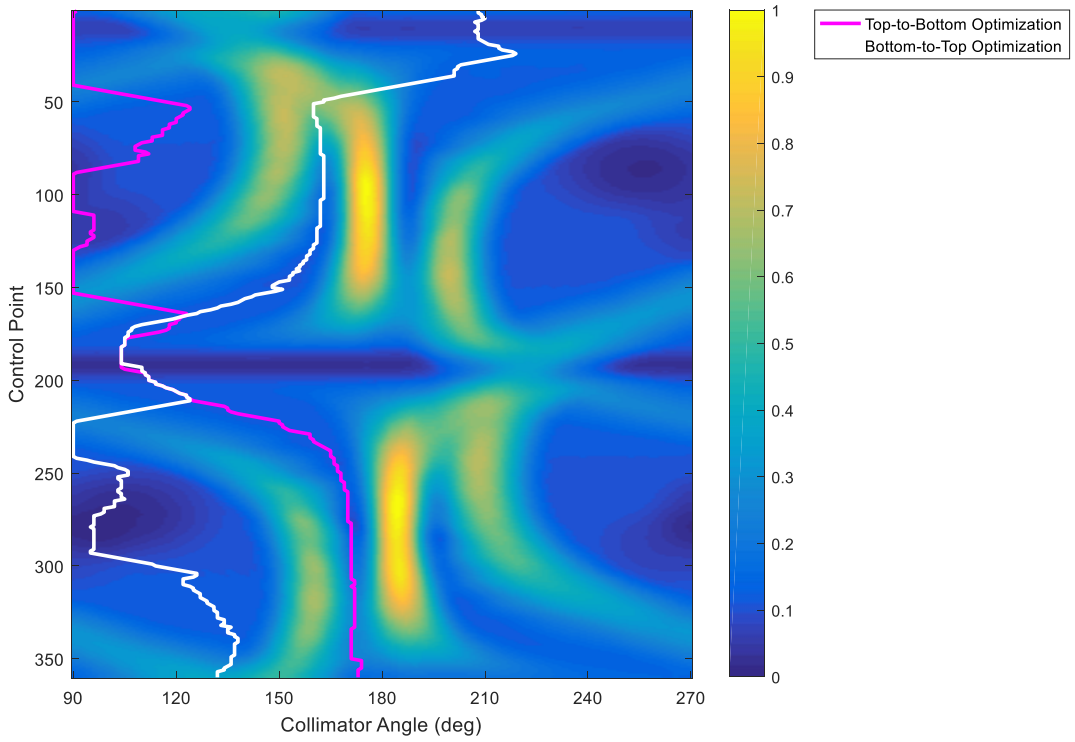

Figure 35: A trajectory designed for a coplanar arc for a three-target clinical case using the bi-directional gradient algorithm in the top-to-bottom direction (magenta), and the bottom-to-top direction (white). The color scale indicates a normalized value of whitespace.

4.4.7 Fixed Collimator Plans (FC-DCA)

For all patients, a DCA treatment plan with whitespace-minimized fixed collimator angles for each arc was created using the arc configuration outlined in Table 9. The plans were generated using DCA arcs with MLC leaves fit to the Boolean "OR" of all three targets, with a 1 mm margin.

4.4.8 VMAT Plans

For all patients, VMAT plans were generated according to the clinical planning procedure at the NSHA. The priority on Eclipse's automatic normal tissue objective (NTO) function was set 25 points higher than the priority on the targets (as per clinical procedure and recommended by Varian) used in conjunction with a tuning ring structure

to minimize dose to OARs and normal brain. The tuning ring was defined with a 4 cm outer margin and 1 cm inner margin from the outer boundary of the PTV. Dose objectives to OARs were used as needed to further limit dose to OARs. Standard arc geometry as shown in Table 9 was used in all VMAT plans.

4.4.9 Plan Normalization and Evaluation

In-house dose evaluation software was generated which optimizes the DCT-DCA and FC-DCA plans. This was necessitated by the fact that generating a plan sum in Eclipse involving 175 individual plans (one for each control point) was not feasible. The purpose of this software was to analyze dose matrices using patient contour structures and generate dose-volume histograms (DVH) using similar methodology as conducted in Eclipse. The patient plan files, structure sets, and dose matrices from a number of previously planned patients were analyzed to validate the system (data not shown). Each exported dose matrix was super-sampled by a factor of five in all dimensions, and each dose slice was truncated using a binary mask generated from the patient structure contours at each slice. The voxels inside the mask were then condensed to generate DVHs and compared to the structure DVHs as calculated in Eclipse.

To ensure comparable target coverage, all plans in this study were normalized to have the same coverage: the 90% isodose (prescription isodose) to cover 99.5% of every target volume. In all non-VMAT plans, the MU weight was different for each arc, but consistent from control point to control point within the same arc (i.e. constant MU/control point within one arc).

Each DCT-DCA plan was calculated with 175 fields, one for each control point in the plan, at a resolution of five degrees of gantry motion per control point. Each of these dose matrices were individually analyzed and masked, and the sum of these voxels, once weighted according to an in-house MU optimization method (outlined in Section 4.4.10), was combined into a total matrix and analyzed with the same method as the individual dose matrices. The FC-DCA plans were generated using the same methodology, but with a fixed collimator angle selected for each of the arcs and each arc having a different collimator angle.

4.4.10 Arc Monitor Unit Optimization

An arc-weight optimization algorithm was developed in-house in which the objective function was based on: minimizing the separation of the normalization points (V99.5%) in the DVH of any target to the prescription dose, minimizing the maximum dose to the target, and minimizing maximum dose to OARs. DVHs were generated from the sum of the dose matrices calculated for each individual control point of the plan. Final beam weights were selected based on a solution found via objective function minimization by SA where an arc was allowed to vary with relative values spanning one order of magnitude. This optimization algorithm was used for FC-DCA and DCT-DCA plans.

4.5 RESULTS

4.5.1 Validation with Test Cases

In an axial arc, two spheres located on the cranial-caudal axis, as described in Section 4.4.2, will be optimally fit with an MLC when the collimator angle remains static

at 0º throughout the arc. Figure 36 displays a profile of whitespace for a BEV across all collimator angles for control point 180. The same type of measurement shown in Figure 37 was performed at every control point (1° resolution) for the entire coplanar arc; the resulting whitespace map is shown in Figure 37.

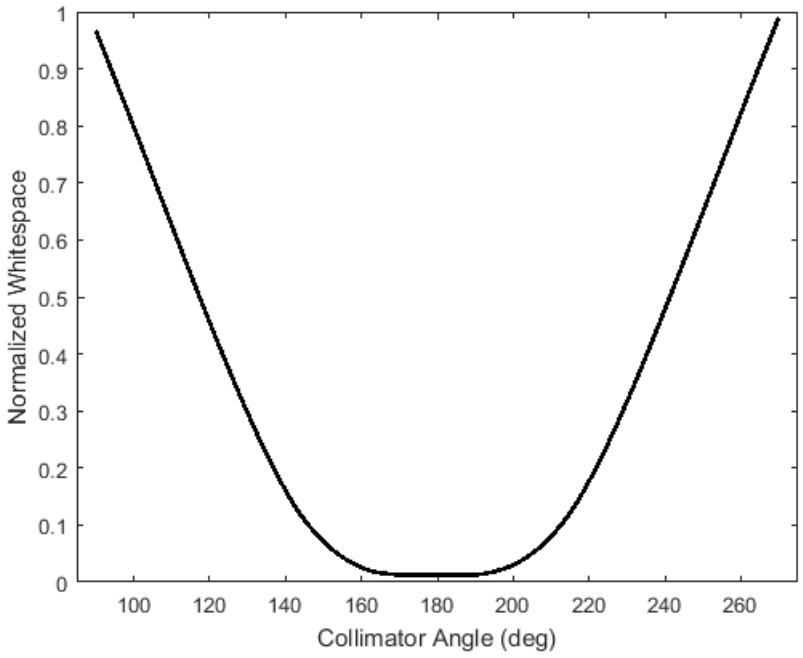

Figure 36: Normalized whitespace profile as measured using Equation 46. The measurement was made with a test case of two identical 2 cm PTVs arranged in a cranial-caudal arrangement, 3 cm apart, with a centrally located isocentre. The BEV shown was projected from $\theta_{CH} = 0^{o}$ and $\theta_{GA} = 0^{o}$ (e.g. control point 180) (Varian IEC).

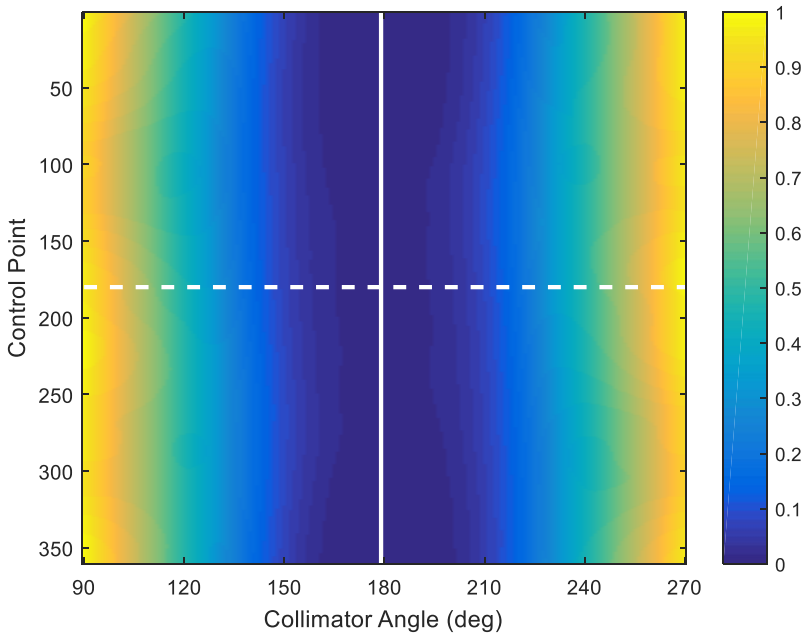

Figure 37: The whitespace map generated from Equation 46 for a two PTV test patient with the same orientation as description in Figure 36. The solid white line indicates the collimator angle that corresponds to the minimum total accrued whitespace across the entire map, and the dashed white line indicates the profile shown in Figure 36.

To utilize the information presented in the normalized whitespace map of Figure 37, the total accrued whitespace as a result of choosing every possible collimator angle was compared, and the minimum accrued whitespace trajectory was determined to be 180^{o} collimator angle, as predicted in the definition of the artificial anatomy. This corresponds to an MLC geometry in which the MLC leaves have the highest capability of shielding the normal tissue between the generated targets. Similar studies were also performed for spheres co-located on the anterior-posterior axis and the left-right and the algorithm performed correctly (data not shown) with results as predicted.

4.5.2 Correlation of Whitespace and Dose

Figure 38 illustrates the data corresponding to the methodology described in Section 4.4.3. The mean dose to the volume bounded by the outer edges of the target volumes, minus the targets themselves, is strongly correlated with integrated whitespace ($R^2 = 0.90$). This normal tissue is at high risk for incidental exposure in the course of treatment of the targets. This indicates that whitespace minimization may result in significant reductions in normal tissue dose under certain circumstances - a result that seems reasonable for DCA cases in particular. It should be noted that these angles span the total quality of whitespace available on the map. The FC-DCA angle used would correspond to the highest quality whitespace seen here. Further evaluation will be required to see if reductions in normal tissue doses are similarly achieved during VMAT treatment deliveries with optimized collimator angles.

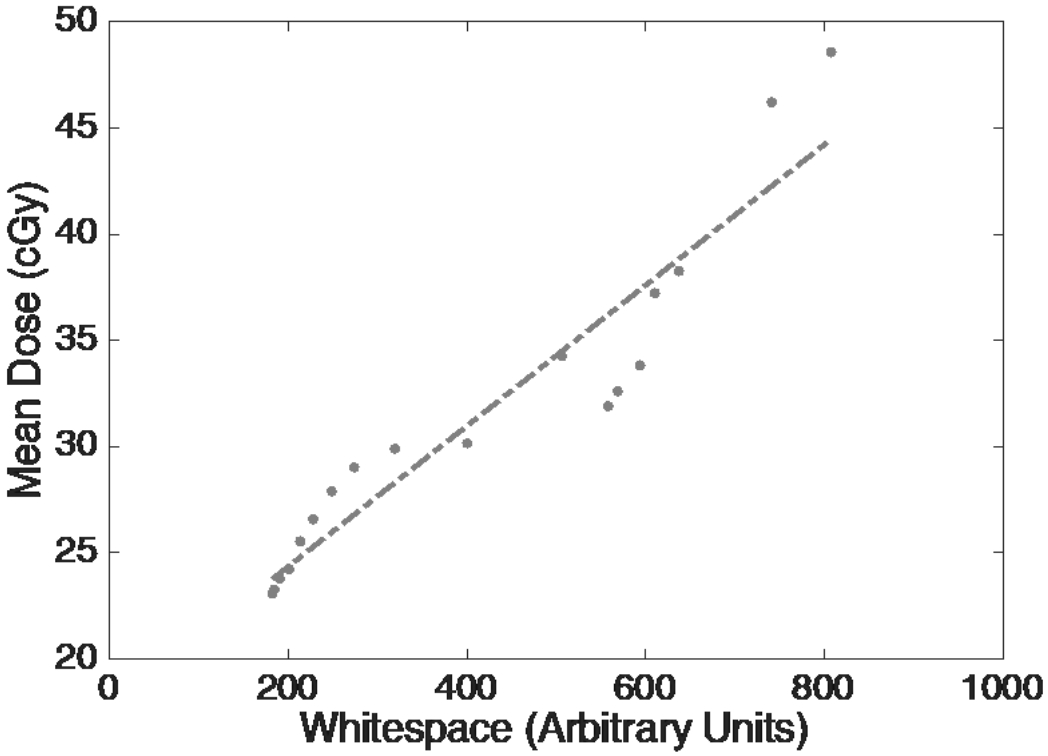

Figure 38: A plot of mean dose to normal tissue bounded by the outer edges of each of the target volumes, subtract the target volumes themselves, with the whitespace amount present in the treatment arc.

4.5.3 Clinical Cases

Twelve cases (two clinically treated patients & ten artificial target plans) were generated with three-targets, and five cases with four-targets (all artificial target plans). All targets were treated to 24 Gy prescribed to the 90% isodose. Three plans were generated for all seventeen cases: DCT-DCA, FC-DCA, and VMAT (as outlined in Sections 4.4.6, 4.4.7, and 4.4.8, respectively). All error bars in the following figures are standard error of the means. Figure 39 shows the mean total plan monitor units across all plans for the three and four target cases. The MU efficiency increase (decrease in MUs) comparing VMAT to DCT is 43.4% and 49.7 % for the three and four target cases,

respectively. When comparing VMAT to FC the gains are 43.2% and 49.7 % for the three and four target cases, respectively.

Figure 40 shows the mean clinically relevant V12Gy across all plans for the three and four target cases, respectively. The decrease in dose to V12Gy comparing VMAT to DCT is 2.9 cm^3 and 1.2 cm^3 for the three and four target cases, respectively, and 2.9 cm^3 and -0.8 cm^3 comparing VMAT to FC for the three and four target cases, respectively.

Figures 41 and 43 show the mean maximum dose to relevant OARs across all plans for the three and four target cases, respectively. None of the OAR doses reached statistical significance in comparing between any of the techniques, suggesting the quality of OAR sparing is comparable to that of VMAT. Statistical significance between plans for each OAR was tested using the Wilcoxon rank sum test, with the results summarized in Table 10.

Figures 42 and 44 show the mean subtraction of normal brain DVHs for DCT from VMAT and DCT from FC across all plans for the three and four target cases, respectively. For each test case, the DCT-DCA DVH was subtracted from the corresponding DVH from one of the other techniques (e.g. VMAT or FC-DCA). The lines shown in Figures 42 and 44 represent the average of this subtraction operation across all test cases (for the three-target or four-target cases, respectively). The differences between DCT-DCA and FC-DCA for three target cases is very small, and the current data indicate that the advantage is dose-level-specific for four target cases (though it is significantly less pronounced than the difference between DCT-DCA and VMAT in the dose levels below V12Gy).

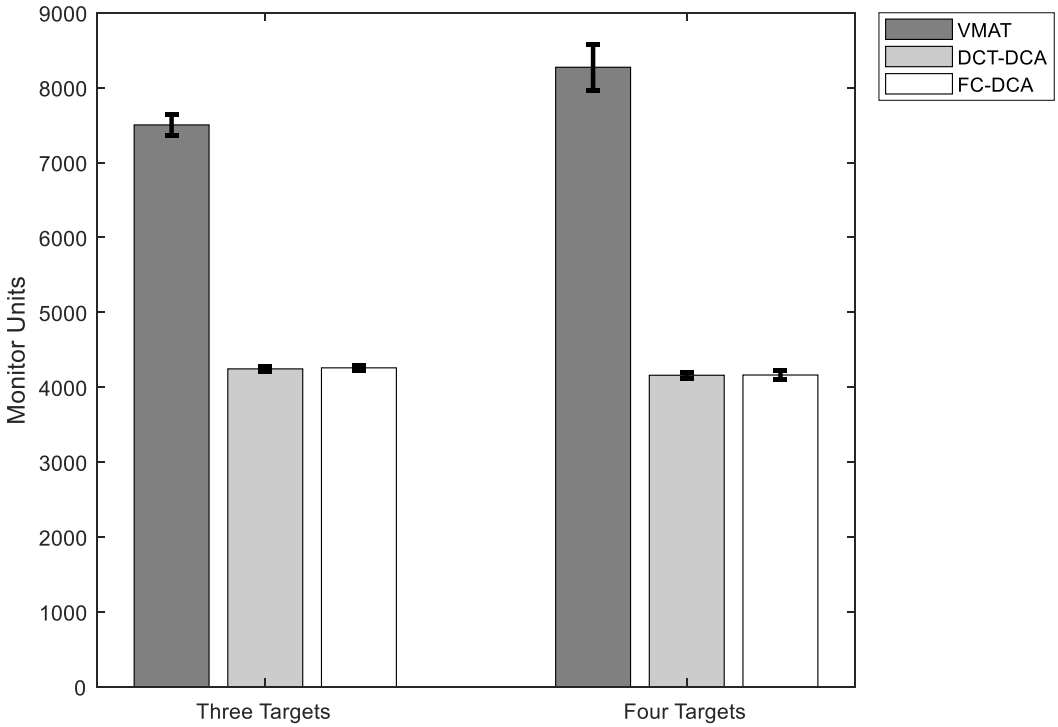

Figure 39: Mean total plan monitor units across all plans generated with three (n =12) and four targets (n =5).

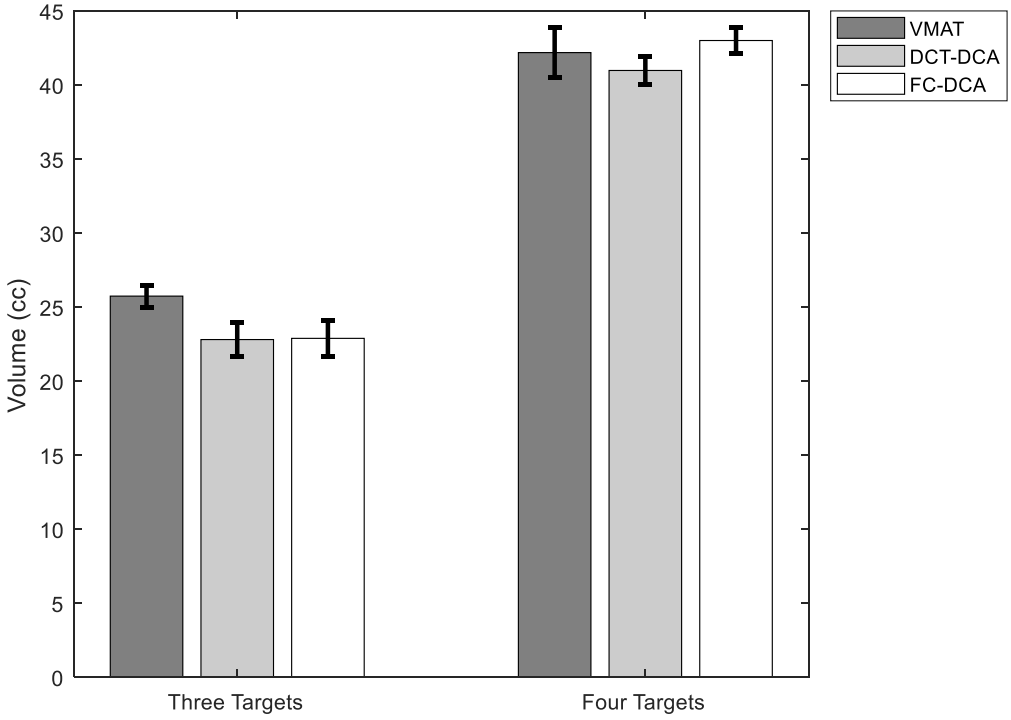

Figure 40: Mean V12Gy across all plans generated with three (n =12) and four targets (n =5).

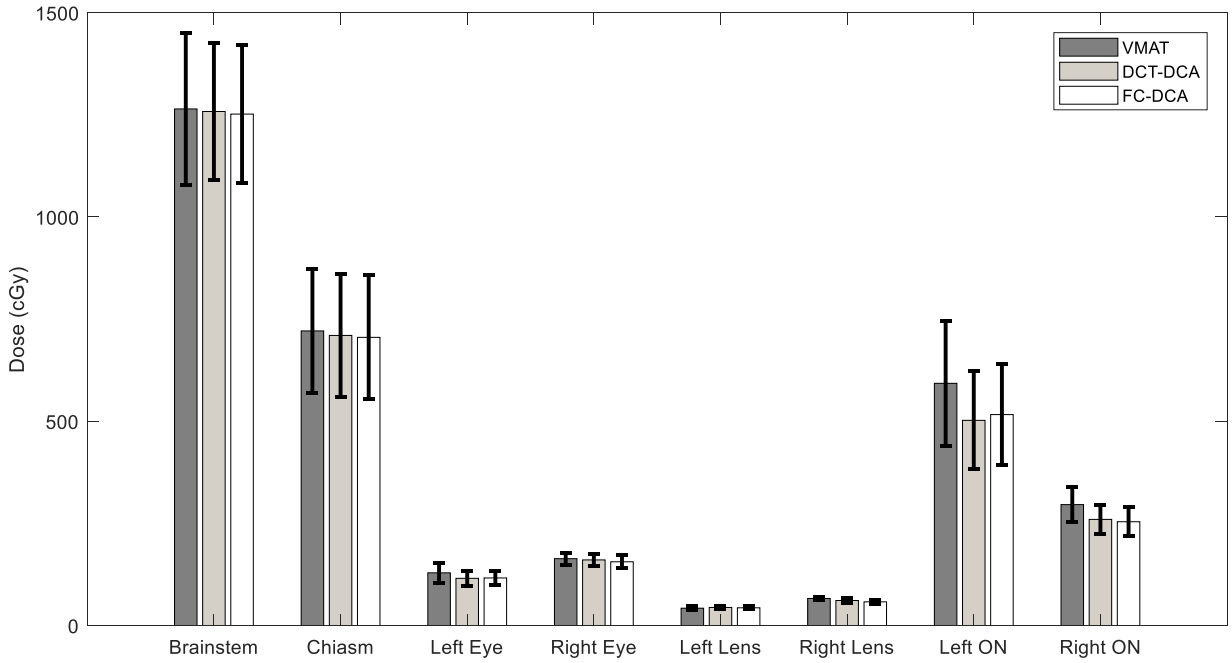

Figure 41: Mean maximum dose to organs-at-risk across all plans generated with three target volumes (n = 12). Optic nerve is represented by ON.

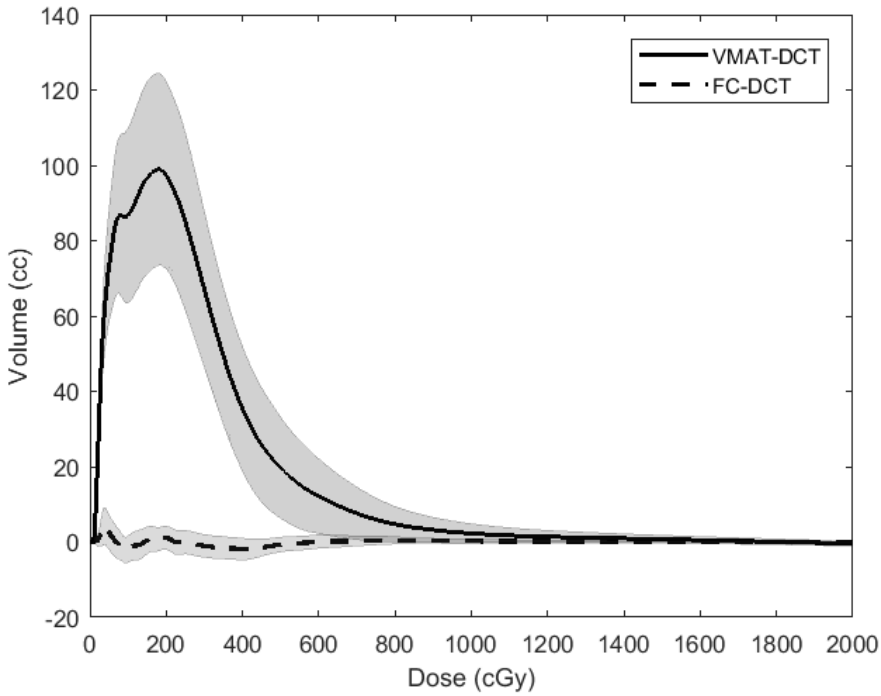

Figure 42: Mean normal brain DVH subtracted between 0 and 20 Gy. The solid line indicates the mean of VMAT subtract DCT across all three target plans, and the dashed line indicates the FC subtract DCT across all three target plans. The shaded region indicates the uncertainty calculated as standard error.

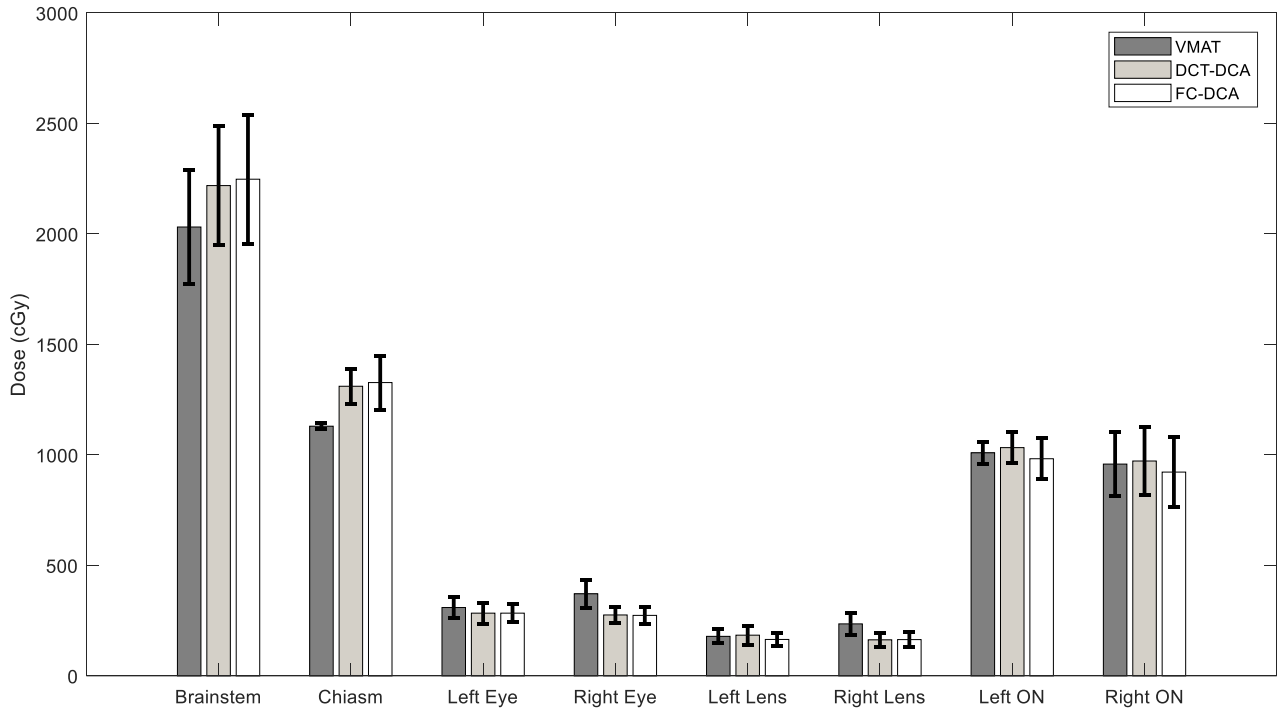

Figure 43: Mean maximum dose to organs-at-risk across all plans generated with four target volumes (n = 5). Optic nerve is represented by ON.

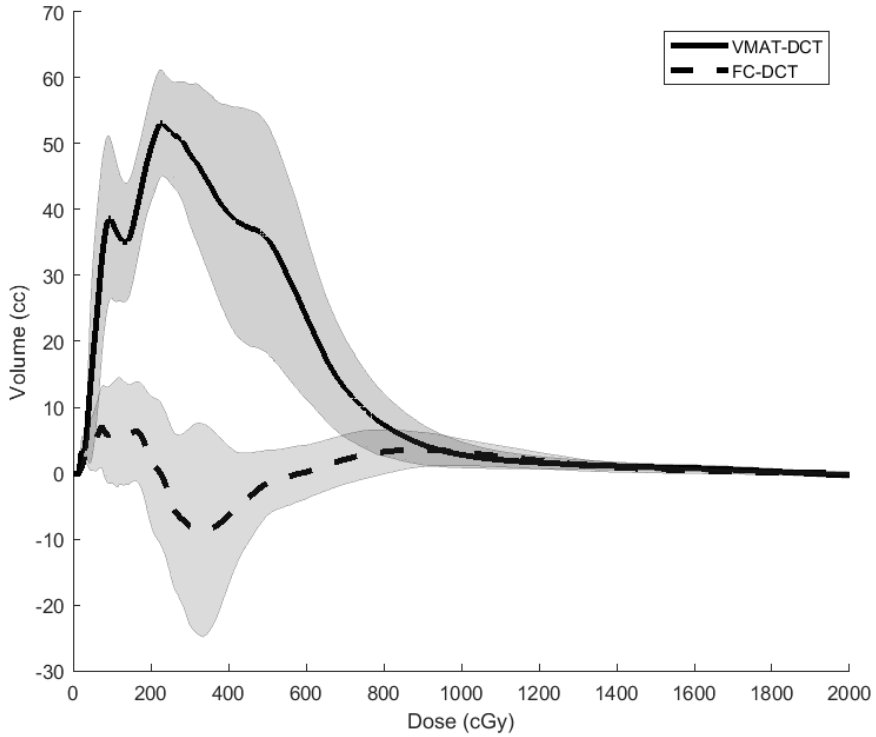

Figure 44: Mean normal brain DVH subtracted between 0 and 20 Gy. The solid line indicates the mean of VMAT subtract DCT across all four target plans, and the dashed line indicates the FC subtract DCT across all four target plans. The shaded region indicates the uncertainty calculated as standard error

Table 10: P-values as calculated by Wilcoxon rank sum computed using MATLAB. Statistical significance above 95% ($p < 0.01$) is highlighted with an *.

Three Target					Four Target			
	VMAT vs DCT	VMAT vs FC	DCT vs FC			VMAT vs DCT	VMAT vs FC	DCT vs FC
MU	<0.00001*	<0.00001*	1		MU	0.0079*	0.0079*	1
V12Gy	0.069	0.0999	1		V12Gy	0.222	1	0.151
Brainstem	1	1	0.885		Brainstem	0.31	0.31	0.841
Chiasm	0.977	0.795	0.977		Chiasm	0.0556	0.151	0.841
Left Eye	0.751	0.665	0.863		Left Eye	0.548	0.421	1
Right Eye	0.84	0.795	0.708		Right Eye	0.31	0.31	0.841
Left Lens	0.908	0.885	0.977		Left lens	1	0.691	0.841
Right Lens	0.273	0.126	0.751		Right Lens	0.421	0.31	1
Left ON	0.544	0.5834	0.751		Left ON	1	1	1
Right ON	0.403	0.371	0.885		Right ON	1	1	1

4.6 DISCUSSION

The potential benefits of dynamic collimator trajectories are threefold:

1. Increased treatment delivery efficiency.
2. Normal tissue dose comparable to VMAT.
3. Elimination of manual collimator angle selection.

With respect to the first point, evidence of improved treatment delivery efficiency is provided in Section 4.5.3. When compared to state-of-the-art methods of multiple-metastases treatment planning, such as that offered by VMAT, the optimized collimator trajectory treatment offers an increased efficiency in MUs of up to 49.7% ($p < 0.01$). This difference can largely be attributed to the method with which each approach treats targets. In VMAT planning, apertures used in treatment frequently involve collimation to small fractions of the total target projection which aim to limit the dose to healthy tissue while treating target volumes. This in turn forces more monitor units to be delivered to meet prescription dose levels. It does not make use of potential efficiencies by attempting to keep the aperture in a conformal setting as much as possible. The simultaneous

treatment of all targets in the DCT-DCA and FC-DCA treatments results in a significant reduction in MUs when compared to VMAT. Following arc-weight optimization for the DCT-DCA and FC-DCA plans, the MU for these two techniques were, on average very similar (Figure 39). When put in the context of SRS or SBRT treatments (i.e. high dose, high dose gradient treatments), significant reductions of beam-on time confer the advantage of reducing the time available for intrafraction motion. Although certainly secondary considerations, long beam-on times also raise questions about leakage dose, with implications for both radiation safety (e.g. bunker wall thickness) [91, 92] and secondary malignancies in patients [90, 93, 94]. Additionally, extended treatment times may contribute to the repair of sub-lethal damage within targeted tissues [80].

With respect to the comparable normal tissue dose (point 2), our data indicate that dynamic conformal arc plans had normal tissue values comparable to that of the highly modulated VMAT plans. Even in cases with four targets all within 1 cm of an OAR, the optimized DCA treatments did not significantly deviate from VMAT OAR doses. In cases with physical abutment or overlap between OAR and target, the conformal aperture used in FC-DCA or DCT-DCA could be modified to attempt additional sparing to the abutting OAR. This could be conducted by introducing additional value to the weighting factor w_3 in the whitespace cost equation. Differences in the V12Gy metric were not statistically different in any of the comparisons. A 2010 study by Blonigen et al. [96] indicates that the best predictors of radionecrosis for linear accelerator-based SRS is the V8 Gy to V16 Gy. As illustrated in Figures 42 and 44, there is dosimetric advantage of the DCT plans over the VMAT plans in both the three and four targets cases at the V8.5Gy ~ V10 Gy (not statistically significant). Below V8.5Gy, larger advantages were

observed when comparing the DCT-DCA plans to VMAT. For the three target cases, the difference was statistically significant between 0.1 and 8.5 Gy ($p < 0.05$). While the four target cases showed similar trends, the small sample size ($n = 5$) and reduced magnitude were insufficient to achieve statistical significance. There were no significant differences between DCT-DCA and FC-DCA plans at any 475 dose levels for either three or four target cases. This information may still be of clinical significance given the fact that oligometastases treatments delivered in multiple plans or patient retreatments could necessitate reduction of normal brain dose at all dose levels to ensure that the cumulative effects at the V12Gy level are kept as low as possible. The isodose contour for an initial plan could be imported to a secondary treatment plan and treated as an OAR to avoid irradiating the same volume.

Interestingly, in the cases studied, normal tissue doses were not significantly reduced in the DCT-DCA plans relative to the FC-DCA plans. With an increase in the number of targets in the treatment and with increased separation of the targets, we expect the normal tissue sparing advantage of DCT over FC to increase, as the incidence of zero whitespace collimation options generally decreases with increases in target number, and the magnitude of the area increases with increased separation of targets. This trend begins to appear in Figure 40 where the V12Gy for DCT and FC is approximately equivalent for three targets ($p = 1$) and lower for DCT ($p = 0.151$) for four targets. Although we did not study non-optimal fixed collimator DCA plans in this work, the data presented in Figure 38 suggest that deviation from an optimal collimator position will lead, at a minimum, to higher normal brain doses. The degree of sensitivity to non-optimal collimator angle will likely depend on patient-specific anatomy, number of targets treated, and spatial

orientation of those targets. We recognize that in this, as in any, planning study in which different planning techniques are compared, there is always the potential that different planners would achieve different results. In this study, all VMAT plans were generated by two experienced medical physicists, one of whom was an experienced SRS VMAT planner who also reviewed all VMAT plans. Further efforts to reduce normal tissue doses may have yielded dosimetric benefit but would likely have increased the treatment monitor units.

With respect to the selection of fixed collimator angles (point 3), the clinical process is typically manual and may be based on planner experience, trial-and-error, or departmental procedure. Regardless of how it is chosen, it is highly unlikely that the selected angle will match the one chosen with a robust optimization algorithm. As such, this algorithm has current clinical utility in aiding fixed collimator angle selection for DCA or VMAT plans, as manual collimator angle optimization would be subjective and a potentially non-optimal process. Using an algorithm such as the one presented here would remove this step from the planning process and provide optimized fixed collimation throughout the treatment. Current methods of generating optimal collimator angle identify shortest dimension of BEV target [47], a method susceptible to non-optimal conditions, and inferior to the method offered here. Although based on a small number of cases, these data indicate that the proposed algorithm can generate significant gains in efficiency.

The collimator trajectory indicated in Figure 35 was generated via the bi-directional gradient method. By measuring, for each control point, the collimator angle with the minimum value of whitespace and generating a discontinuous trajectory, we can

establish a benchmark for the minimum achievable integrated whitespace (i.e. - without consideration of collimator motion constraints between control points). Comparing the dynamic trajectory generated for Figure 35 via the bi-directional gradient to this lower bound, we found an increase in whitespace of only 2%, while the best fixed collimator solution increases whitespace by 92%. While other methods exist for determining paths of least resistance, the gains from implementation of these methods could only serve to further reduce the minor differences between the bi-directional gradient search and the lowest possible solution, which may not have clinical relevance.

In this work, we limited the allowable collimator motion to ± 3° between control points. Currently, this constraint is applied only to ensure dosimetric accuracy is maintained between calculated and delivered fields and the axis position transitions inherent in LINAC control point delivery. This restriction additionally ensures the treatment will not incur an increase in time to accommodate motion on the collimator rotation axis. With removal of the restriction to the collimator trajectory, the maximum dose to six out of eight OARs for the most challenging four-target case in this study were reduced by an average of 33.78 cGy (18.2 - 78.2 cGy). For the right optic nerve, the dose increased by 27.0 cGy. This increase in sparing comes at a detriment to deliverability as the treatment time would be extended in order to accommodate the required collimator rotation. Through experiments, it may be found that ± 3° is too restrictive; in which case, the degree of flexibility of our method may be expanded.

In the current work, we focused on the treatment of three and four lesions simultaneously. Treatment of fewer lesions in an SRS setting would likely not offer any improvements in efficiency, unless the targets have substantial complexity, although

normal tissue doses may still see a decrease in dose even with two targets, as the algorithm will select optimal collimator angles to minimize dose between the PTVs. In the case of a single target with a complex shape, such as a meningioma or an arteriovenous malformation, the advantage of lower normal tissue doses as a result of dynamic collimator trajectories is a possibility. Additionally, through the cataloging nature of this method, it could degenerate into a fixed collimator angle solution if there were no benefit to dynamic collimator motions.

4.7 CONCLUSION

Dynamic collimator trajectories have the potential to improve radiotherapy treatment deliveries through decreased monitor units and, consequently, delivery time. Additionally, in DCA treatments, the minimization of whitespace from a BEV perspective reduces dose to normal tissue in close proximity to the target volumes. This study has demonstrated that the whitespace metric correlates well with mean dose to proximal normal tissue.

Analysis of our results shows that optimized collimator trajectories were found to produce a reduction in monitor units of up to 49% compared to the state-of-the-art VMAT technique.

Increased efficiency, normal tissue doses comparable to VMAT, and automated collimator angle optimization are major benefits of this algorithm, especially in the treatment of multiple cranial metastases. The clinical implementation of dynamic collimator trajectories in arc therapies, such as VMAT or DCA, could be introduced by

linear accelerator manufacturers with little cause for concern from a safety point of view since collimator motions have minimal impact on the profile of the machine.

CHAPTER 5 MANUSCRIPT 3: INTRA-ARC BINARY COLLIMATION ALGORITHM FOR THE OPTIMIZATION OF STEREOTACTIC RADIOTHERAPY

5.1 PROLOGUE

This manuscript is the second foray into dynamic collimation techniques and is an expansion on the methodology of Chapter 4 to address the ability to accomplish demanding prescription doses in DCA techniques with dynamic collimation.

A novel method of dose optimization was designed to define a schedule and quota of subsets of the total targets to be treated at a given control point. By allowing every target at every control point to be in one of two binary states, treated conformally or completely shielded, the optimal pattern of targets to be treated with equal weighting of every control point was designed via SA. Collimation to desired targets with the MLC was then employed with dynamic collimator rotation in order to minimize the discrepancy between approximating perfect collimation to all targets and fitting all targets with an MLC.

The monitor unit distribution (MUD) (the relative distribution of dose on a control point specific distribution) was then defined for the control points and the plan was imported into the Eclipse treatment planning system for confirmation of dosimetry. The plans are compared with expert-planned VMAT plans for dosimetric evaluation.

Publication: *MacDonald, R. Lee, Christopher G. Thomas, Lucy Ward, and Alasdair Syme. "Intra-Arc Binary Collimation Algorithm for the Optimization of Stereotactic Radiotherapy Treatment of Multiple Metastases with Multiple Prescriptions." Medical Physics (Submitted January 1, 2018): (under review).*

5.2 ABSTRACT

Purpose: To design and implement a novel treatment planning algorithm based on a modification of dynamic conformal arc (DCA) therapy for the treatment of multiple cranial metastases with variable prescription doses.

Methods: A workflow was developed in which separate dose matrices were calculated for each target at each control point (i.e. the MLC was fit conformally to that single target). A cost function was used to quantify the relative contributions of each dose matrix in the plan to the overall plan objectives. Simulated annealing was used to allow for the inclusion or exclusion of individual dose matrices at each control point. The exclusion of individual targets at a given control point is termed intra-arc binary collimation (iABC) in this work and is accomplished by closing the MLCs over the target for a duration specified by simulated annealing optimization. Dynamic collimator motions were employed to minimize the variation between the idealized dose matrices (i.e. perfectly collimated targets) and actual dose matrices (i.e. MLC apertures that include quantities of non-target tissue due to the relative orientations of targets in the field). An additional simulated annealing optimization was performed to weight the relative contributions of dose at each control point (referred to as the monitor unit distribution (MUD)) to improve compliance with plan objectives. The algorithm was tested on seven previously-treated multiple metastases patients and plans were compared to the clinically-treated VMAT plans.

Results: Treatment plans generated with iABC used an average of 3044 (37%) fewer MU in the total plan than VMAT plans ($p = 0.026$). All normal tissue metrics for all plans and all patients were clinically acceptable. There were no statistically significant differences in any normal tissue dose metrics. Normalized prescription target coverage

accuracy, after prescription coverage was obtained applied for all targets, was 4.0% better on average for VMAT plans when compared to iABC ($p = 0.016$), and 14.8% better on average for iABC when compared to optimized DCA ($p = 0.041$).

Conclusion: A novel method of aperture and dose distribution design was developed to significantly increase the MU efficiency of single isocentre treatment of multiple metastases with variable prescription doses when compared to VMAT, and which improves target coverage accuracy significantly when compared to optimized DCA. By applying a DCA approach to subsets of targets across control points, a hybrid method of treatment delivery was developed that combines the efficiency of dynamic conformal treatments and the dosimetric flexibility of VMAT.

5.3 INTRODUCTION

Treatment of multiple cranial metastases with variable prescription doses in a single isocentric treatment is a complex optimization task. Compared to other treatment techniques that use multiple isocentres, single isocenter treatments are often significantly more efficient (i.e. the patient spends less time on the bed). From a patient population perspective, this increase in efficiency could lead to greater patient throughput on a treatment unit. From the patient-specific perspective, increased efficiency may translate into reduced treatment times and thus reduced potential for intrafraction motion.

The optimization of radiation dose distributions through the intensity modulation of rotating fields in order to achieve improved target conformity has been under investigation for 30 years [44]. Highly conformal treatment plans, characterized by rapid dose fall off outside of target volumes, are often delivered with VMAT or IMRT. Early

systems of aperture and fluence optimization divide the beam's-eye-view (BEV) of the tumor into a series of finite size pencil beams, and ideal distributions were created via optimally weighted beams. Leaf-sequence optimizers then translate the distribution into deliverable sequences [97]. The resultant plans often require large quantities of monitor units (MU) to approximate these dose distributions. Improvements in efficiency were made by implementing automated systems to directly optimize the shape and weight of the apertures that incorporate the machine dependent delivery constraints that were previously conducted in a separate leaf-sequencing step. This simultaneous optimization allows user-specified control over the complexity of treatment delivery through plan objective weighting, resulting in significant reduction in the number of beam segments and the number of MU [37].

Dynamic conformal arc (DCA) treatments present two advantages over VMAT: dosimetric robustness and a decrease in the total required MU for treatment. The larger apertures used in DCA planning have been shown to increase plan MU efficiency (decrease in MUs) and decrease susceptibility to multi-leaf collimator (MLC) errors compared to highly complex plans [99]. Additionally, the use of conformal apertures increases the average target dose per MU compared to a typical VMAT aperture, which irradiates a subset of target voxels at any one time, thus allowing DCA to use substantially fewer MU. A limitation of DCA, however, is the inability to create complex fluence or aperture modulation patterns to meet demanding dosimetric constraints. In the

case of variable prescription doses applied in multiple metastases treatments, DCA planning is less likely to accomplish accurate coverage of all targets.

Binary collimation, as implemented in TomoTherapy (Accuray Inc., Sunnyvale, CA, USA), uses a tungsten leaf MLC to divide a fan beam of radiation into smaller segments (beamlets). A beamlet at any point in the treatment is then "open" if its associated leaf is retracted, or "closed" if the leaf is extended across the fan [101]. Our research introduces a variation on this principle by offering two states at any control point for a target in the treatment field: (1) MLCs conformally fit to the target, or (2) entirely shielding the target. This concept differs from other conformal techniques, such as that employed in Brainlab's Multiple Metastases Element (MME) (Brainlab AG, Munich, Germany), which offers treatment of a subset of targets within a given arc. MME selects the optimal number of arcs based on the number and location of the targets but does not vary which targets are treated between control points within an arc [98].

This study aims to design a system that uses simulated annealing to optimize the collimation of subsets of targets at specified control points, through a process defined as intra-arc binary collimation (iABC), along with control point-specific MU weighting, to achieve prescription target coverage and normal tissue sparing, where this would be normally accomplished through MLC modulation in a VMAT plan.

5.4 METHODS

At each control point, the system aims to optimize the number of targets treated, the rotation angle of the collimator, the MLC positions, and the number of MU delivered. A flowchart of this optimization is shown in Figure 45.

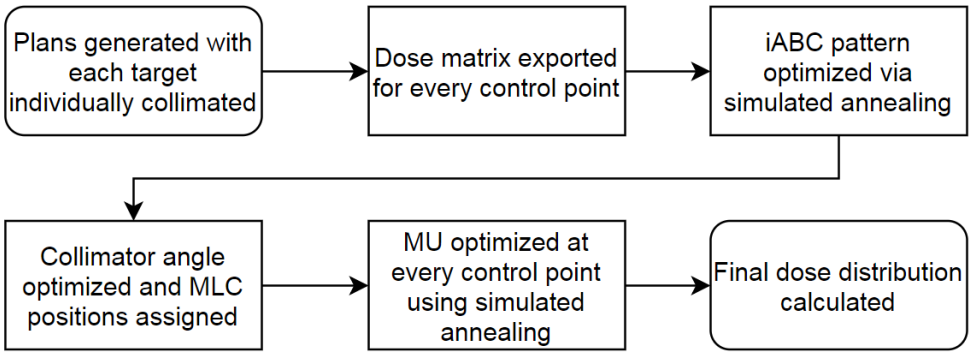

Figure 45: A flowchart of the methodology for iABC treatment planning process.

5.4.1 Individual Target Dose Matrix Calculation

A conventional clinical stereotactic four arc treatment planning template [45] (one 360° coplanar arc, one 155° vertex arc, and two 180° arcs at couch angles 315° and 45°) was divided into 175 equally spaced control points (1 control point every 5° of gantry travel). A treatment plan was then created for each control point with each PTV individually collimated with a 1 mm margin (single isocentre for all PTVs) and a dose matrix for every CP was generated in Eclipse (v.11) for a 6X-FFF beam on a Varian TrueBeam STx accelerator with an HD120 MLC (Varian Medical Systems, Inc., Palo Alto, USA). CT slice thickness was 1.25 mm and the dose calculation grid size was 1.5 mm. Each dose matrix was then analyzed using in-house MATLAB (R2017b,

MathWorks, Inc., Natick, MA, USA) software to extract the voxels within the following: brainstem, optic chiasm, eyes, lenses, and optic nerves. The doses from each control point dose matrix for every structure were indexed and summed over the entire treatment plan to generate a dose total for each structure.

5.4.2 Plan Quality Objective Function

A novel objective function (OF) was designed for this study to quantify relative plan quality, and a simulation system was developed to minimize this OF in order to optimize plan quality. A series of penalty metrics (M) is calculated using a linear-quadratic function that is intended to be more appropriate for typical SRS planning constraints that are often focused primarily on maximum doses to normal tissues or minimum coverage of a target. The value of M was non-zero for OARs for any non-zero dose. For targets, M takes on a non-zero value for any deviation from a perfect DVH (i.e. all target voxels receive exactly the prescription dose). For OARs, the value of M increases linearly as the maximum OAR dose increases from zero. Once the maximum dose reaches a user-defined warning value, denoted as v_{warn}, the value of M begins to increase quadratically. An arbitrary value of 100 for M was defined at the value of the clinical constraint (or limit of acceptability), denoted here as v_{must} (see Figure 2). A similar approach was adopted for the targets, however, the parameters of interest were expanded to include the dose received by 99% of the target volume (D99%), the maximum target dose and the volume of the target receiving the prescription dose (VRx). For the normal brain dose objective, the v_{must} value was established based on the V12Gy value for the total plan dose in the first iteration (prior to any optimization) and is defined in Table 11 as $v_{initial}$. The input values for the variables in the OF for each dose metric are

defined in Table 11 based on established clinical constraints [18]. A p_{warn} value of 20 was used for all metrics to encourage a shallow linear function, providing a steep quadratic function.

Table 11: The parameters used for the iABC planning objectives to generate the plans used in this comparison. $V_{initial}$ here corresponds to the initial value of V12Gy from the plan total prior to any optimization.

	Metric	v_{warn}	p_{warn}	v_{must}	p_{warn}
Target Metrics	**$D_{99\%}$**	Rx + 0.5 Gy or Rx – 0.5 Gy	20	Rx + 1.0 Gy or Rx – 1.0 Gy	100
	Target Maximum	135 % of Rx	20	160 % of Rx	100
	V_{Rx}	98.9 % or 99.1%	20	98.8 % or 99.2 %	100
Normal Tissue Metrics	**OAR Maximum**	0.7 × v_{must}	20	8 Gy	100
	V12Gy	0.7 × v_{must}	20	$V_{initial}$	100

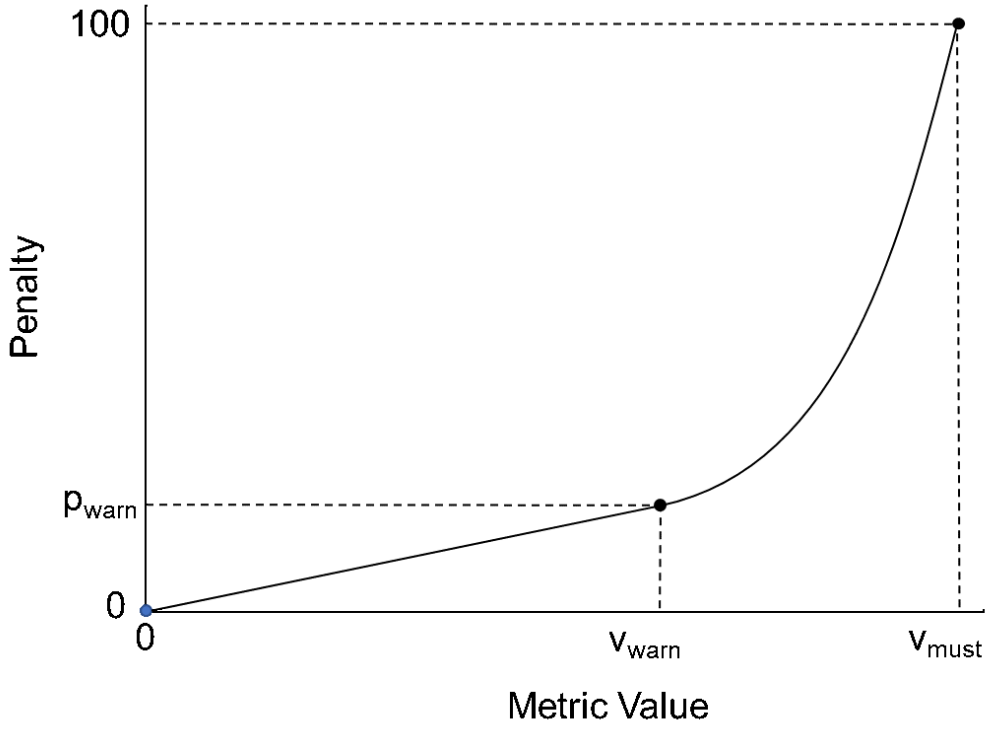

Figure 46: Generalized penalty function for all metrics used in the calculation of the objective function.

The OF for an individual target (OF_{PTVi}) was a quadrature addition of the target metrics (M_i), and the total OF for all targets (OF_{PTV}) was a linear sum of the individual OF_{PTVi}. The total normal tissue OF (OF_{OAR}) was a linear sum of normal tissue metrics,

one for each OAR. The plan quality objective function (OF_{PLAN}) was the sum of target and normal tissue functions. The equations representing the objective function are represented below in Equations 47 to 51, where M is the penalty at metric value v, k is the number of metrics applied to the i[th] PTV, p is the number of targets, o is the number of OARs:

$$M = \begin{cases} \frac{p_{warn}}{v_{warn}} v, \ if \ \ 0 < v < v_{warn} \\ \frac{100 - p_{warn}}{v_{must} - v_{warn}} [v - v_{warn}]^2 + p_{warn}, \ if \ v \geq v_{warn} \end{cases} \quad (47)$$

$$OF_{PTV\,j} = \sqrt{\sum_{i=1}^{k} M_i^2} \quad (48)$$

$$OF_{PTV} = \sum_{j=1}^{p} OF_{PTV\,j} \quad (49)$$

$$OF_{OAR} = \sum_{i=1}^{o} M_i \quad (50)$$

$$OF_{PLAN} = OF_{PTV} + OF_{OAR} \quad (51)$$

5.4.3 iABC Pattern Optimization

Using the total plan dose obtained in Section 5.4.1, OF_{PLAN} defined in Section 5.4.2 was used as a minimization metric in a simulated annealing procedure to define the intra-arc binary collimation (iABC) pattern. With iABC, each target can either be conformally treated or entirely shielded by the MLC at each control point (CP) (except for any incidental overlap between a treated and a shielded target). At every iteration in the simulation, a new iABC pattern was generated for each CP. The OF_{PLAN} was recalculated and was accepted if it decreased. A larger OF_{PLAN} can be accepted based on a calculated probability of acceptance of worsening solutions, which decays with time [100]. This feature of simulated annealing facilitates a more thorough search of the OF parameter space and reduces the likelihood of becoming trapped in a local minimum in

the solution space. The simulation was conducted with 3000 total iterations to ensure convergence of the objective function. At the end of the simulation, the pattern which returns the minimum OF_{PLAN} was selected, regardless of the iteration at which it occurred.

5.4.4 Collimator Optimization

With the iABC pattern defined in Section 5.4.3, the BEV projection for each control point can be defined based on the targets included at the control point. Using a previously published collimator optimization method [60], the collimator rotation angle was optimized at each control point, generating a dynamic collimator rotation trajectory. The purpose of this optimization is to minimize the presence of non-target anatomy present within the BEV throughout treatment. The collimator trajectory was defined with a mechanical restriction of 3° of collimator rotation for every 1° of gantry rotation.

After collimator rotation optimization, the MLC leaf position was then defined by in-house MATLAB code to conformally fit to the targets defined in the iABC pattern with a 1 mm margin from the PTV.

The optimization of collimator angle also serves to minimize the discrepancy between the idealized dose matrices that were used in the determination of the iABC pattern in 5.4.3 and the real dose matrices that were derived from the actual MLC positions, which may include non-ideal target collimation when opposed leaf pairs are required to conform to more than one target.

5.4.5 Monitor Unit Distribution Optimization

The simulated annealing process described in 5.4.3 was repeated using the field doses to optimize MUs at each CP. At the start of the simulation, all fields had an equal

contribution of MU. The simulation assigned a randomly selected relative normalized value between 0.1 and 3 of an MU to a randomly selected control point, renormalized the doses to meet prescription requirements, recomputed the same OF_{PLAN} outlined in Section 5.4.2, and accepted this new value based on the SA process described in Section 5.4.3. The simulation was conducted with 3000 total iterations to ensure convergence of the objective function. The result of this optimization was a control point specific monitor unit distribution (MUD) aimed at defining the relative contribution of dose at each of the 175 control points (fields in the plan). This distribution was then used to reconstruct the RTPlan DICOM file with optimized monitor units to be imported into Eclipse for evaluation.

5.4.6 Test Patient Planning

Seven multiple metastases patients previously treated at the Nova Scotia Health Authority were anonymized and re-planned with VMAT, optimized DCA, and iABC using consistent planning methods. The optimized DCA plans resulted from identical methodology to the iABC plans (MUD and collimator angle optimization, as described in 5.4.4 and 5.4.5), however all targets were treated at every control point, with the aperture fit conformally with a 1 mm margin from the PTVs. Six patients were treated using single fraction stereotactic radiosurgery (SRS) and one (Test Patient 1) using fractionated stereotactic radiotherapy (SRT). Clinically-assigned prescription values and PTV volumes are shown in Table 12.

All VMAT planning was conducted by one of the authors (L. Ward), a CMD-certified treatment planner with six years of VMAT planning experience. Most of the

VMAT planning required up to four passes through the optimizer to meet OAR and PTV constraints, with adjustments on objectives and priorities on each pass. Automatic normal tissue objective (NTO) was used in all cases, as well as a tuning ring around the PTVs (4 cm outer diameter, 1 cm inner diameter).

All iABC and optimized DCA plans were generated with OF parameters shown in Table 11, without patient-specific customization or repeated optimization. All plans were normalized such that the prescription dose to the coldest target, with reference to its prescription, was covering 99% of said target volume. In this way, all targets were at least 99% covered by their prescription dose and allowed inhomogeneities within target volumes. Metrics were extracted from all plans using MATLAB scripting. The clinically relevant metrics extracted were: total MU, brain volume receiving 12 Gy or greater, conformation number [85] for all targets with the maximum prescription, isodose volume receiving the minimum prescription dose (both raw volume and normalized to VMAT plan volume), dose covering 99% of the target volume normalized to the prescription

dose (target coverage accuracy), and maximum dose delivered to the brainstem, eyes, lenses, optic chiasm, and optic nerves.

Table 12: All target volumes and clinical prescription doses for all targets in the study.

Patient ID	Volume (cm^3)	Prescription Dose (Gy)
Test Patient 1	1.15	25
	1.15	25
	11.83	30
Test Patient 2	5.85	20
	0.48	24
	1.3	24
	0.46	24
Test Patient 3	8.13	20
	13.41	20
	1.59	24
Test Patient 4	2.97	18
	7	15
	1.48	18
Test Patient 5	4.99	18
	8.27	15
	1.35	20
	2.81	18
	2.71	18
Test Patient 6	10.76	18
	4.36	20
	0.63	24
Test Patient 7	6.46	20
	0.18	24
	0.1	24

5.4 RESULTS

5.5.1 iABC Pattern Optimization

Using the OF_{PLAN} described in 5.4.2 and the optimization described in 5.4.3, iABC patterns were designed for all seven patients. The evolution of the value of the OF_{PLAN} as the simulated annealing proceeds is shown in Figure 47. The mean OF_{PLAN}

value for the simulations is seen to reduce by several orders of magnitude before plateauing and converging onto a final value at the end of the simulation.

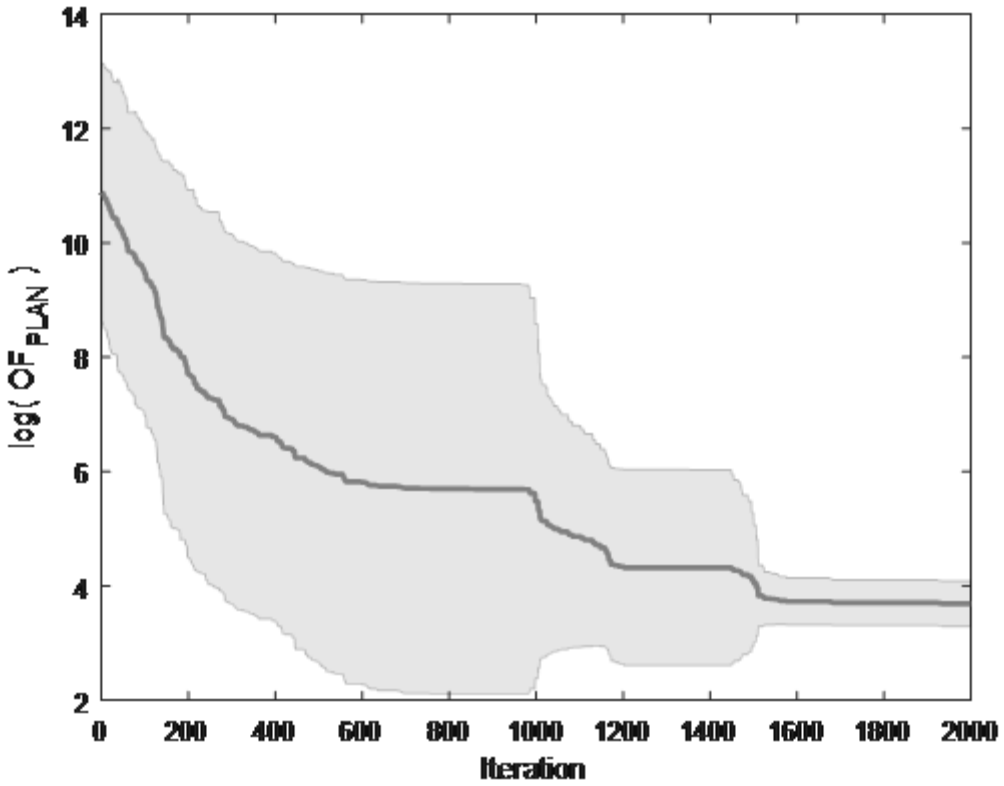

Figure 47: Simulation convergence for iABC pattern assignment averaged across the patient population (n = 7). The solid line indicates the mean value at each iteration, while the shaded area indicates the standard deviation.

5.5.2 Monitor Unit Optimization

Using the OF_{PLAN} described in 5.4.2 and the optimization described in 5.4.5, MUDs were designed for all iABC plans. To illustrate the advantages of iABC in terms of the OF_{PLAN}, the MUD optimization was also applied to the optimized DCA plans. At both initial iterations and final iterations, iABC produced OF_{PLAN} values that were several orders of magnitude smaller than optimized DCA. In general, as shown in Figure 48, this

optimization step requires fewer iterations to converge on a final solution than the iABC optimization.

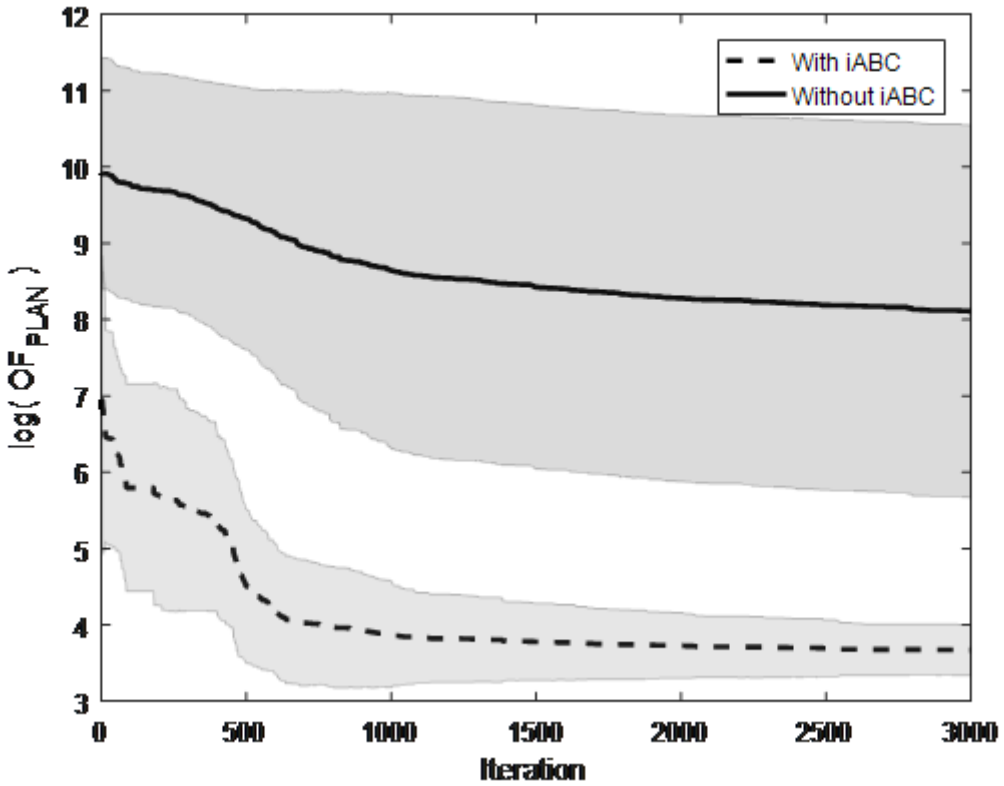

Figure 48: Simulation convergence for MUD assignment with and without the implementation of iABC method averaged across the patient population (n = 7). The solid line and dashed line indicates the mean values at each iteration. The shaded area indicates the standard deviations for each curve.

5.5.3 Dynamic Collimator Optimization

As described in Section 5.4.4, the collimator angle was optimized through the navigation of a 2D cost function map quantifying the area of non-target anatomy present in the BEV. Figure 49A illustrates collimator optimization without the use of iABC (i.e. the collimator trajectory applied to the optimized DCA plans), and Figure 49B shows the collimator cost function value with iABC included. By removing targets from the BEV through iABC, ideal target collimation becomes more common among collimator angles,

reducing the overall cost in rows of the map. This modification to the cost function map allows for the identification of optimal trajectories not previously available without iABC.

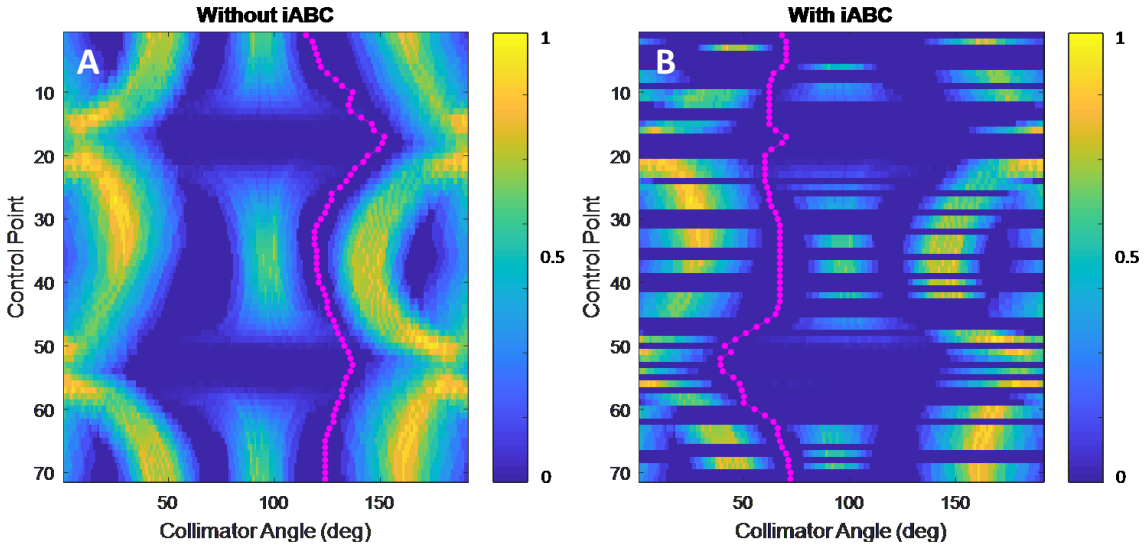

Figure 49: Collimator cost function (whitespace) maps without (A) and with (B) the use of iABC techniques. The color scale is indicative of the non-target anatomy area present in the BEV. The magenta trajectory across the map represents the path of the optimized collimator angles throughout the treatment.

5.5.4 Test Patient Planning

Table 13 is a tabulation of the mean values for all planning metrics extracted from all optimized DCA, iABC, and VMAT plans conducted as described in Section 5.4.6. Salient observations are plotted in Figure 50 as bar plots in order to further illustrate important trends. Statistical significance of differences between planning techniques was evaluated using a Wilcoxon rank-sum analysis in MATLAB.

Table 13: Results of all planning metrics for optimized DCA, iABC, and VMAT plans for all seven multiple metastases cases with multiple prescription doses. ¶ indicates statistical significance ($p<0.05$) between DCA and iABC, § indicates statistical significance between iABC and VMAT, and * indicates statistical significance between DCA and VMAT.

	Optimized DCA			*iABC*			*VMAT*	
Metric	**Mean**	**Standard Deviation**		**Mean**	**Standard Deviation**		**Mean**	**Standard Deviation**
Monitor Units	4248*	234		5181§	377		8225*§	1098
V12 Gy (cm^3)	86.2	14.9		63.0	9.32		54.5	7.20
Inverse van't Riet Conformity Number	1.61	0.31		1.54	0.22		1.34	0.18
Volume of lowest Prescription (cm^3)	43.29	23.58		29.73	12.65		22.85	9.27
Volume of lowest Prescription (normalized to VMAT)	1.88	0.75		1.31	0.29		1.00	0.00
Target Coverage Accuracy	1.202*¶	0.220		1.054¶§	0.054		1.014*§	0.027
Brainstem Max (Gy)	12.8	2.79		11.6	3.1		10.4	2.8
Chiasm Max (Gy)	4.73	0.72		3.70	0.61		2.85	0.60
Right Eye Max (Gy)	3.61*	0.69		3.22	0.60		2.54*	0.45
Left Eye Max (Gy)	3.06	0.50		2.55	0.34		1.98	0.31
Right Lens Max (Gy)	1.86	0.34		1.88	0.29		1.24	0.16
Left Lens Max (Gy)	1.97*	0.32		1.81	0.29		1.17*	0.11
Right Optic Nerve Max (Gy)	4.13	0.98		3.35	0.78		2.19	0.25
Left Optic Nerve Max (Gy)	4.13	0.81		3.24	0.51		2.60	0.62
Brainstem Mean (Gy)	10.66	2.72		9.50	2.86		8.05	1.87
Chiasm Mean (Gy)	4.20	0.77		3.26	0.65		2.74	0.69
Right Eye Mean (Gy)	2.38	0.35		2.16	0.30		1.74	0.20
Left Eye Mean (Gy)	2.72	0.66		2.25	0.40		1.60	0.28
Right Lens Mean (Gy)	1.55	0.20		1.53	0.23		1.10	0.13
Left Lens Mean (Gy)	1.67*	0.20		1.48	0.23		1.09*	0.12
Right Optic Nerve Mean (Gy)	2.99	0.49		2.58	0.48		1.93	0.27
Left Optic Nerve Mean (Gy)	3.76	0.93		2.77	0.53		2.44	0.71

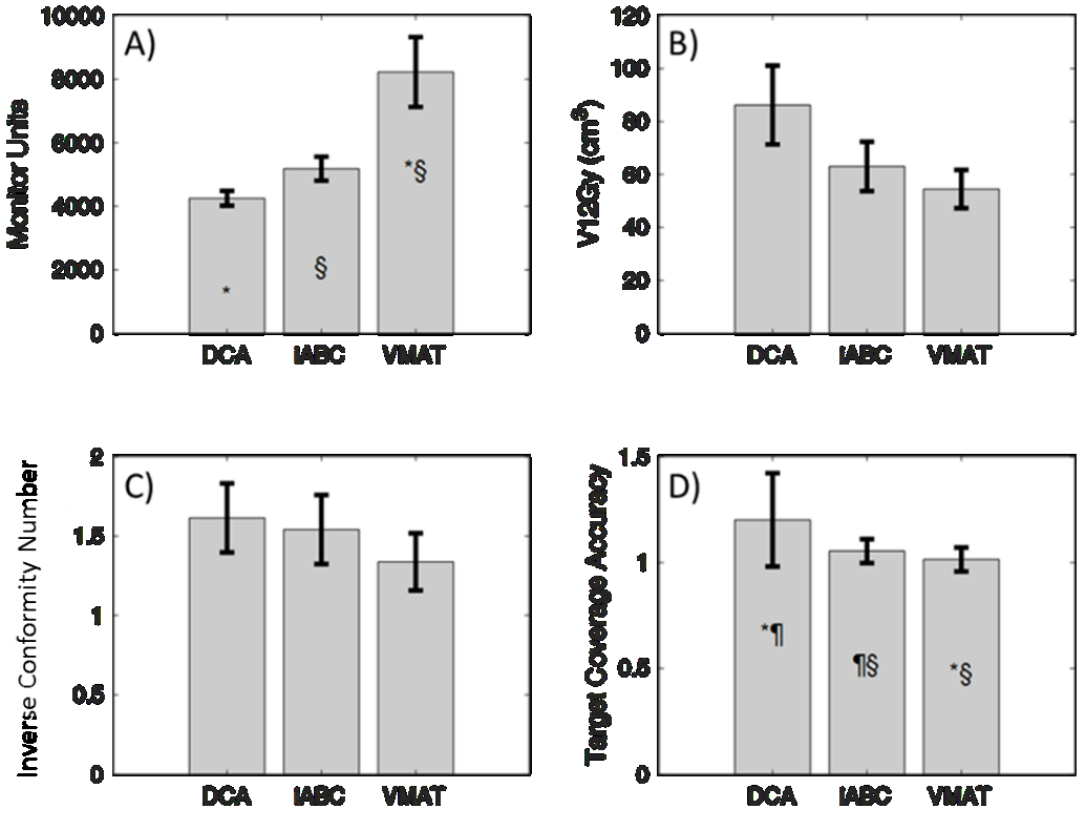

Figure 50: Comparison of mean and standard deviation for clinically relevant metrics for each of the plans (n = 7). The data shown here is tabulated in Table 3. ¶ indicates statistical significance ($p<0.05$) between DCA and iABC, § indicates statistical significance between iABC and VMAT, and *indicates statistical significance between DCA and VMAT. A) is the total plan monitor units, B) is the volume of normal brain receiving 12 Gy or higher, C) is the inverse of the van't Riet conformity number [85], and D) is the target coverage accuracy.

5.6 Discussion

The benefits of iABC are illustrated clearly in Figure 50: a statistically significant decrease of 37% in MU (increase in MU efficiency) when compared to VMAT plans, and a statistically significant improvement of 15% in target coverage accuracy when compared to optimized DCA. Target coverage accuracy may be improved with expansion of the MLC margins; however, degradation of conformity may result. A previous study by this group [60] has demonstrated the potential advantages of collimator optimization in DCA treatments of multiple metastases. However, that study focused on single

prescription multiple metastases cases. The efficiency gains in this study with the iABC plans are not as pronounced as they were in the previous study – a finding that can likely be attributed to the fact that all targets were treated at all control points in that study.

The data in Figures 48 and 50 demonstrate that simultaneous treatment of all targets using optimized DCA, when there is variation in prescriptions doses, results in inferior plans compared to plans generated using the iABC approach. Optimized DCA plans rely solely on MUD optimization to achieve appropriate prescription coverage for all targets, as shown in Figures 50D. However, MUD optimization alone is not sufficient to meet this goal – PTVs (other than the one used to normalize the plan) receive, on average, 14.8% higher dose than that which is prescribed. As prescription doses in stereotactic planning are often assigned based on target volume to control normal brain necrosis, lower prescriptions are assigned to larger volume targets [18]. This increases the disadvantage of non-iABC conformal approaches, as the conformal aperture to a larger target has a larger output factor, contributing more dose to larger targets than to small targets for the same number of MU.

Conversely, in VMAT planning, prescription doses are accomplished by delivering dose in highly modulated apertures with small areas. The result of the use of small apertures is a decreased total administered dose to targets per MU (Gy/MU), requiring additional MU to meet prescription doses. The resulting benefit, as shown in this study, is a statistically significant improvement of 4% in target coverage and marginally superior (though not statistically significant) normal tissues doses compared to iABC (see Table 13 and Figure 50). The cost is >3000 MU more on average,

increasing the required time for the patient to be on the bed during treatment, thus increasing the time available for intrafraction motion. Additional concerns for increased MUs are leakage dose and secondary malignancy induction from low-dose exposure [89, 92, 93, 94].

iABC is a hybrid method of optimization which aims to first coarsely mitigate any discrepancies between target size, depth, and resulting output factor through the optimization of a binary pattern of conformal collimation, followed by a fine optimization through MUD optimization. The result is a method capable of robust flexibility to meet dosimetric coverages using conformal MLC patterns to ensure MU efficiency. The optimization only requires dose to be calculated once for each target at each control point. The optimizer then computes the objective function by approximating total dose as the sum of all dose matrices. While this method ignores the presence of non-target anatomy between targets that may be present in the final MLC apertures (potentially unavoidable due to relative target orientation, or potentially caused by mechanical constraints on collimator motions), the optimization of the collimator angle through dynamic collimator rotation minimizes discrepancies caused by this approximation [60]. By computing this sum, the optimization does not require recalculation of dose with each modification to the aperture, as there are only two possible positions for the aperture: completely closed (zero) or set conformally (one).

Additional benefit is apparent in Figures 51 and 52, which are comparisons of the mean normal brain DVH and the total volume receiving the lowest prescription dose, respectively. While Table 13 shows a small, statistically insignificant reduction in V12Gy

in VMAT relative to iABC, this trend is not consistent for the entire normal brain DVH. A mean of the subtractions of the normal brain DVHs from the iABC plans from that of the VMAT plans is shown in Figure 51. The data demonstrate that iABC is more effective at reducing the low dose wash relative to VMAT, on average, although this trend does not possess contiguous regions of statistical significance. While this dose range is below the dose level correlated to brain necrosis [96], it suggests a systematic sparing in ranges which have become of increasing concern with regard to secondary malignancies [94] and may be of increased importance for retreatments. Figure 52 further illustrates the benefits of iABC to conformal treatments as the volume receiving the lowest prescription dose decreases with implementation of iABC when compared to optimized DCA, although this also did not reach statistical significance. Taken together, Figures 51 and 52 imply that while iABC may not reduce mid-level dose to normal tissue as well as VMAT, it does reduce low-level dose to normal tissue better than VMAT.

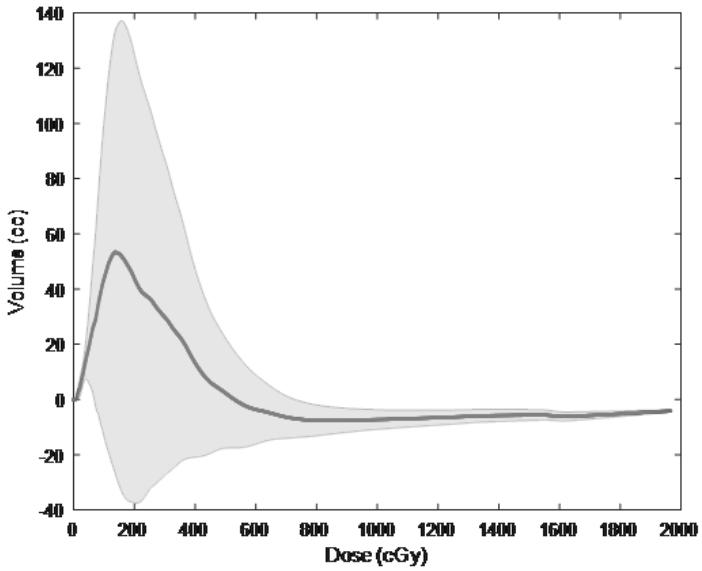

Figure 51: The mean normal brain DVH for iABC subtracted from the mean normal brain DVH for VMAT. Positive value on the y-axis corresponds to higher amount of brain dose for VMAT

than iABC. The solid line indicates the mean value (n = 7), while the shaded area is the standard deviation.

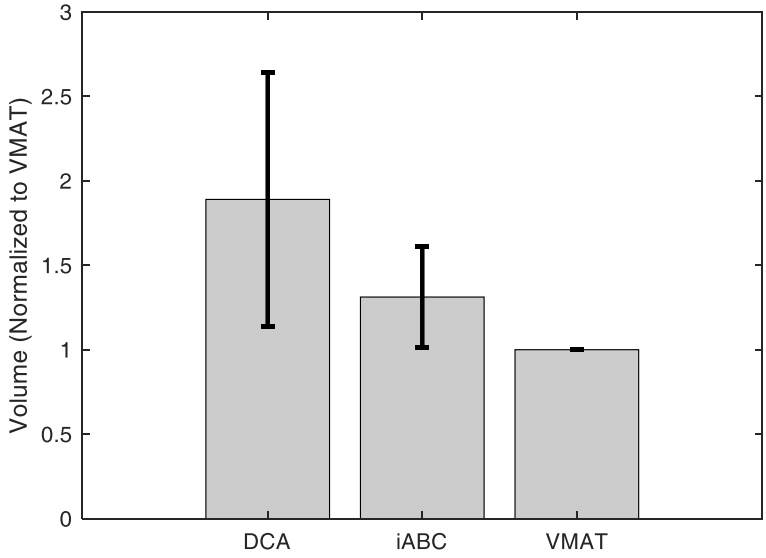

Figure 52: Comparison of the tissue volume receiving the lowest prescription dose (n = 7). Error bars are standard deviation.

The iABC plans have been designed by using discrete control points to approximate dynamic motions of the LINAC axes. Consequently, there will be discrepancies, as with any rotation-based treatment, between calculated and delivered plans. The binary nature of targets being included or removed between successive control points, coupled with the implicit assumption of instantaneous MLC transitions presents challenges to this approximation. Deliveries of plans with dynamic motions apply a linear interpolation to drive a moving part through its prescribed motion between control points. One method to mitigate the effects of the iABC leaf transitions is to insert additional control points for the purpose of maximizing the speed with which those motions take place. The plan is adjusted to initiate these MLC transitions over a specific window of the control point.

By parameterizing the width of this window for MLC transition as a function of control point spacing, one can tradeoff between total treatment time and the dosimetric agreement between delivered and calculated plans. The two extremes of this parameter are included here:

1. If the fraction of a control point to be delivered before initiating the MLC transitions, *p*, is at a value of 1, the entire control point will be completed, followed by a pause on motion of all other axes of the machine as MLC transition is initiated. This represents the highest likelihood of agreement between calculated and delivered dose, however we would expect extended delivery times in order to accommodate repeated pauses to machine axes.
2. If the fraction of a control point to be delivered before initiating these sharp MLC transitions, *p*, is at a value of 0.5, half of the control point will be completed, after which the MLC transition is initiated over the remaining portion of the control point as well as the first half of the next control point. This represents the fastest method of treatment delivery but may impact the agreement between calculated and delivered doses.

Figure 53 shows the average beam-on time of iABC as a function of the width of the motion point parameter compared to the average beam-on time of VMAT. In this calculation, all MLC transit motion to accomplish iABC blinking is initiated at the same fraction of the control point, *p*, regardless of the scale of the transition. This may result in transitions being slower than necessary at lower *p* values. Additionally, at high *p* values, if all axes move as fast as possible, but the requested motions cannot be completed within the window defined by *p*, the gantry will be slowed to permit the motions (gantry slowing

is included in the presented calculations below). The delivery time calculations include the time to deliver the designed trajectories for the MLC, gantry, dose rate, jaw, and collimator. This total value was calculated from the time it takes to deliver each control point in the treatment plan. Using the maximum velocity for each axis on the TrueBeam system (shown in Table 6), the time for the axis with the most demanding displacement between control points can be determined via:

$$t = \frac{\Delta x}{\max(\frac{\Delta x}{\Delta t})}$$

Where *t* is the time to complete the control point, *Δx* is the total displacement between control points, and $max(\frac{\Delta x}{\Delta t})$ is the maximum velocity. As axes on the TrueBeam arrive at control points in temporal coincidence, the axes with the longest total *t* dictates the time to deliver the control point, and all other axes velocities slow to accommodate coincidence. Only the axes motion during beam-on time was used to calculate the delivery time.

The MLC positions in iABC plans have additionally been sequenced to transit parked leaf pairs prior to their employment in an aperture in order to mitigate delays to delivery time for MLC transitions. This ensures that delivery of a control point is never delayed for a leaf to transit from a park position to its position for use in an aperture, but is in close proximity prior to use in an aperture, increasing the efficiency.

Dosimetric agreement of calculated iABC plans and delivered plans over a range of motion point parameters will be the focus of an additional study to establish the gains in treatment delivery times with implementation of iABC. Additional steps could be taken to limit the allowed number of binary collimations to targets or the minimum duration of

a collimation to further reduce delivery times, while maintaining the dosimetric advantages shown in this work by using MUD optimization. In addition, the potential benefit of planner interactivity with the optimizer will be studied to help refine the cost function of the optimizer. Since the iABC plans generated in this study were the result of a single pass through the optimizer, additional gains in dosimetric plan quality may be achievable.

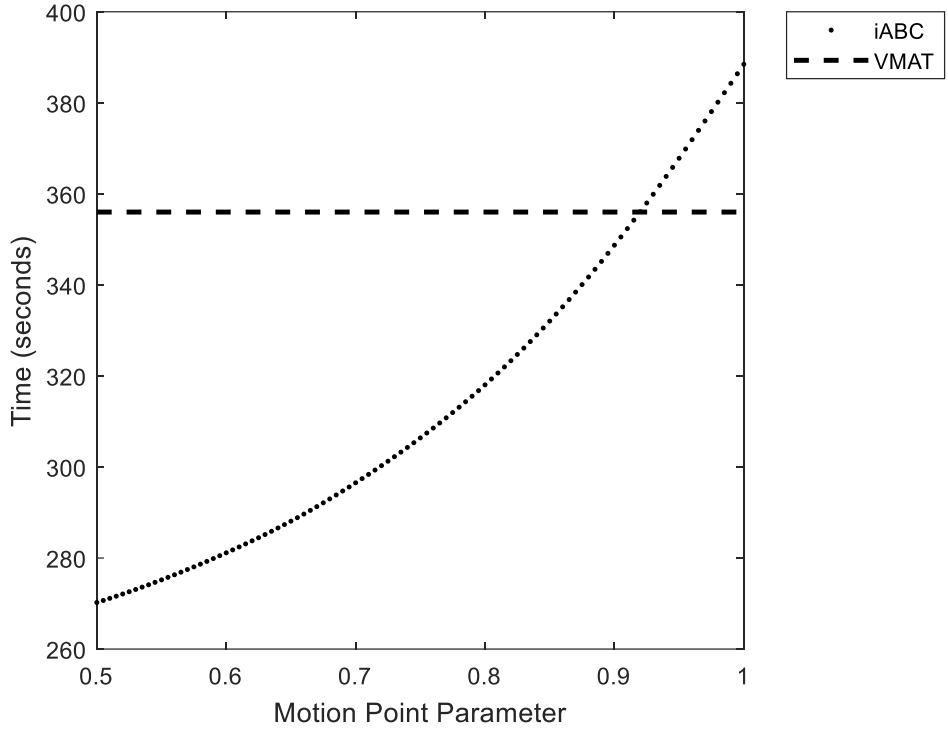

Figure 53: Average calculated delivery times for iABC plans as a function of the motion point parameter compared with the average delivery time of VMAT plans.

5.7 CONCLUSION

iABC is a hybrid-technique capable of combining the MU efficiency and dosimetric robustness of DCA treatment planning, with the dosimetric accuracy of VMAT planning, through the optimization of the pattern of targets to be conformally treated and number of MU at each control point. With substantial gain in MU efficiency over VMAT, iABC has the potential to reduce treatment times in multiple cranial

metastases treatment plans with variable prescriptions, which in turn reduces the time available for intrafraction motion. The method also confers a statistically significant improvement to target coverage accuracy when compared to optimized DCA. Additionally, this method retains the majority of MU efficiency inherent to DCA (37% less when compared to VMAT), without a statistically significant difference in normal tissue dose when compared to VMAT.

CHAPTER 6 MANUSCRIPT 4: CODA: COMBINED OPTIMIZATION OF DYNAMIC AXES

6.1 PROLOGUE

This manuscript establishes a bridge between the technologies defined in Chapter 3 and those in Chapters 4 and 5. While independent optimization of these axes yields dosimetric improvements, synergistic optimization allows for the possibility of the combined benefit to exceed that found independently. Additionally, the pre-calculation of the metrics from Sections 2.3.2 in all combined coordinates of axes positions allows for trajectories to be optimized with reference to a 3D cost-function space previously unavailable.

Additionally, this paper also aims for current clinical practicality, as it does not accomplish gains by employing dynamic rotation of couch and collimator. A novel and sophisticated trajectory definition method is used to generate a final optimized trajectory with additional optimization to the gantry span to yield additional benefits.

Candidate arcs are generated to solve every plane of the solution space, and a user-defined number of final arcs are defined from searching spatially separated collections of candidate arcs. Conventional expert-planned VMAT plans are compared to the output solutions for dosimetric evaluation.

Publication: *MacDonald, R. Lee, Alasdair Syme, Brian Little, Lucy Ward, and Christopher G. Thomas. "Combined Optimization of Dynamic Axes (CODA) in Radiation Therapy." (In preparation).*

6.2 ABSTRACT

Purpose: To develop a novel system for patient-specific combined optimization of couch, collimator, and gantry start and stop angles for use in VMAT treatment planning. The system is designed to produce highly compact dose distributions by optimally sampling the 4π space. Automated trajectory planning is used to reduce normal tissue doses by avoiding beams-eye-view (BEV) overlap with organs-at-risk (OARs) and improve monitor unit (MU) efficiency through collimator angle optimization.

Methods: By merging distinct BEV objective functions used to optimize the couch rotation angle and collimator angle, a three-dimensional cost space (the CODA cube) can be constructed with axes of gantry, couch, and collimator rotation angles. At each voxel in this CODA cube, the cost of implementing this combination of axes positions in a trajectory is quantified. The CODA cube is sampled and explored using a modified constrained Bellman-Ford algorithm to suggest low-cost fixed candidate arcs on each plane of the space, from which 10-arcs are chosen using a k-means clustering algorithm. These arc trajectories are then imported into the Eclipse treatment planning system (v11) and inverse-optimized according to clinical standards. Eight artificial cranial targets were contoured in a test-patient anatomy, and six treatment plans were generated from combinations of three and four targets. The CODA cube plans were compared to standard 4-arc VMAT plans for cranial stereotactic radiotherapy/surgery that were calculated for the same sets of targets; maximum dose to each OAR and total MUs were compared. Both planning methods were inverse-optimized with identical dosimetric objectives.

Results: CODA plans resulted in a reduction in maximum dose to OARs of 20.6% ($p < 0.01$), with maximum brainstem dose decreasing by 2.63 Gy ($p = 0.031$) on average. Mean reduction in total MU was 8.6% ($p = 0.156$), and a mean decrease in normal brain tissue receiving 12 Gy or higher was 3.9% ($p = 0.16$), when compared to standard VMAT methods ($n = 7$).

Conclusion: The optimization of couch, collimator, and gantry angles simultaneously using a three-dimensional optimization space achieves improvement of multiple clinical metrics when compared to conventional VMAT. A statistically significant sparing to OAR maximum doses was seen. Combining these optimizations may yield superior results to independent optimization.

6.3 INTRODUCTION

The optimization of arc trajectories in VMAT radiotherapy has become an active area of research. With the increasing digitization of linear accelerator control systems and the capacity for experimental systems with enabled coordinated motion of gantry, couch, and collimator, the synergistic cooperation of these axes in radiotherapy delivery seems likely to become a clinical reality. The significant dosimetric benefit of increasing the sampling of the 4π space in VMAT through non-coplanar approaches has been repeatedly shown for both VMAT and IMRT [102, 58, 62, 65, 60]. A 2012 study by Panet-Raymond *et al.* [102] showed that non-coplanar IMRT and VMAT techniques provided significantly better sparing of the contralateral optic structures than their coplanar equivalents. In 2015, Wild *et al* [58]. published a comprehensive comparison of nasopharyngeal patients using both coplanar and non-coplanar plans, and additionally compared them to an upper limit benchmark 4π plan with approximately 1400 non-coplanar beam directions. This study

confirmed the dosimetric benefits of non-coplanar irradiation and found that IMRT using optimized non-coplanar beams and VMAT using optimized, arbitrary, non-coplanar trajectories enabled substantial dose reductions in OARs. Wilson, Otto, and Gete [62] presented trajectory-VMAT (TVMAT) in 2017 for SRS that applies a standard beam trajectory formed by dynamic motion of the treatment couch and the gantry. While the couch sweeps through 180 degrees, the gantry sweeps through two to eight partial arcs to change the degree of sampling of the 4π space. Dose rate and MLC sequence are modulated throughout this trajectory using inverse planning. The result is an efficient dynamic delivery which shows dosimetric accuracy, significant sparing of surrounding of normal tissues, dose fall-off outside the target, homogeneity, and conformity. In 2018, Langhans *et al.* [65] developed a noncoplanar VMAT optimization (NoVo) to produce VMAT trajectories using an objective function based on geometrical considerations and a customized path finding algorithm. The group found their method reduced computation time compared to published algorithms and decreased their objective function values in lung, brain, and liver cases when compared to coplanar VMAT. Their brain case was, however, not compared to the non-coplanar four arc VMAT template frequently found in stereotactic radiosurgery (SRS) [45].

Creation of optimized trajectories via multi-dimensional solution spaces generated from clinical and geometric considerations have successfully guided the position of radiotherapy axes in several recent publications. Yang *et al.* [47] produced two-dimensional maps based on geometric overlap between targets and OARs and generated sub-arcs by optimizing the couch-gantry trajectories using hierarchical clustering of minimum score functions, paired with principal component analysis of collimator angles.

These trajectories incorporated simultaneous couch, gantry, and collimator motion, and provided improved dosimetric properties and efficiency in the treatment of CNS tumors. This method was expanded upon by MacDonald *et al.*[60] (Chapter 3) to incorporate factors for OAR weighting based on clinical dose constraints, relative depth of structures involved in overlap, and orthogonality of beam directions with the direction of proximal OARs. Smyth *et al.* [54] produced non-coplanar dynamic couch rotation during VMAT using a combination of ray-tracing and graph search algorithms applied to three sites: partial breast, brain, and prostate. A cost-map was generated reflecting the number of OAR voxels intersected at each potential source position. The least-cost path was determined using Dijkstra's algorithm. This technique was shown to reduce dose to specified OARs for plans otherwise comparable to conventional coplanar VMAT.

Manufacturers of radiosurgery software have also begun incorporating couch trajectory optimization into commercially available products. Brainlab has incorporated 4π optimization into Elements Cranial SRS (Brainlab AG, Munich, Germany) [103] to automatically select couch angles based on critical OARs, as well as to identify optimal gantry start and stop angles. Their VMAT optimization then incorporates trajectory optimization to create an optimized deliverable plan. In order to increase efficiency, Varian's Hyperarc (Varian Medical Systems, Inc., Palo Alto, USA) [104] implements automatically delivered multiple non-coplanar arcs without the need to enter the treatment room and manually reposition the patient. The system delivers multiple arcs from a predefined class solution and performs imaging automatically before each arc.

This presents a precedent for clinical dynamic rotation of couch and gantry without user intervention.

The work presented here aims to define an automated patient-specific approach to trajectory design by defining the trajectory of the couch rotation angle, gantry start and stop angle, and collimator angle for any stereotactic radiosurgery plan. This is the only work that generates a complete three-dimensional cost function analysis and traverses this space using a system of graph theory algorithms, producing an optimal set of arcs to improve the dosimetric properties of VMAT plans. The trajectories are generated without user-intervention or any requirement for custom parameter input. These trajectories do not incorporate the simultaneous rotation of couch or collimator with the gantry, and unlike a number of previous works in trajectory optimization, these trajectories are immediately implementable in any clinic currently delivering stereotactic radiosurgery.

6.4 METHODS

To synergistically optimize multiple dynamic treatment axes simultaneously, a system of algorithms has been designed to automate the design of patient-specific multi-axes trajectories. The system uses patient contour and machine profile information to define a solution space based on possible treatment coordinates. Using previously published metrics (outlined in Chapter 3 and Chapter 4) for quantifying axis position

suitability based on beam's-eye-view (BEV) information, the system combines multiple objective functions for the combined optimization of dynamic axes (CODA).

6.4.1 CODA Cube

To measure a patient-specific solution space, a three-dimensional resource (hereinafter, CODA cube) is constructed with dimensions equal to the entire range of motion for the three axes being optimized: gantry, couch, and collimator rotation angles. At every possible combination of these three axes, a unique voxel is given an objective function value to quantify the suitability of including this combination in the treatment plan. The CODA objective function is constructed from two previously published methods for BEV suitability quantification: the 4π objective function (outlined in Chapter 3), used to reduce dose to organs-at-risk of exposure (OAR); and the whitespace objective function, used to increase treatment plan monitor unit (MU) efficiency and reduce dose to normal brain (outlined in Chapter 4).

6.4.1.1 4π Objective Function

The 4π objective function is computed from the OAR and target volume (PTV) constituents of the BEV. At every coordinate of couch and gantry rotation angle the total cost, *E(c,g)*, is computed from Equation 52 (as outlined in Chapter 3):

$$E(c,g) = \sum_i w_i \times w_F \left(\frac{PDD_i}{PDD_t}\right)_{c,g} \times w_O \left[\frac{L_i(c,g)}{A_t(c,g)} \times \frac{L_i(c,g)}{A_i(c,g)}\right] + w_U \cos(\alpha)^n \quad (52)$$

where w_i is the relative weighting associated with each OAR and is defined here as the inverse of the tolerance dose for the OAR in question [83, 15]; $PDD(d_{OAR})$ and $PDD(d_{PTV})$ are the values of the PDD curves for a 6 MV beam with field size 10x10 cm^2 and SSD = 100 cm for the i^{th} OAR and the PTV at the depths d_{OAR} and d_{PTV}, respectively; $L_i(c,g)$,

$A_t(c,g)$, $A_i(c,g)$, are the area in the BEV as projected onto a plane at isocentre of the overlap between the PTV and the i^{th} OAR, the area of PTV, and the area of the i^{th} OAR, respectively, as they are first defined and published in 2011 [47]; and α is the three dimensional angle between the vector joining the centre-of-mass (COM) of the PTV and the source position, and the vector joining the COM of the PTV with the COM of the OAR deemed most urgent for sparing (in this study designated by closest proximity to PTV). The variables w_F, w_O, and w_U are weighting coefficients for terms in the 4π cost equation and are assigned values of one in the context of this work.

4π objective function maps are measured for every combination PTV and OAR and summed based on the designated weighting values as depicted in Equation 52. The anatomical structures were projected on to an isocentric plane using previously published in-house MATLAB (The MathWorks, Inc., Natick, Massachusetts, USA) software, which extracts structure information from RT structure set DICOM files and simulates the BEV for a given couch and gantry position. The calculated objective function values are catalogued into a map containing the full range of the couch rotation axis (191 degrees) and gantry rotation axis (360 degrees). Coordinates which correspond to a physical collision of the gantry and the couch were assigned infinite cost to prevent their inclusion in a trajectory. The coordinates of the collision space were manually measured on a Varian TrueBeam STx (Varian Medical Systems, Inc., Palo Alto, CA, USA) linear accelerator at the Nova Scotia Health Authority (NSHA). An anthropomorphic phantom was placed on the couch in a typical stereotactic radiotherapy setup. The gantry and couch were rotated over their ranges of motions. A point in a collision zone was recorded for which the couch position and gantry position were such that: (a) the collision

avoidance system was triggered, or (b) the gantry was within 5 cm of either the treatment bed or the phantom.

6.4.1.2 Whitespace Objective Function

The whitespace objective function is used to optimize the collimator rotation angle, and by consequence (as outlined in Chapter 4), the direction of multi-leaf collimator (MLC) leaf travel. The objective function quantifies the area of non-target anatomy left uncollimated in the BEV when the MLC is fit conformally to the target. By categorizing and measuring these areas in any BEV defined by the couch rotation angle, θ_{CH}, gantry rotation angle, θ_{GA}, and any chosen collimator angle, θ_{CL}, the parameter denoted by whitespace (W) can be defined by Equation 53:

$$W(\theta_{CL}, \theta_{CH}, \theta_{GA}) = w_1 A_{Jaw} - w_2 A_{PTV} + w_3 (A_{PTV} \cap A_{OAR}) - w_4 A_{MLC} \quad (53)$$

where A_{Jaw} is the area collimated by the fitted rectangular jaws, A_{PTV} is the area of the PTV, $A_{PTV} \cap A_{OAR}$ is the area of the OAR overlapping with the PTV, and A_{MLC} is the area collimated by the MLC in a conformal position when the entire PTV is targeted. The variables w_1 -w_4 are weighting coefficients to control the significance of each term and are assigned values of one in the context of this work. The whitespace output from Equation 53 is catalogued into a three-dimensional space (whitespace cube) containing the full range of couch rotation axis (191 degrees), full range of gantry rotation axis (360 degrees), and full range of collimator rotation axis (180 degrees).

For this work, a Varian HD 120 MLC (Varian Medical Systems, Inc., Palo Alto, California, USA) is used since the clinical plans generated involve stereotactic radiosurgery, although the algorithm is equally applicable to any other MLC design. This

MLC was modeled according to the vendor specifications for leaf number and width. The HD MLC 120 is composed of two bi-lateral banks, each composed of sixty motor-positioned tungsten leaves [76]. The central 32 pairs of leaves have a 2.5 mm width and the peripheral 28 leaf pairs have a 5 mm width when projected to isocentre.

6.4.1.3 Combined Objective Function

To merge the 4π and whitespace objective functions such that the total cost of suitability for any combination of gantry, couch, and collimator can be quantified, the two-dimensional couch-gantry planes of the whitespace cube are extracted such that each plane has an iso-collimator angle, and the mean of every couch-gantry pixel is taken between the 4π and whitespace values in order to promote contribution from both metrics, and ensure that all instances of cost from either metric are recognized. These averaged two-dimensional objective function planes are then used to construct the combined three-dimensional CODA cube. The results of combining objective functions on a single plane into a CODA cube are shown in Figure 54.

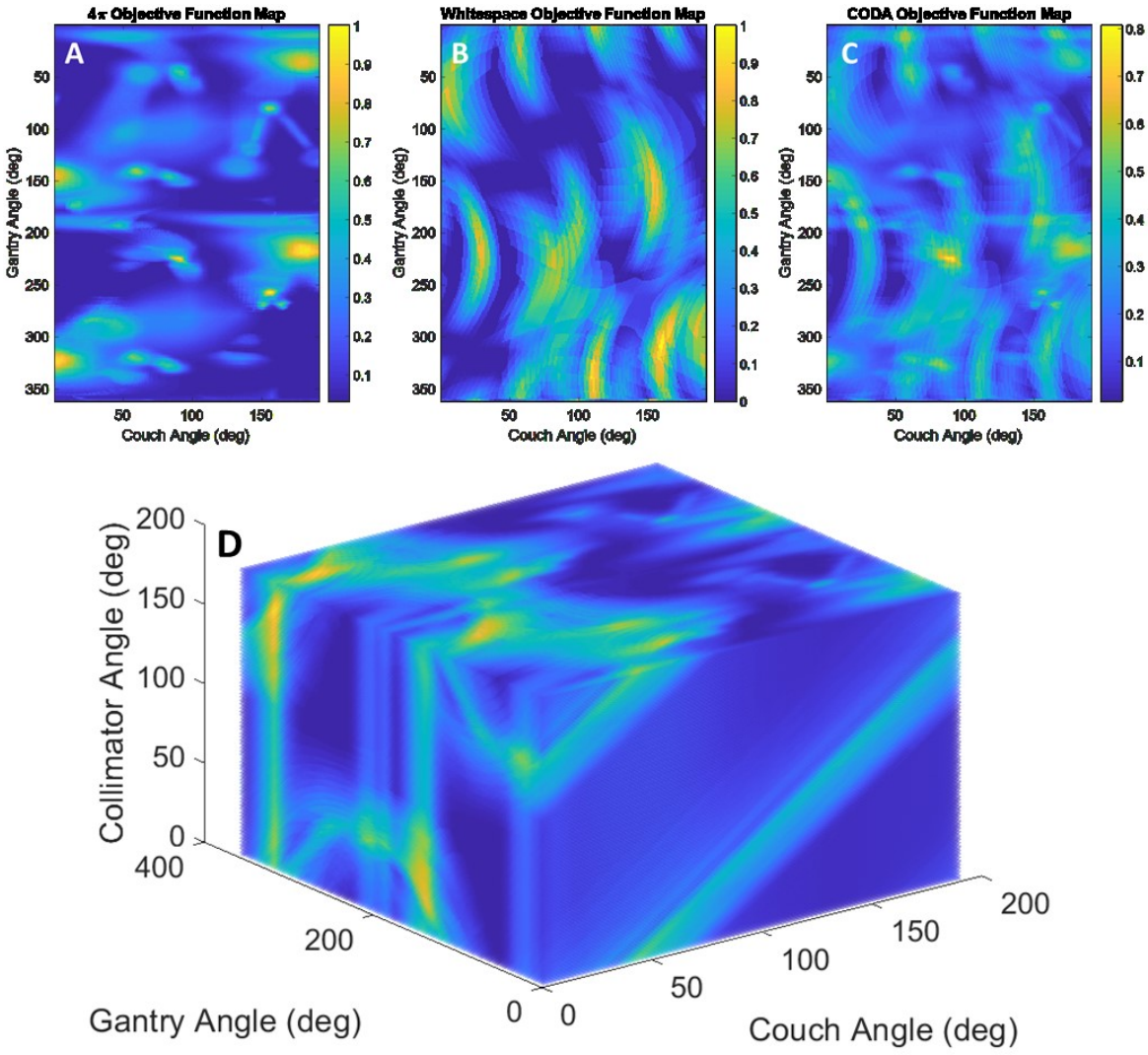

Figure 54: An example of a single plane of the CODA cube. A) The 4π objective function map for all PTVs and OARs included in the optimization. B) A couch-gantry plane of the whitespace cube taken for a single collimator angle. C) A pixel-wise mean of the planes shown in A & B. D) CODA cube for one patient as constructed from the method described in Section 6.4.1.3.

6.4.2 CODA Cube Navigation

The CODA cube outlined in Section 6.4.1.3 is valuable as a reference for the design of optimal arc trajectories for use in radiotherapy treatment planning. Contiguous voxels of low cost in the cube represent potential paths for the linear accelerator to follow in rotational radiotherapy and can be used to build arcs in the treatment planning system. This work translates trajectories designed in the CODA cube into arcs used in VMAT

planning for cranial stereotactic radiosurgery using Eclipse. Using this treatment planning system for optimization places restrictions on the allowable trajectories, narrowing the trajectory solution space from all possible trajectories in the CODA cube to all trajectories in the CODA cube that meet the restrictions of the VMAT optimizer (PRO v. 11.0.31, Varian Medical Systems, Inc., Palo Alto, California, USA). These restrictions are that the total arc gantry travel length must be greater than or equal to 30 degrees and that there can be no more than 10 arcs in the final arc solution. The task then becomes finding all allowable trajectories and identifying the optimal set of arcs for a patient-specific CODA cube. The CODA trajectory problem can be expressed in graph theory notation by the following four expressions:

$$S = min \sum_{(i,j)\in E} c_{ij} x_{ij} \quad (54)$$

$$(j - i) \geq 30 \quad (55)$$

$$\sum_{(i,j)\in E} x_{ij} \leq 10 \quad (56)$$

$$(i,j) \in Z; \;\; i < j \quad (57)$$

where S is the final arc solution; c_{ij} is an arc beginning at gantry angle i and ending at gantry angle j; and x_{ij} is a binary property of arc c_{ij}, where $x_{ij} = 1$ indicates that it is part of the final arc solution and a 0 if it is not. Expressions 55 and 56 are the restrictions placed on the trajectories to be acceptable by the Eclipse VMAT optimizer, as mentioned above. While these restrictions are specific to trajectories optimized using Eclipse, this method is generalizable, and would expand the trajectory solution space with the removal of these restrictions. Additional restrictions include the use of only fixed couch and collimator geometries due to current LINAC hardware and software limitations, meaning the rotation angle of these axes can be defined only once per arc. With these restrictions, the

procedure for defining an optimal set of arcs for a given CODA cube is conducted in four steps: (1) finding the optimal set of allowable minimum cost arcs for traversing a given couch-gantry plane, (2) accumulating all couch-gantry plane solutions into a set of candidate arcs, (3) separating arcs into spatially distributed clusters by use of a k-means clustering algorithm, and (4) selecting the arc with longest total gantry span from each cluster to be used in the final solution.

6.4.2.1 Generation of Candidate Arcs

To find the optimal set of allowable minimum-cost arcs, a set of candidate minimum-cost arcs are first constructed by independently solving each couch-gantry plane of the CODA cube for the optimal set of minimum-cost arcs which compose a piece-wise function that spans the gantry domain (see Figure 55) and is allowed by the VMAT optimizer restrictions.

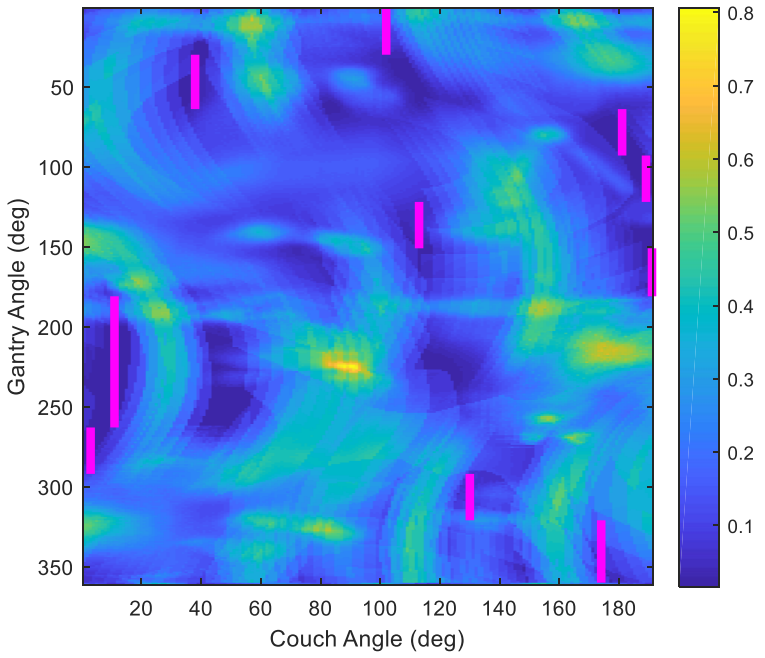

Figure 55: The couch-gantry plane of the CODA cube taken for a single collimator angle as shown in Figure 54C. The magenta path shows the minimum cost piece-wise function trajectory

with ten or fewer arcs.

To solve a couch-gantry plane, a collection of all possible arcs within the plane was assembled. For all arcs, c_{ij}, starting at gantry angle i and ending at gantry angle j, the minimum-cost couch angle was identified, $\min(c_{ij})$. The $\min(c_{ij})$ arcs were then matched into combinations that form piece-wise functions spanning the gantry domain. The minimum cost piece-wise function that uses the least number of arcs was determined using a modified constrained Bellman-Ford algorithm. A maximum of 10 arcs was permissible to comply with Expression 56.

When all planes have been independently solved, the plane solutions are compiled to generate the full set of low-cost candidate arcs from which the final arc solution set will be chosen.

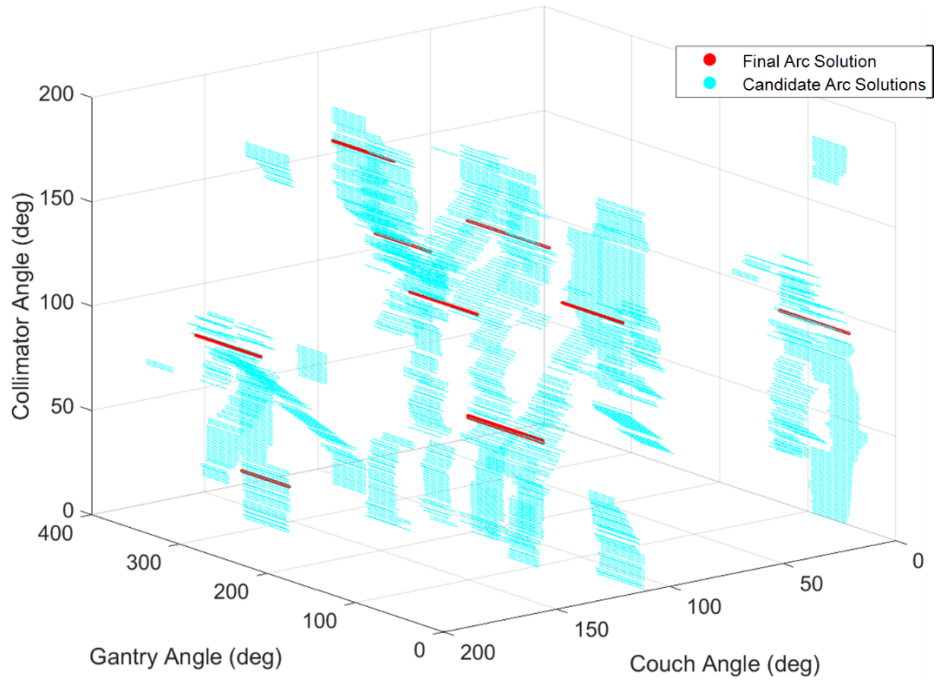

Figure 56: All candidate arcs generated for the CODA cube shown in Figure 54D. Candidates are generated for each couch-gantry plane as depicted in Figure 55.

6.4.2.2 Final Arcs Solution Selection

To define the selected set of arcs that compose the final arc solution, the average gantry position and couch position for each arc were entered into a k-means clustering algorithm to identify ten clusters of candidate arcs that are spatially separated in the couch-gantry dimension. Enforcement of this arc separation is used to promote sampling of the 4π space. From each of these ten clusters, the arc with the longest total gantry span was selected for use in the final arc solution. The longest gantry span was used to maximize the total number of control points in the final arc solution, increasing the potential for the dose optimizer to identify opportunities to improve target conformity and minimize dose to OARs.

6.4.3 VMAT Planning & Comparison

To test the potential benefits of patient-specific trajectory optimization using CODA, eight artificial target volumes were manually contoured using Eclipse v11. We chose to create artificial targets due to the low number of three and four target clinical cases in our clinical database. The artificial targets span the volume sizes appropriate for a prescription of 24 Gy as per RTOG 9508 [18]. All dose calculations were performed in Eclipse using AAA v.11.0.31 and a calculation grid size of 1.5 mm. All artificial targets were within 5 cm of an organ at risk, with four targets closer than 1 cm (0.44 cm from the optic chiasm, 0.74 cm from the brainstem, 0.66 cm from the brainstem, and 0.28 cm from the brainstem), to challenge our algorithms.

Combinations of these targets were used to generate seven cases of three and four target geometries. Two VMAT plans were generated for each case: one using the

standard VMAT cranial stereotactic arc template (modified from UAB [45]) used at the Nova Scotia Health Authority (NSHA) (shown in Table 14), and one using the case-specific trajectory defined in CODA-cube optimization. All VMAT planning was conducted by one of the authors (L. Ward), a CMD-certified treatment planner with six years of VMAT planning experience. Most of the VMAT planning required up to four passes through the optimizer to meet OAR and PTV constraints, with adjustments on objectives and priorities on each pass. Automatic normal tissue objective (NTO) was used in all cases, as well as a tuning ring around the PTVs (4 cm outer diameter, 1 cm inner diameter). All artificial targets were treated using prescription doses of 24 Gy prescribed to the 90% isodose.

Table 14: Gantry and couch parameters for the clinical stereotactic plan used at the NSHA [9]. CW = clockwise, CCW = counter-clockwise. These coordinates are in the IEC 1217 system.

Couch Angle (°)	**Gantry Start** (°)	**Gantry Stop** (°)	**Gantry Direction**
45	180	0	CCW
0	180.1	179.9	CW
90	150	355	CCW
315	0	180	CW

Clinically relevant metrics were extracted from all plans using MATLAB scripting: extracted were: total MU, brain volume receiving 12 Gy or greater, inverse van't Riet conformity number [85] for all targets, and maximum dose delivered to the brainstem, eyes, lenses, optic chiasm, and optic nerves.

6.5 RESULTS

6.5.1 VMAT Planning & Comparison

Figures 57 – 59 and 61 illustrate the results averaged over the seven-plan cohort. The most salient planning details are shown in Figure 57: a decrease in maximum dose to

the brainstem of 24.4% (p = 0.031), a mean MU reduction of 8.6% (p = 0.16), a mean V12Gy reduction of 3.9% (p = 0.16), and a 0.1% reduction in inverse van't Riet conformity number [85] (CI) with implementation of CODA. All errors are shown as standard deviation. Figure 58 shows the mean and standard deviation values of maximum doses for all OARs used in the CODA optimization. CODA optimization decreased the maximum OAR dose on average in all but one OAR, the left eye. The four OARs with the highest dose on average, the brainstem, the chiasm, and the optic nerves, had the highest amount of dose spared with implementation of CODA. Figure 59 shows the mean DVHs over the test patient population for brainstem and chiasm (curves on the left side of the plot) and target volumes (curves on the right side of the plot), all treated to 24 Gy. This plot illustrates that while coverage was almost identical for both cases, there is consistently lower doses to the brainstem and chiasm at all doses in the DVHs across the population with implementation of CODA. Figure 60 depicts the trajectory as planned via

the CODA optimization for one of the three target cases in the study.

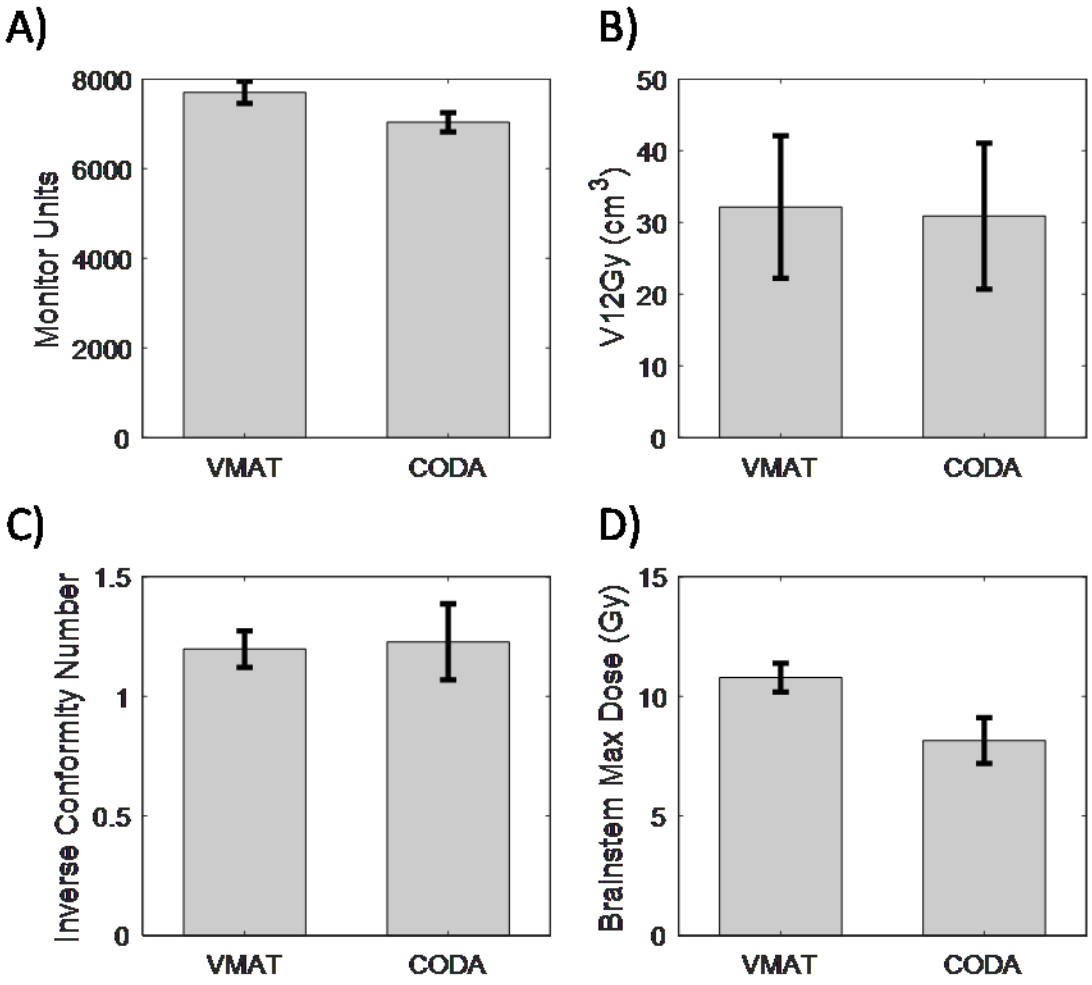

Figure 57: Planning metrics for the comparison of CODA and standard VMAT plans (n=7). A) Total plan monitor units. B) Volume receiving 12 Gy or more. C) Inverse van't Riet conformity number [85] D) Maximum dose to the brainstem in Gy. All errors bars are standard deviation.

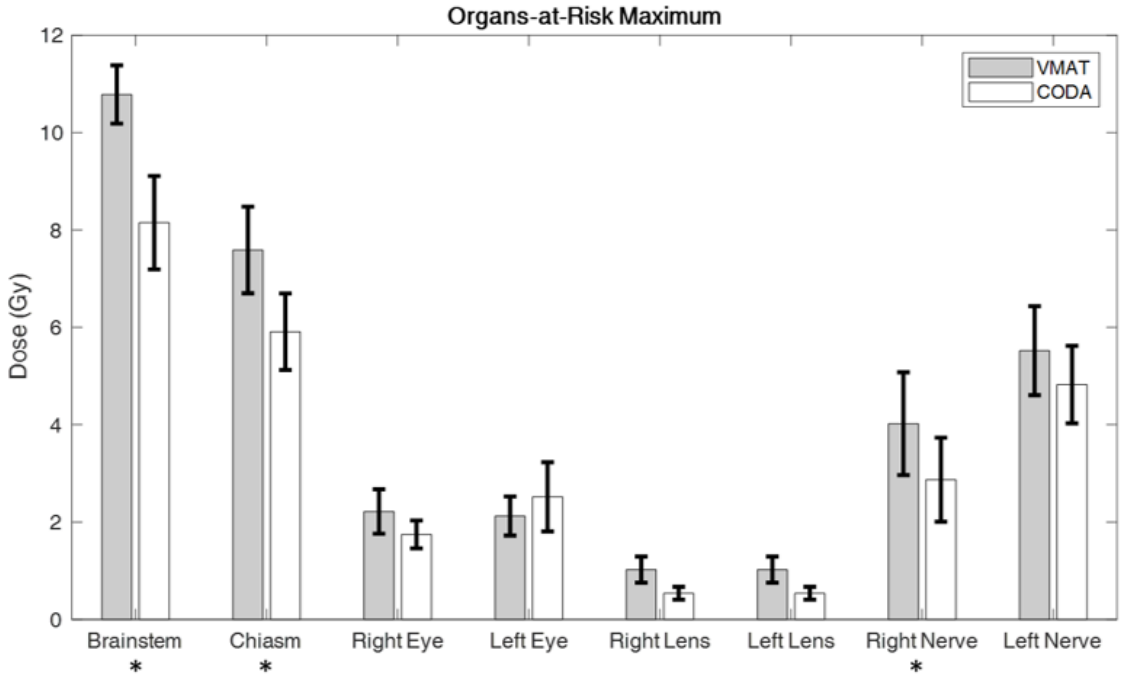

Figure 58: Comparison of maximum dose to OARs used in the planning comparison (n = 7). All errors bars are standard deviation. * indicates statistical significance at $p < 0.05$.

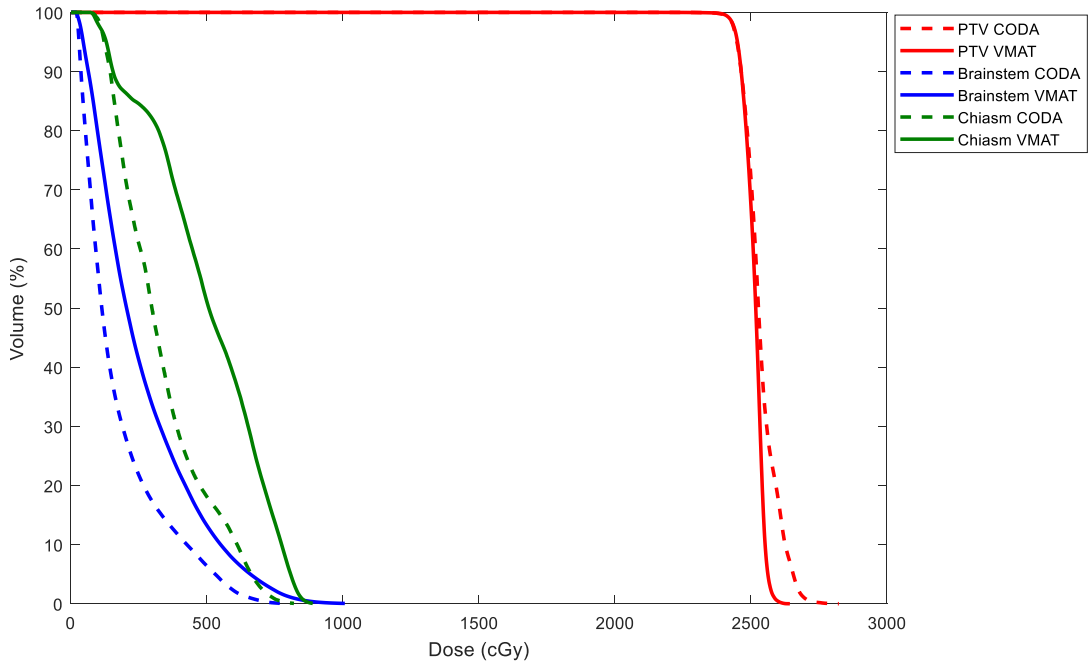

Figure 59: DVH comparison of the mean DVHs for the PTVs, brainstem, and chiasm (n = 7). The dotted lines indicate the mean for CODA plans, while the solid lines indicate the mean for the VMAT plans.

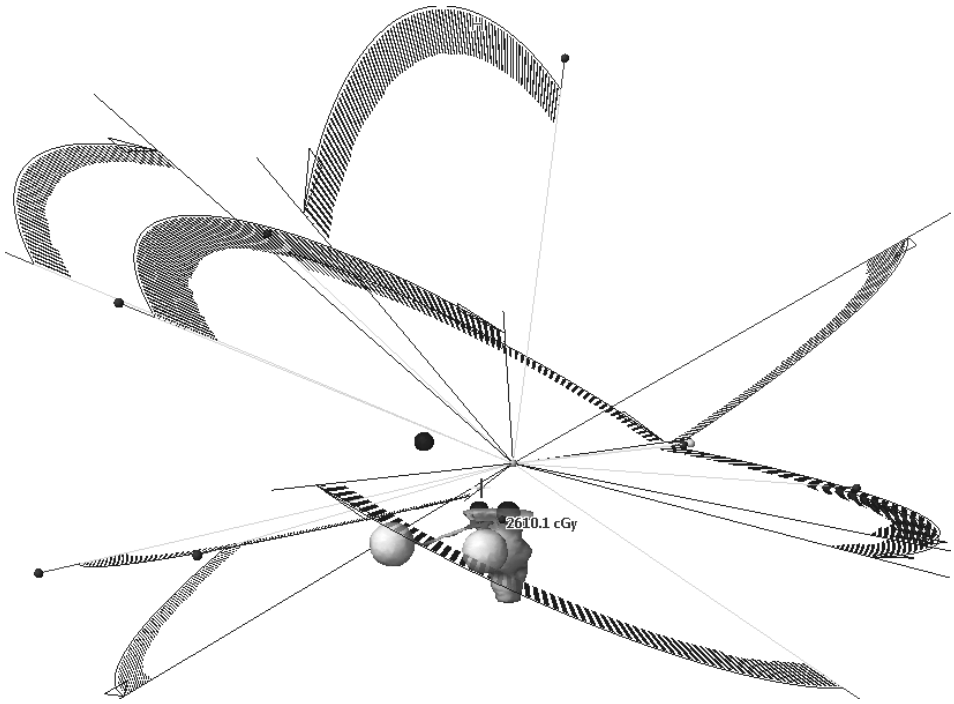

Figure 60: An example of a CODA trajectory overlaid on patient anatomy. This final arc solution was generated from the patient-specific CODA cube via the methodology outlined in section 6.4.2.

6.6 DISCUSSION

The benefits from introducing this automated trajectory optimization are visible in Figures 57 – 59 and 61. In this test patient population, there was statistically significant sparing of dose to the brainstem, which was the most proximal and most critical structure included in all treatment plans. This benefit was gained without compromise to target conformity, as both plans have almost identical average conformity values. Figure 59 displays the agreement in target DVHs and benefit to the average brainstem and chiasm DVHs with implementation of CODA. The dose was normalized such that 24 Gy was assigned to cover 99.5% volume of the coldest target. At the shoulder of the average target DVHs, we can see excellent agreement between the results from the CODA and VMAT plans. While the maximum dose in targets appears hotter on average for CODA than for standard VMAT, this difference is not statistically significant, nor of clinical

significance. Additionally, from Figure 58 we can see that this increased benefit to the brainstem did not come with a compromise of focus to any other OAR. On average, all OAR maximum doses decreased with implementation of CODA, except for the left eye which increased by a statistically insignificant amount and were below clinical dose constraints with both techniques. Figure 61 displays that the sparing of these OARs is not limited the maximum dose, but is present in mean dose as well, indicating that sparing is occurring throughout the volume of the OAR with CODA when compared to standard VMAT. While mean dose reduction would be of interest in the case of retreatment, in the context of single treatment maximum dose is the clinically relevant metric.

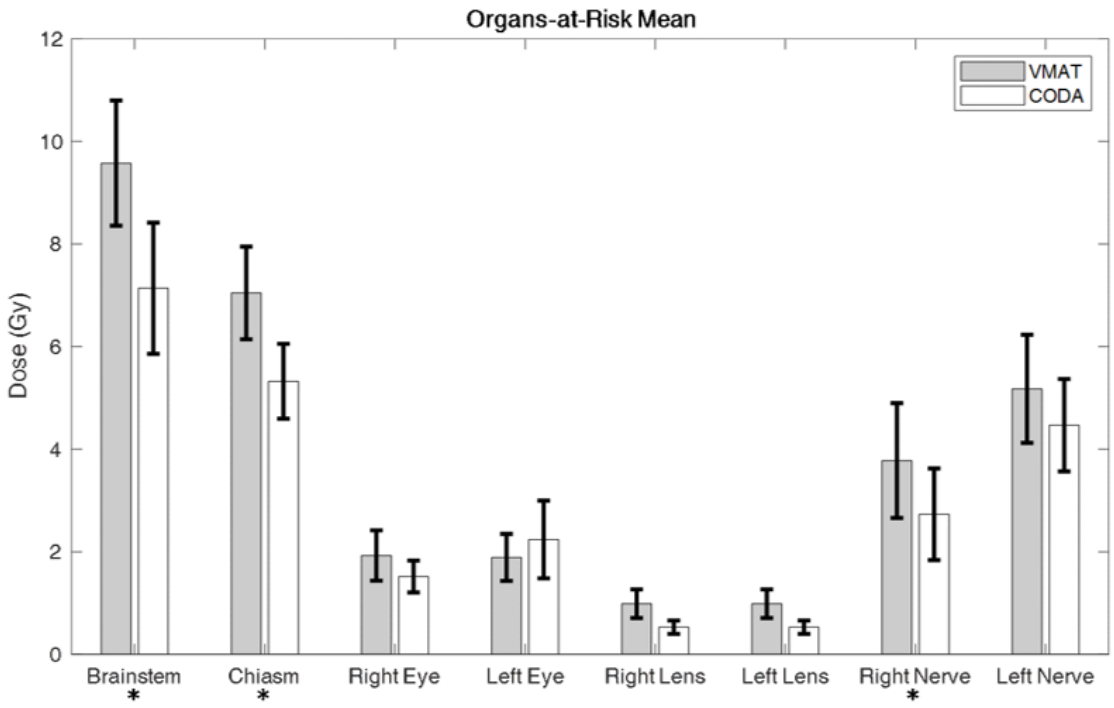

Figure 61: Comparison of OAR mean dose used in the optimization of CODA trajectories in the planning comparison (n = 7). All errors bars are standard deviation. * indicates statistical significance at $p < 0.05$.

The redistribution of dose to avoid OARs and retain target coverage has not increased the volume of brain receiving 12 Gy or higher. As indicated by Figure 57B,

there is a small, statistically insignificant reduction in the V12Gy from CODA when compared to standard VMAT. Figure 57A shows the improvement in MU efficiency with implementation of CODA. Six of the seven plans had fewer MU with implementation of CODA. The percent reduction in total MU for each of the cases was 6.65%, 12.9%, 7.43%, 10.2%, 17.7%, 16.7%, and -15.1%. The case which showed an increase in MU included the three targets closest to the brainstem, two of which were within 5 mm. This case required substantially more modulation to spare the brainstem than the other plans. In the six plans showing decreased MU, the cause of this is likely two-fold: the decrease of the presence of OARs in the BEV, leading to an increase in overall aperture area; and the optimization of the direction of MLC leaf travel via collimator optimization, leading to an increase in the ability to deliver dose to multiple targets simultaneously without irradiating the normal tissue between them. A decrease in irradiation of normal tissue will also result in less demand on the PRO algorithm, through NTO sparing, in order to reduce dose to these tissues, which may result in less fluence modulation and fewer MU. This increased dose efficiency leads to a decrease in the total required MUs, which may in turn decrease the total plan treatment time, hence reducing the opportunity for intrafraction motion to occur.

Figure 60 is a visualization of the trajectory produced from the CODA cube for a test patient in the dataset. The increase in the diverse number of planes of incident beams when compared to conventional trajectories is clear from this overlay on the patient anatomy. While k-means clustering finds groups of candidate arcs which are spatially separated in the couch-gantry plane, there remains the possibility for these arcs to be very similar in their incident beam angle direction, leading to the potentially redundant

inclusion of two arcs sampling the same space. Additionally, if this occurs on multiple arcs in the final arc solution, this could bias the dose distribution toward this oversampled space. While this possibility was not found in this patient subset, and not detected in the clinical metrics examined, additional work will focus on enforcing separation of solutions on the 4π sphere to ensure efficient sampling.

While it is not guaranteed that the trajectory definition process returns the optimal set of arcs, the algorithm does enforce that the arcs are members of the optimal solution to their couch-gantry plane and are thus inherently (at least locally) low-cost members of spatially separated clusters and are long in gantry travel to promote flexibility in the optimizer. Additionally, an arc with a long gantry travel that is a member of an optimal low-cost solution for its couch-gantry plane is more likely to have a lower cost per control point than an arc with short gantry travel.

Additional gains will be expected in trajectory optimization and dosimetric benefit with the removal of VMAT optimization restrictions in treatment planning systems, and the inclusion of simultaneous rotation of multiple LINAC axes. This method could be generalized to trajectories with simultaneous rotation by first navigating each couch-gantry plane using a minimum cost dynamic trajectory algorithm and finding the longest contiguous gantry-span regions in the 3D space of the cube from the candidate dynamic trajectories.

6.7 CONCLUSION

CODA represents an automated means of optimizing a multiple-axes trajectory of a VMAT plan to reduce the number of total MU and significantly lower doses to critical surrounding OARs without compromising the dose to the target. CODA is a complete software system requiring no user intervention to produce superior trajectories and is immediately implementable clinically. It is a method of automatically detecting geometric challenges of demanding multiple metastasis plans and suggesting optimal arc arrangements. The system works with current restrictions on the planning system to provide the highest achievable flexibility to the planner. Provided identical procedure in planning optimization and analysis, the CODA plans proved superior to standard VMAT in this test-patient study.

CHAPTER 7 CONCLUSIONS

7.1 SUMMARY

The purpose of this thesis is to develop and implement novel technologies to automate the improvement of plan quality, specifically, as applied to cases which present difficult anatomical geometries in stereotactic radiotherapy planning. By beginning with insight into the decisions made by expert planners to further improve plans in complex scenarios, these optimization methods aim to thoroughly analyze and catalogue the available decisions and provide a user with an optimal solution, alleviating the trial-and-error approach normally associated with demanding planning. The reduction of OARs in the target BEV, as conducted in 4π optimization (Chapter 3), and the improvement of the efficacy of collimation, as conducted in collimation optimization (Chapter 4), reduce the need for MLC modulation to accomplish dosimetric sparing. This enables the use of more conformal apertures that maximize planning efficiency. With techniques for state-of-the-art dose planning with conformal apertures that can be conducted without user intervention, such as iABC (Chapter 5), the need for iterative hands-on planning with VMAT is reduced. This presents the possibility of end-to-end treatment planning automation that produces statistically significantly superior plan quality without iterative planning. Further, these fundamental principles can be applied to generate new means of delivering radiotherapy through the creation of dynamic trajectories based on optimizing patient-specific metrics. While some of the methods within this thesis contain objective functions with weighting parameters whose impact has not been explored, the performance of these methods in their current embodiments and in the context of the test patients shown throughout is clear.

The first manuscript is an example of the impact a small-scale modification to radiotherapy can have with implementation. This manuscript modifies the couch rotation angle of the conventional stereotactic arc arrangement to minimize a cost function purposed to minimize target/OAR overlap in the BEV and encourage orthogonality of the radiation entrance angle with the direction of the most proximal OARs. Otherwise, this planning methodology is identical to the conventional method of planning VMAT SRS cases. This method is applied to acoustic neuroma cases to both challenge the optimizer to minimize OAR doses in clinically demanding scenarios, and to show its utility as a resource in treatment planning. Application of this methodology showed statistically significant reductions to both mean and maximum doses to OARs compared to conventionally planned VMAT cases. Adding the USF to the cost equation created an additional 2% maximum dose sparing to the brainstem (the most demanding OAR to spare in all cases) without statistically significant degradation of maximum dose sparing for other OARs in the patients. Additionally, the method was applied to less demanding cases with more distant OARs and showed similar ability to spare OARs. This sparing of normal structures was accomplished without significant impact of delivery to the target volume.

The second manuscript is a collimator optimization method which examines the BEV using a cost equation calculated for every valid collimator angle. The system uses the fundamentals established in the first manuscript to assemble a cost-function space composed of the output of the cost equation. As regular modification to collimator orientation has no bearing on potential LINAC and patient collisions, dynamic collimator trajectories are much more apt to be implemented with little modification to current

clinical planning software and LINAC control systems workflow. A dynamic algorithm generates trajectories across the solution space which maximizes the efficacy of collimation throughout a treatment. This system was validated using known geometries and it was shown that whitespace correlates strongly with the mean dose to the normal tissue immediately surrounding targets in multiple metastases scenarios.

To test the system, artificial targets were contoured in reasonable locations and volumes [18] in demanding proximity to OARs. The system was applied to DCA treatment plans and compared to state-of-the-art VMAT. While OAR maximum doses were comparable between methods, total plan MU was reduced by approximately 43% for three target cases and 50% for four target cases. Additionally, low doses to normal brain were substantially decreased on average with implementation of dynamic collimator optimization. The volume of normal brain receiving 12 Gy or higher, associated with radionecrosis, was decreased, but was not statistically significant. Patients can present with multiple brain metastases requiring varied prescription doses. Modulating MU to accomplish these varied prescriptions to the same degree as VMAT is not possible using optimized collimator DCA, thus creating the motivation for the technology discussed in the third manuscript.

The third manuscript extends the optimization practices described in the second manuscript by creating a novel collimation pattern which maximizes aperture area to specified targets while they are being treated and completely shields them at specified control points. While this is a drastic reduction in collimation degrees of freedom compared to VMAT treatment planning, in which each leaf is capable of dynamic collimation independently, each iteration of the iABC optimizer creates a greater

perturbation to the global dose solution, sampling a much more diverse set of solutions to optimal collimation compared to fine adjustments. Additionally, it makes the methodology of the second manuscript much more suited to application to multiple metastases cases with varied prescription doses as individual targets can be collimated independently. Application of this technique to clinical cases from the NSHA database showed a 37% decrease in the total MU compared to state-of-the-art VMAT planning of the same cases. Additionally, compared to DCA, this method was capable of more closely matching the target coverage and conformity of VMAT. It was also capable of sparing low dose to peripheral normal tissues.

Through these results, this manuscript shows the application of a hybrid method of collimation that possesses the dosimetric robustness and MU reduction abilities of DCA with the normal tissue protection and target coverage abilities of VMAT. Additionally, a novel objective function was employed to converge onto solutions of collimation patterns and MUD on a control point specific basis. This iterative convergence was made computationally feasible by calculating dose to all targets individually at all control points and performing arithmetic operations with dose voxels. Alternatively, establishing a novel system of dosimetric calculation outside of the treatment planning system would require substantial validation to be meaningful in this setting. By using the treatment planning system to evaluate all dosimetric results, the dosimetric results have been produced by a validated and commissioned clinical system.

The fourth and final manuscript returns to the concept of optimizing VMAT planning with a far greater set of degrees of freedom compared to the first manuscript. By marrying the objective functions introduced in the first and second manuscript, a hybrid

solution space is designed that is capable of synergistic optimization of multiple axes simultaneously. Extending the solution map concept to a third dimension allows the creation of a solution space where a 3D trajectory creates an axes trajectory solution on a patient specific basis. Instead of creating a dynamic solution using the dynamic algorithms, we again return to solutions which are accepted by the clinical planning system and implementable immediately clinically. Novel algorithms for the navigation of this 3D space have been created and implemented to abide by the restrictions of the planning system and compared to the state-of-the-art VMAT planning of seven multiple metastases cases using the artificial dataset introduced in the second manuscript. The result of implementing CODA was a decrease in maximum dose to OARs of 21%, with maximum brainstem dose decreased by 2.63 Gy on average. The brainstem was the OAR that received the highest dose on average with each of these cases. In addition to the OAR sparing, there was a 9% reduction in total MU, and a 4% decrease in the volume receiving 12 Gy or higher in the CODA plans.

The trajectory optimization for these cases was performed automatically without user intervention. The arc arrangement was not based on an initial template, but was generated on a patient-specific basis. Inter-planner variation was mitigated in this study by using the same experienced planner to conduct all the planning optimizations for these cases.

7.2 Future Work

The work conducted in this thesis has introduced the concepts of optimization to multiple axes of a C-arm LINAC. The solutions to these new degrees of freedom form a

single presented embodiment of what can be leveraged with implementation of these concepts in the radiotherapy planning process.

In Chapter 3, the cost equation weightings are not examined or optimized on a per patient basis. Instead, the cost equation is calculated the same way in all patients, and the trajectory is optimized on this map. A potential investigation could identify alternative weightings to the cost equation. Specifically, the relative weighting between the overlap-based cost and cost due to the USF value could be adjusted to maximize OAR sparing. Additionally, the trajectory is not optimized for gantry start-and-stop angles. This is major limitation and could increase the total cost contained in an arc, however, it was not investigated in this work due to the isolation of couch angle as the investigated variable.

The bi-direction trajectories generated in Chapter 4 are specific embodiments of navigation of the cost function space, and navigation may improve with alternative trajectories. Additionally, the restriction on collimator motion between control points, and its effect on the measured dose compared to calculated dose has not been fully investigated. It is possible that the collimator rotation mechanical restriction is too conservative and greater degrees of freedom can be leveraged by lifting this restriction. Additionally, delivery was never interrupted throughout treatment to reoptimize the position of the collimator. It is logical to hypothesize that substantial improvements in results could be made by allowing a pause in delivery to reorient the collimator in difficult collimation settings.

Chapter 5 presents perhaps the most radical modification to delivery techniques in this thesis with the development of iABC. This requires MLC transitions from control point to control point in order to completely shield a target and then to deliver dose

conformally to a target. The calculations conducted in this work are presented as discrete fields (as is the convention in treatment planning systems for dynamic plans) and the transition time between full exposure to full shielding is not modeled. Identifying the fidelity loss in dose because of this approximation ought to be the focus of further study. However, this is simply a question of engineering to deliver what we have shown here to be an increase in overall efficiency compared to standard VMAT. Additionally, the axes of the linear accelerator and MLCs must have the time required to meet the locations designed in the control points. The optimization of the sequencing of these should be additionally studied to ensure the efficiency increase in total plan MU can be converted into delivery time efficiency.

Finally, Chapter 6 presents a method of navigating the CODA cube using fixed arcs that are acceptable by the treatment planning system. This type of navigation is a simple first foray into the navigation of these types of spaces. Dynamic motions of both the collimator and the couch would present much more efficient means of exploring the solution space, provided the sampling was thorough. While dynamic motions in VMAT were not possible to include due to restrictions in planning system VMAT optimization, the literature suggests these advanced motions will leverage the benefits shown in the studies included in this thesis. Additional quality assurance methods during simultaneous motions during irradiation must be designed to ensure that regular repositioning of the couch and collimator do not result in a decrease in the fidelity of the planned dose distribution when delivered.

With faster methods of dose calculation, iterative identification of optimal trajectories can accommodate new methods for patient-specific solutions. Additionally,

with accommodation for intra-fraction motion and target localization and the appropriate adaption of these methods to extra-cranial sites, the same advantages seen here for cranial planning might be introduced to other sites.

With the complete digitization of the tools for radiotherapy so too should come the capacity to explore additional degrees of freedom in radiotherapy, and automate the present day manual tasks, such as trial-and-error in planning, allowing the capacity of physicists to be applied to furthering the impact of automation and developing increasingly advanced technologies. Additionally, tools in large-scale data organization, analysis, and extraction will change the practice of radiotherapy planning with their introduction into everyday clinical practice. The impact from allowing researchers to leverage cutting-edge developer platforms of radiotherapy tools is evident from the literature review of this thesis, as prior to 2011 there was one publication on dynamic radiotherapy, and since 2011, and the release of Developer Mode, there have been more than twenty.

7.3 CONCLUSIONS

The research in this thesis illustrates the advantages of introducing patient-specific trajectory optimization methods to modern radiosurgery practice. The advantages of these optimization methods over conventional state-of-the-art methods include decrease in OAR maximum doses with implementation of customized BEV OAR avoidance techniques, increases in overall MU efficiency and normal tissue sparing with implementation of dynamic collimator trajectories, additional capacity to accomplish demanding prescription doses in dissimilar multiple metastases cases, advancing the capacity of modern DCA, and combining these optimization methods to synergistically

deploy the techniques in a combined advanced treatment planning process that indicates superiority to conventional arc geometries in VMAT planning.

The optimization metrics built in this thesis are capable of being implemented immediately to improve current stereotactic radiosurgery treatment planning. The specific solutions to trajectory generation are implementable in modern planning systems and are readily comparable to current practice. Additionally, the fundamental elements being considered in this thesis can form the basis for radical new methods of radiosurgery arc generation to automate the complexity seen in modern radiotherapy.

REFERENCES

[1] Canadian Cancer Society, Statistics Canada, Public Health Agency of Canada, and Provincial/Territorial Cancer Registries, *Canadian cancer statistics 2017* (2017).

[2] Candian Cancer Society, Information on Treatment, Canada, Public Health Agency of Canada, and Provincial/Territorial Cancer Registries.

[3] American Society for Radiation Oncology, ASTRO Legislative Priorities. 2015.

[4] "Radiation Therapy for Cancer." Fact Sheet. National Cancer Institute. Accessed April 2, 201.

[5] C. J. Karzmark, "Medical Electron Accelerators." Medical Physics 20, no. 3 (May 1, 1993)

[6] "Intensity-Modulated Radiation Therapy (IMRT) - About - Mayo Clinic." Accessed April 3, 2018. https://www.mayoclinic.org/tests-procedures/intensity-modulated-radiation-therapy/about/pac-20385147.

[7] F.M. Kahn. The Physics of Radiation Therapy, 4th Edition. Lippincott Williams and Wilkins, 2003.

[8] Wild, Esther, Mark Bangert, Simeon Nill, and Uwe Oelfke. "Noncoplanar VMAT for Nasopharyngeal Tumors: Plan Quality versus Treatment Time." *Medical Physics* 42, no. 5 (May 2015): 2157–68. https://doi.org/10.1118/1.4914863.

[9] Yu, C. X. "Intensity-Modulated Arc Therapy with Dynamic Multileaf Collimation: An Alternative to Tomotherapy." *Physics in Medicine and Biology* 40, no. 9 (September 1995): 1435–49.

[10] Otto, Karl. "Volumetric Modulated Arc Therapy: IMRT in a Single Gantry Arc." *Medical Physics* 35, no. 1 (January 2008): 310–17. https://doi.org/10.1118/1.2818738.

[11] Cao, Daliang. "Volumetric Modulated Arc Therapy (VMAT): The future of IMRT?" *American Association of Physicists in Medicine.* Annual Meeting

[12] Infusino, Erminia. "Clinical Utility of RapidArc™ Radiotherapy Technology." *Cancer Management and Research* 7 (November 12, 2015): 345–56. https://doi.org/10.2147/CMAR.S72775.

[13] Leksell L. The stereotactic method and radiosurgery of the brain. *Acta Chir Scand.* 1952; 102:316-319.

[14] Leksell L. Stereotactic radiosurgery. J Neurological Neurosurgery Psychiatry 1983; 46:797–803.

[15] E.J. Hall and A.J. Giaccia, *Radiobiology for the Radiologist*, 7th ed. (Wolters Kluwer Health/Lippincott Williams & Wilkins, Philadelphia, PA, 2012).

[16] Kondziolka, Douglas, Samuel M. Shin, Andrew Brunswick, Irene Kim, and Joshua S. Silverman. "The Biology of Radiosurgery and Its Clinical Applications for Brain Tumors." *Neuro-Oncology* 17, no. 1 (January 2015): 29–44. https://doi.org/10.1093/neuonc/nou284.

[17] Park, Heon Joo, Robert J. Griffin, Susanta Hui, Seymour H. Levitt, and Chang W. Song. "Radiation-Induced Vascular Damage in Tumors: Implications of Vascular Damage in Ablative Hypofractionated Radiotherapy (SBRT and SRS)." *Radiation Research* 177, no. 3 (March 2012): 311–27.

[18] Andrews, David W., Charles B. Scott, Paul W. Sperduto, Adam E. Flanders, Laurie E. Gaspar, Michael C. Schell, Maria Werner-Wasik, *et al*. "Whole Brain Radiation Therapy with or without Stereotactic Radiosurgery Boost for Patients with One to Three Brain Metastases: Phase III Results of the RTOG 9508 Randomised Trial." *Lancet (London, England)* 363, no. 9422 (May 22, 2004): 1665–72. https://doi.org/10.1016/S0140-6736(04)16250-8.

[19] Paldor, Iddo, Annie S. Chen, and Andrew H. Kaye. "Growth Rate of Vestibular Schwannoma." *Journal of Clinical Neuroscience: Official Journal of the Neurosurgical Society of Australasia* 32 (October 2016): 1–8. https://doi.org/10.1016/j.jocn.2016.05.003.

[20] Watanabe, Shinya, Masaaki Yamamoto, Takuya Kawabe, Takao Koiso, Tetsuya Yamamoto, Akira Matsumura, and Hidetoshi Kasuya. "Stereotactic Radiosurgery for Vestibular Schwannomas: Average 10-Year Follow-up Results Focusing on Long-Term Hearing Preservation." *Special Supplements* 125, no. Supplement 1 (December 1, 2016): 64–72. https://doi.org/10.3171/2016.7.GKS161494.

[21] Johns HE, Bates LM, Watson TA. 1,000 curie cobalt units for radiation therapy: the Saskatchewan cobalt 60 unit. *Br. J. Radiol.* 1952;25:296.

[22] Betti O, Derechinsky V. Hyper selective encephalic irradiation with a linear accelerator. Acta Neurochir 1984; Suppl 33:385–390.

[23] Columbo F, Benedetti A, Pozza F, *et al*. External stereotactic irradiation by linear accelerator. Neurosurgery 1985; 16:154–160.

[24] Podgorsak E, Pike G, Olivier A, *et al*. Radiosurgery with high energy photon beams: a comparison among techniques. Int J Radiat Oncol Biol Phys 1989; 16:857–865.

[25] Hadley, M. N., A. G. Shetter, and M. R. Amos. “Use of the Brown-Roberts-Wells Stereotactic Frame for Functional Neurosurgery.” *Applied Neurophysiology* 48, no. 1–6 (1985): 61–68.

[26] Winston, K. R., and W. Lutz. “Linear Accelerator as a Neurosurgical Tool for Stereotactic Radiosurgery.” *Neurosurgery* 22, no. 3 (March 1988): 454–64.

[27] Gill, S. S., D. G. Thomas, A. P. Warrington, and M. Brada. “Relocatable Frame for Stereotactic External Beam Radiotherapy.” *International Journal of Radiation Oncology, Biology, Physics* 20, no. 3 (March 1991): 599–603.

[28] J. Robar, Linear accelerator-based stereotactic radiosurgery and stereotactic radiation therapy, Curriculum for CAMRT Dosimetry III Course.

[29] Babic, Steven, Young Lee, Mark Ruschin, Fiona Lochray, Alex Lightstone, Eshetu Atenafu, Nic Phan, *et al*. “To Frame or Not to Frame? Cone-Beam CT-Based Analysis of Head Immobilization Devices Specific to Linac-Based Stereotactic Radiosurgery and Radiotherapy.” *Journal of Applied Clinical Medical Physics* 19, no. 2 (March 2018): 111–20. https://doi.org/10.1002/acm2.12251.

[30] Orton, Colin G., Thomas R. Bortfeld, Andrzej Niemierko, and Jan Unkelbach. “The Role of Medical Physicists and the AAPM in the Development of Treatment Planning and Optimization.” *Medical Physics* 35, no. 11 (November 2008): 4911–23. https://doi.org/10.1118/1.2990777.

[31] K.C. Tsien “The application of automatic computing machines for radiotherapy treatment planning,” Br. J. Radiol. 28, 432-439 (1955).

[32] S. Webb, “Optimization of conformal radiotherapy dose distributions by simulated annealing,” Phys. Med. Biol. **34**, 1349–1370 1989.

[33] Y. Censor, M. D. Altschuler, and W. D. Powlis, “A computational solution of the inverse problem in radiation-therapy treatment planning,”

[34] D. J. Convery and M. E. Rosenbloom, “The generation of intensity modulated fields for conformal radiotherapy by dynamic collimation,” Phys. Med. Biol. 37, 1359–1374 1992.

[35] T. Bortfeld, D. L. Kahler, T. J. Waldron, and A. L. Boyer, “X-ray field compensation with multi-leaf collimators,” Int. J. Radiat. Oncol., Biol., Phys. 28, 723–730 1994.

[36] S. V. Spirou and C. S. Chui, “Generation of arbitrary fluence profiles by dynamic jaws or multi-leaf collimators,” Med. Phys. 21, 1031–1041 1994.

[37] D. M. Shepard, M. A. Earl, X. A. Li, S. Naqvi, and C. Yu, "Direct aperture optimization: A turnkey solution for step-and-shoot IMRT," Med. Phys. 29, 1007–1018 2002.

[38] Xiaochun Wang, Xiaodong Zhang, Lei Dong, Helen Liu, Qiuwen Wu, and Radhe Mohan. "Development of Methods for Beam Angle Optimization for IMRT Using an Accelerated Exhaustive Search Strategy." International Journal of Radiation Oncology • Biology • Physics 60, no. 4 (November 15, 2004): 1325–37. https://doi.org/10.1016/j.ijrobp.2004.06.007.

[39] Rowbottom CG, Nutting CM, Webb S. Beam-orientation optimization of intensity-modulated radiotherapy: Clinical application to parotid gland tumors. *Radiother Oncol* 2001;59:169–177.

[40] Pugachev, A., and L. Xing. "Pseudo Beam's-Eye-View as Applied to Beam Orientation Selection in Intensity-Modulated Radiation Therapy." *International Journal of Radiation Oncology, Biology, Physics* 51, no. 5 (December 1, 2001): 1361–70.

[41] Pugachev, Andrei, and Lei Xing. "Incorporating Prior Knowledge into Beam Orientaton Optimization in IMRT." *International Journal of Radiation Oncology • Biology • Physics* 54, no. 5 (December 1, 2002): 1565–74. https://doi.org/10.1016/S0360-3016(02)03917-2.

[42] Stein Jörg, Mohan Radhe, Wang Xiao-Hong, Bortfeld Thomas, Wu Qiuwen, Preiser Konrad, Ling C. Clifton, and Schlegel Wolfgang. "Number and Orientations of Beams in Intensity-modulated Radiation Treatments." *Medical Physics* 24, no. 2 (June 4, 1998): 149–60. https://doi.org/10.1118/1.597923.

[43] Brahme, Anders. "Optimization of Stationary and Moving Beam Radiation Therapy Techniques." *Radiotherapy and Oncology* 12, no. 2 (June 1, 1988): 129–40. https://doi.org/10.1016/0167-8140(88)90167-3.

[44] Bortfeld, T., and W. Schlegel. "Optimization of Beam Orientations in Radiation Therapy: Some Theoretical Considerations." *Physics in Medicine & Biology* 38, no. 2 (1993): 291. https://doi.org/10.1088/0031-9155/38/2/006.

[45] Grant M. Clark, Richard A. Popple, Brendan M. Prendergast, Sharon A. Spencer, Evan M. Thomas, John G. Stewart, Barton L. Guthrie, James M. Markert, and John B. Fiveash. "Plan Quality and Treatment Planning Technique for Single Isocenter Cranial Radiosurgery with Volumetric Modulated Arc Therapy." Practical Radiation Oncology 2, no. 4 (October–December 2012): 306-313. doi:10.1016/j.prro.2011.12.003.

[46] Podgorsak EB, Olivier A, Pla M, *et al*. Dynamic stereotactic radiosurgery. Int J Radiat Oncol Biol Phys 1988;14:115-126.

[47] Yang, Y., Zhang, P., Happersett, L., Xiong, J., Yang, J., Chan, *et al*. (2011). Choreographing couch and collimator in volumetric modulated arc therapy. International Journal of Radiation Oncology Biology, Physics.

[48] Shaitelman, S.F., Kim. L.H., Yan, D., Martinez, A.A., Vicini, F.A., & Grills, I.S. (2011). Continuous arc rotation of the couch therapy for the delivery of accelerated partial breast irradiation: a treatment planning analysis. International Journal of Radiation Oncology, Biology, Physics.

[49] Dong, P., Lee, P., Ruan, D., Long, T., Romeijn, E., Yang, Y., *et al*. (2013). 4π Non-coplanar liver SBRT: a novel delivery technique. International Journal of Radiation Oncology, Biology, Physics, 85(5), 1360-66.

[50] Dong, P., Lee, P., Ruan, D., Long, T., Romeijn, E., Yang, Y., *et al*. (2013). 4π Noncoplanar stereotactic body radiation therapy for centrally located or larger lung tumors. International Journal of Radiation Oncology, Biology, Physics, 86(3), 407-13.

[51] Fahimian, B., Yu, V., Horst, K., Xing, L., & Hristov, D. (2013). Trajectory modulated prone breast irradiation: a LINAC-based technique combining intensity modulated delivery and motion of the couch. Radiotherapy and Oncology: Journal of the European Society for Therapeutic Radiology and Oncology, 109(3), 475-81.

[52] Popescu, C.C., Beckham, W.A., Patenaude, V.V., Olivotto, I.A., & Vlachaki, M.T. (2013). Simultaneous couch and gantry dynamic arc rotation (CG-Darc) in the treatment of breast cancer with accelerated partial breast irradiation (APBI): Feasibility Study. Journal of Applied Clinical Medical Physics / American College of Medical Physics, 14(1), 161-175.

[53] Rodrigues, Anna, Fang-Fang Yin, and Qiuwen Wu. "Dynamic Electron Arc Radiotherapy (DEAR): A Feasibility Study." *Physics in Medicine and Biology* 59, no. 2 (January 20, 2014): 327–45. https://doi.org/10.1088/0031-9155/59/2/327.

[54] Smyth, G., Bamber, J.C., Evans, P.M., & Bedford, J.L. (2013). Trajectory optimization for dynamic couch rotation during volumetric modulated arc radiotherapy. Physics in Medicine and Biology, 58(22), 8163-77.

[55] Yu Victoria Y., Fahimian Benjamin P., Xing Lei, and Hristov Dimitre H. "Quality Control Procedures for Dynamic Treatment Delivery Techniques Involving Couch Motion." *Medical Physics* 41, no. 8Part1 (July 23, 2014): 081712. https://doi.org/10.1118/1.4886757.

[56] Liang, Jieming, Todd Atwood, Rie von Eyben, Benjamin Fahimian, Erika Chin, Kathleen Horst, Karl Otto, and Dimitre Hristov. "Trajectory Modulated Arc Therapy: A Fully Dynamic Delivery With Synchronized Couch and Gantry Motion Significantly Improves Dosimetric Indices Correlated With Poor Cosmesis

in Accelerated Partial Breast Irradiation." *International Journal of Radiation Oncology, Biology, Physics* 92, no. 5 (August 1, 2015): 1148–56. https://doi.org/10.1016/j.ijrobp.2015.04.034.

[57] Papp, D., Bortfeld, T., & Unkelbach, J. (2105). A modular approach to intensity modulated arc therapy optimization with noncoplanar trajectories. Physics in Medicine and Biology, 60(13), 5179?98.

[58] Wild, Esther, Mark Bangert, Simeon Nill, and Uwe Oelfke. "Noncoplanar VMAT for Nasopharyngeal Tumors: Plan Quality versus Treatment Time." *Medical Physics* 42, no. 5 (May 2015): 2157–68. https://doi.org/10.1118/1.4914863.

[59] Burghelea, M., Verellen D., Poels, K., Hung, C., Nakamura, M., Dhont, J., *et al*. (2016). Initial characterization, dosimetric benchmark and performance validation of Dynamic Wave Arc. Radiation Oncology, 11(63), 1-10.

[60] MacDonald, R. Lee, and Christopher G. Thomas. "Dynamic Trajectory-Based Couch Motion for Improvement of Radiation Therapy Trajectories in Cranial SRT." *Medical Physics* 42, no. 5 (May 2015): 2317–25. https://doi.org/10.1118/1.4917165.

[61] Smyth, Gregory, Philip M. Evans, Jeffrey C. Bamber, Henry C. Mandeville, Liam C. Welsh, Frank H. Saran, and James L. Bedford. "Non-Coplanar Trajectories to Improve Organ at Risk Sparing in Volumetric Modulated Arc Therapy for Primary Brain Tumors." *Radiotherapy and Oncology: Journal of the European Society for Therapeutic Radiology and Oncology* 121, no. 1 (2016): 124–31. https://doi.org/10.1016/j.radonc.2016.07.014.

[62] Wilson, Byron, Karl Otto, and Ermias Gete. "A Simple and Robust Trajectory-Based Stereotactic Radiosurgery Treatment." *Medical Physics* 44, no. 1 (January 2017): 240–48. https://doi.org/10.1002/mp.12036.

[63] Wilson, Byron, and Ermias Gete. "Machine-Specific Quality Assurance Procedure for Stereotactic Treatments with Dynamic Couch Rotations." *Medical Physics* 44, no. 12 (December 2017): 6529–37. https://doi.org/10.1002/mp.12589.

[64] Yu, Victoria Y., Angelia Landers, Kaley Woods, Dan Nguyen, Minsong Cao, Dongsu Du, Robert K. Chin, Ke Sheng, and Tania B. Kaprealian. "A Prospective 4π Radiation Therapy Clinical Study in Recurrent High-Grade Glioma Patients." *International Journal of Radiation Oncology, Biology, Physics* 101, no. 1 (May 1, 2018): 144–51. https://doi.org/10.1016/j.ijrobp.2018.01.048.

[65] Langhans, Marco, Jan Unkelbach, Thomas Bortfeld, and David Craft. "Optimizing Highly Noncoplanar VMAT Trajectories: The NoVo Method." *Physics in Medicine & Biology* 63, no. 2 (2018): 025023. https://doi.org/10.1088/1361-6560/aaa36d.

[66] Siochi RA, inventor; Siemens Medical Solutions USA, Inc., assignee. High definition radiation treatment with an intensity modulating multi-leaf collimator. United States patent US 6,757,355;2004.

[67] Otto K, inventor; BC Cancer Agency, assignee. Methods and apparatus for planning and delivering intensity modulated radiation fields with a rotating multi-leaf collimator. United States patent US 6,907,105; 2005.

[68] Otto K, Milette MP, inventors; BC Cancer Agency, assignee. Method and apparatus for planning and delivering radiation treatment. United States patent US 7,734,010; 2010.

[69] Milette, Marie-Pierre, and Karl Otto. "Maximizing the Potential of Direct Aperture Optimization through Collimator Rotation." *Medical Physics* 34, no. 4 (April 2007): 1431–38. https://doi.org/10.1118/1.2712574.

[70] Webb, S. "Does the Option to Rotate the Elekta Beam Modulator MLC during VMAT IMRT Delivery Confer Advantage?--a Study of 'Parked Gaps.'" *Physics in Medicine and Biology* 55, no. 11 (June 7, 2010): N303-319. https://doi.org/10.1088/0031-9155/55/11/N01.

[71] Zhang, Pengpeng, Laura Happersett, Yingli Yang, Yoshiya Yamada, Gig Mageras, and Margie Hunt. "Optimization of Collimator Trajectory in Volumetric Modulated Arc Therapy: Development and Evaluation for Paraspinal SBRT." *International Journal of Radiation Oncology, Biology, Physics* 77, no. 2 (June 1, 2010): 591–99. https://doi.org/10.1016/j.ijrobp.2009.08.056.

[72] Locke, Christopher Barry, and Karl Kenneth Bush. "Trajectory Optimization in Radiotherapy Using Sectioning (TORUS)." *Medical Physics* 44, no. 7 (July 2017): 3375–92. https://doi.org/10.1002/mp.12270.

[73] Lee, Christopher M., Gordon A. Watson, and Dennis D. Leavitt. "Dynamic Collimator Optimization Compared with Fixed Collimator Angle in Arc-Based Stereotactic Radiotherapy: A Dosimetric Analysis." *Neurosurgical Focus* 19, no. 1 (July 15, 2005): E12.

[74] F.H. Attix. *Introduction to Radiological Physics and Radiation Dosimetry.* Wiley-VCH, 2004.

[75] E.B. Podgorsak, *Radiation Oncology Physics: A Handbook for Teachers and Students*. (IAEA, 2005).

[76] Varian Medical Systems Inc., Eclipse Algorithms Reference Guide, December 2011.

[77] Varian Medical Systems – TrueBeam™ Developer Mode User's Manual – April 2011

[78] G. Gordon Steel, T.J. McMillan & J.H. Peacock (1989) The 5Rs of Radiobiology, International Journal of Radiation Biology, 56:6, 1045-1048, DOI: 10.1080/09553008914552491

[79] Brown, J. Martin, David J. Carlson, and David J. Brenner. "The Tumor Radiobiology of SRS and SBRT: Are More than the 5 R's Involved?" International Journal of Radiation Oncology, Biology, Physics 88, no. 2 (February 1, 2014): 254–62. https://doi.org/10.1016/j.ijrobp.2013.07.022.

[80] Song, Chang W., L. Chinsoo Cho, Jianling Yuan, Kathryn E. Dusenbery, Robert J. Griffin, and Seymour H. Levitt. "Radiobiology of Stereotactic Body Radiation Therapy/Stereotactic Radiosurgery and the Linear-Quadratic Model." International Journal of Radiation Oncology, Biology, Physics 87, no. 1 (September 1, 2013): 18–19. https://doi.org/10.1016/j.ijrobp.2013.03.013.

[81] Ma, Lijun, Paula Petti, Brian Wang, Martina Descovich, Cynthia Chuang, Igor J. Barani, Sandeep Kunwar, Dennis C. Shrieve, Arjun Sahgal, and David A. Larson. "Apparatus Dependence of Normal Brain Tissue Dose in Stereotactic Radiosurgery for Multiple Brain Metastases." Journal of Neurosurgery 114, no. 6 (June 2011): 1580–84. https://doi.org/10.3171/2011.1.JNS101056.

[82] Ma, Lijun, Alan Nichol, Sabbir Hossain, Brian Wang, Paula Petti, Rosemin Vellani, Chris Higby, *et al*. "Variable Dose Interplay Effects across Radiosurgical Apparatus in Treating Multiple Brain Metastases." International Journal of Computer Assisted Radiology and Surgery 9, no. 6 (2014): 1079–86. https://doi.org/10.1007/s11548-014-1001-4.

[83] Marks, Lawrence B., Ellen D. Yorke, Andrew Jackson, Randall K. Ten Haken, Louis S. Constine, Avraham Eisbruch, Søren M. Bentzen, Jiho Nam, and Joseph O. Deasy. "Use of Normal Tissue Complication Probability Models in the Clinic." International Journal of Radiation Oncology Biology Physics 76, no. 3 (March 1, 2010): S10 – S19. doi:10.1016/j.ijrobp.2009.07.1754

[84] Oliver, Mike, Jeff Chen, Eugene Wong, Jake Van Dyk, and Francisco Perera. "A Treatment Planning Study Comparing Whole Breast Radiation Therapy against Conformal, IMRT and Tomotherapy for Accelerated Partial Breast Irradiation." Radiotherapy and Oncology: Journal of the European Society for Therapeutic Radiology and Oncology 82, no. 3 (March 2007): 317–23. doi:10.1016/j.radonc.2006.11.021.

[85] Van't Riet, Arie, C.A. Mak, Marinus A. Moerland, Leo H. Elders, Wiebe Van Der Zee. "A conformation number to quantify the degree of conformality in brachytherapy and external beam irradiation: Application to the prostate." International Journal of Radiation Oncology Biology Physics 37, no. 3 (February 1, 1997): 731–6. doi:10.1016/S0360-3016(96)00601-3.

[86] Shiraishi, Satomi, Jun Tan, Lindsey A. Olsen, and Kevin L. Moore. “Knowledge-Based Prediction of Plan Quality Metrics in Intracranial Stereotactic Radiosurgery.” Medical Physics 42, no. 2 (February 2015): 908. doi:10.1118/1.4906183.

[87] International Electrotechnical Commission. IEC1217: Radiotherapy equipment-Coordinates, movements and scales, 1996.

[88] Sham, Edwin. "Evaluation of A Mono-Isocentric Treatment Planning Software For Stereotactic Radiosurgery Of Multiple Brain Metastases". 2016. Poster.

[89] Mutic S, Low D A, Klein E E, Dempsey J F and Purdy J A 2001 Room shielding for intensity modulated radiation therapy treatment facilities Int J Radiat Oncol 50 239J46

[90] Mohan, R., M. Arnfield, S. Tong, Q. Wu, and J. Siebers. “The Impact of Fluctuations in Intensity Patterns on the Number of Monitor Units and the Quality and Accuracy of Intensity Modulated Radiotherapy.” Medical Physics 27, no. 6 (June 2000): 1226–37. doi:10.1118/1.599000.

[91] Lee, Mark T., Thomas G. Purdie, Cynthia L. Eccles, Michael B. Sharpe, and Laura A. Dawson. “Comparison of Simple and Complex Liver Intensity Modulated Radiotherapy.” Radiation Oncology 5 (2010): 115. doi:10.1186/1748-717X-5-115.

[92] Kry, Stephen F., Mohammad Salehpour, David S. Followill, Marilyn Stovall, Deborah A. Kuban, R. Allen White, and Isaac I. Rosen. “The Calculated Risk of Fatal Secondary Malignancies from Intensity-Modulated Radiation Therapy.” International Journal of Radiation Oncology, Biology, Physics 62, no. 4 (July 15, 2005): 1195–1203. doi:10.1016/j.ijrobp.2005.03.053.

[93] Verellen, D., and F. Vanhavere. “Risk Assessment of Radiation-Induced Malignancies Based on Whole-Body Equivalent Dose Estimates for IMRT Treatment in the Head and Neck Region.” Radiotherapy and Oncology: Journal of the European Society for Therapeutic Radiology and Oncology 53, no. 3 (December 1999): 199–203.

[94] Timlin, C., D. R. Warren, B. Rowland, A. Madkhali, J. Loken, M. Partridge, B. Jones, J. Kruse, and R. Miller. “3D Calculation of Radiation-Induced Second Cancer Risk Including Dose and Tissue Response Heterogeneities.” Medical Physics 42, no. 2 (February 1, 2015): 866–76. doi:10.1118/1.4905158.

[95] Grimm, Jimm, Tamara LaCouture, Raymond Croce, Inhwan Yeo, Yunping Zhu, and Jinyu Xue. “Dose Tolerance Limits and Dose Volume Histogram Evaluation for Stereotactic Body Radiotherapy.” Journal of Applied Clinical Medical Physics 12, no. 2 (February 8, 2011). http://www.jacmp.org/index.php/jacmp/article/view/3368.

[96] Blonigen, Brian J., Ryan D. Steinmetz, Linda Levin, Michael A. Lamba, Ronald E. Warnick, and John C. Breneman. “Irradiated Volume as a Predictor of Brain Radionecrosis after Linear Accelerator Stereotactic Radiosurgery.” International Journal of Radiation Oncology, Biology, 625 Physics 77, no. 4 (July 15, 2010): 996–1001. doi:10.1016/j.ijrobp.2009.06.006.

[97] Webb, S. “Optimizing the Planning of Intensity-Modulated Radiotherapy.” Physics in Medicine & Biology 39, no. 12 (1994): 2229. https://doi.org/10.1088/0031-9155/39/12/007.

[98] Narayanasamy, Ganesh, Sotirios Stathakis, Alonso N. Gutierrez, Evangelos Pappas, Richard Crownover, John R. Floyd, and Niko 400 Papanikolaou. “A Systematic Analysis of 2 Monoisocentric Techniques for the Treatment of Multiple Brain Metastases.” Technology in Cancer Research & Treatment 16, no. 5 (October 2017): 639–44. https://doi.org/10.1177/1533034616666998.

[99] Wang *et al*., “Are Simple IMRT Beams More Robust against MLC Error?” JACPM 17, no.3 (147-57)

[100] Dias, Joana *et al*. Simulated annealing applied to IMRT beam angle optimization: A computational study Physica Medica: European Journal of Medical Physics , Volume 30 , e21.

[101] Piotrowski, Tomasz, Małgorzata Skórska, Agata Jodda, Adam Ryczkowski, Joanna Kaźmierska, Krystyna Adamska, Aldona Karczewska-435 Dzionk, Małgorzata Żmijewska-Tomczak, and Hanna Włodarczyk. “Tomotherapy – a Different Way of Dose Delivery in Radiotherapy.” Contemporary Oncology 16, no. 1 (2012): 16–25. https://doi.org/10.5114/wo.2012.27332.

[102] Panet-Raymond, Valerie, Will Ansbacher, Sergei Zavgorodni, Bill Bendorffe, Alan Nichol, Pauline T. Truong, Wayne Beckham, and Maria Vlachaki. “Coplanar versus Noncoplanar Intensity-Modulated Radiation Therapy (IMRT) and Volumetric-Modulated Arc Therapy (VMAT) Treatment Planning for Fronto-Temporal High-Grade Glioma.” Journal of Applied Clinical Medical Physics 13, no. 4 (July 5, 2012): 3826.

[103] “Elements Cranial SRS.” Brainlab. Accessed March 19, 2018. https://www.brainlab.com/en/radiosurgery-products/brain/cranial-srs/.

[104] “Varian Hyper-Arc: High Definition Radiotherapy–Varian Medical Systems”. Accessed March 19, 2018. https://www.varian.com/oncology/solutions/hyperarc

[105] Chin, Lawrence S., Regine, William F. “Principles and Practice of Stereotactic Radiosurgery” 2008. 978-0-387-71069-3

[106] Whelan *et al.*, Characterisation of a gridded electron gun in magnetic fields: implications for MRI-Linac therapy. University of Sydney, Australia. ESTRO 2016.

[107] Varian Medical Systems, TrueBeam STx System Specifications. August 2015.

[108] Shepard, David, Gamma Knife and CyberKnife: Physics and Quality Assurance. Swedish Cancer Institute, Seattle WA. AAPM Presentation.

[109] Dijkstra, E. W. "A Note on Two Problems in Connexion with Graphs." Numer. Math. 1, no. 1 (December 1959): 269–271. https://doi.org/10.1007/BF01386390.

[110] Varian Medical Systems, The Evolution of Intensity Modulated Radiation Therapy (IMRT), 1999 Annual Report. http://media.corporate-ir.net/media_files/nys/var/annual/10.htm

[111] "Clinical." Medical Physics Unit. McGill University. Accessed June 15, 2018. https://www.mcgill.ca/medphys/clinical.

[112] Laub, W. "SU-E-T-680: Comparison between XVMC Monte Carlo and Eclipse AAA Dose Calculations for Rapidarc Plans." Medical Physics 38, no. 6Part21 (n.d.): 3646–3646. https://doi.org/10.1118/1.3612642.

[113] Brainlab AG, Monte Carlo Dose Algorithm, Clinical White Paper, August 2011.

[114] Kirkpatrick, S., C. D. Gelatt, and M. P. Vecchi. "Optimization by Simulated Annealing." *Science* 220, no. 4598 (1983): 671–80.

[115] Stelzer, Keith J. "Epidemiology and Prognosis of Brain Metastases." Surgical Neurology International 4, no. Suppl 4 (May 2, 2013): S192–202. https://doi.org/10.4103/2152-7806.111296.

[116] NRCC Report PIRS-701: The EGSnrc Code System: Monte Carlo Simulation of Electron and Photon Transport, I. Kawrakow and D.W.O. Rogers; Nov 7, 2003.

APPENDIX A Copyright Permission

A.1 Permission For: Overlap-guided fixed-patient support positioning optimization for cranial SRT

JOHN WILEY AND SONS LICENSE
TERMS AND CONDITIONS
Apr 16, 2018

This Agreement between Dalhousie University -- Robert MacDonald ("You") and John Wiley and Sons ("John Wiley and Sons") consists of your license details and the terms and conditions provided by John Wiley and Sons and Copyright Clearance Center.

License Number	4330810005728
License date	Apr 16, 2018
Licensed Content Publisher	John Wiley and Sons
Licensed Content Publication	Medical Physics
Licensed Content Title	Overlap-guided fixed-patient support positioning optimization for cranial SRT
Licensed Content Author	R. Lee MacDonald, James L. Robar, Christopher G. Thomas
Licensed Content Date	Jan 3, 2017
Licensed Content Volume	44
Licensed Content Issue	1
Licensed Content Pages	11
Type of Use	Dissertation/Thesis
Requestor type	Author of this Wiley article
Format	Print and electronic
Portion	Full article

Will you be translating?	No
Title of your thesis / dissertation	Trajectory Radiation Therapy
Expected completion date	Aug 2018
Expected size (number of pages)	200
Requestor Location	Dalhousie University Department of Medical Physics 5820 University Avenue Halifax, NS B3H 1V7 Canada
Publisher Tax ID	EU826007151
Total	0.00 CAD

A.2 PERMISSION FOR: DYNAMIC COLLIMATOR TRAJECTORY ALGORITHM FOR MULTIPLE METASTASES DYNAMIC CONFORMAL ARC TREATMENT PLANNING

JOHN WILEY AND SONS LICENSE
TERMS AND CONDITIONS

Apr 16, 2018

This Agreement between Dalhousie University -- Robert MacDonald ("You") and John Wiley and Sons ("John Wiley and Sons") consists of your license details and the terms and conditions provided by John Wiley and Sons and Copyright Clearance Center.

License Number	4330820514272
License date	Apr 16, 2018
Licensed Content Publisher	John Wiley and Sons
Licensed Content Publication	Medical Physics
Licensed Content Title	Dynamic collimator trajectory algorithm for multiple metastases dynamic conformal arc treatment planning
Licensed Content Author	R. Lee MacDonald, Christopher G. Thomas, Alasdair Syme
Licensed Content Date	Nov 27, 2017
Licensed Content Volume	45
Licensed Content Issue	1
Licensed Content Pages	13
Type of use	Dissertation/Thesis
Requestor type	Author of this Wiley article
Format	Print and electronic
Portion	Full article
Will you be translating?	No
Title of your thesis / dissertation	Trajectory Radiation Therapy

Expected completion date	Aug 2018
Expected size (number of pages)	200
Requestor Location	Dalhousie University Department of Medical Physics 5820 University Avenue Halifax, NS B3H 1V7 Canada
Publisher Tax ID	EU826007151
Total	0.00 CAD